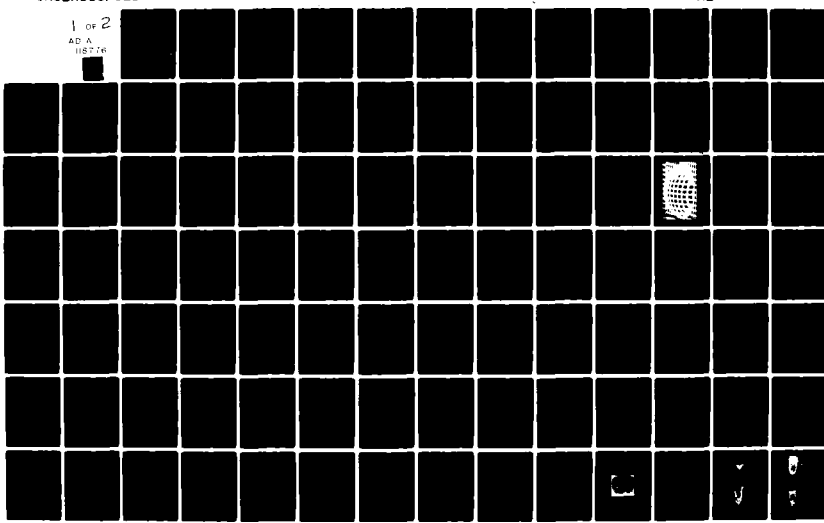


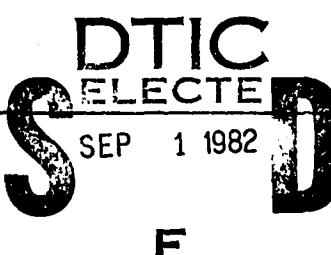
AD-A118 776

MASSACHUSETTS INST OF TECH CAMBRIDGE DEPT OF MATERIALS--ETC F/G 13/8
HEAT SOURCE - MATERIALS INTERACTIONS DURING FUSION WELDING. (U)
APR 82 T W EAGAR, A BLOCK-BOLTON, C ALLEMAND N00014-80-C-0384
NL

UNCLASSIFIED

1 OF 2
AD A
118776



REPORT DOCUMENTATION PAGE		READ INSTRUCTIONS BEFORE COMPLETING
1. REPORT NUMBER	2. GOVT ACCESSION NO.	3. RECIPIENT'S CATALOG NUMBER
		AD-A118776
4. TITLE (and Subtitle) Heat Source - Materials Interactions During Fusion Welding		5. TYPE OF REPORT & PERIOD COVERED 2nd Annual Technical Report April 30, 1982
7. AUTHOR(s) T. W. Eagar, A. Block-Bolten, C. Allemand, D. Hardt, J. Katz, C. Huntington, G. Hunter, G. Dunn, S.K. Fan, A. Lynch, D. Ries, R. Schoder, B. Wilson, M. Lin		6. PERFORMING ORGS. REPORT NUMBER N00014-80-C-0384
9. PERFORMING ORGANIZATION NAME AND ADDRESS Department of Materials Science & Engineering Massachusetts Institute of Technology Cambridge, MA 02139		10. PROGRAM ELEMENT, PROJECT, TASK AREA & WORK UNIT NUMBERS
11. CONTROLLING OFFICE NAME AND ADDRESS Dr. Bruce A. MacDonald Office of Naval Research 800 N. Quincy, Arlington, VA 22217		12. REPORT DATE April 30, 1982
14. MONITORING AGENCY NAME & ADDRESS (if different from Controlling Office)		13. NUMBER OF PAGES 15. SECURITY CLASS. (of this report) Unclassified
16. DISTRIBUTION STATEMENT (of this Report) Reproduction in whole or in part is permitted for any purposes of the United States Government. Distribution of this document is unlimited.		15a. DECLASSIFICATION/DECONVERSION SCHEDULE
17. DISTRIBUTION STATEMENT (of the abstract entered in Block 20, if different from Report)		
18. SUPPLEMENTARY NOTES		 S SEP 1 1982 D F
19. KEY WORDS (Continue on reverse side if necessary and identify by block number) welding, arc, laser, spectrographic measurements, titanium, HY-80, sensors		
20. ABSTRACT (Continue on reverse side if necessary and identify by block number) This report summarizes the second year of research involving spectrographic and thermodynamic studies of vapor emission from welding arcs, infrared measurement of the weld pool surface temperature, electroslag welding of titanium, fracture toughness of HY-80, sensors for weld automation and laser welding of aluminum. All results are preliminary except for preprints of five technical papers which have been submitted for publication.		

AD A118776

DTIC FILE COPY

HEAT SOURCE - MATERIALS INTERACTIONS DURING FUSION WELDING

by

T. W. Eagar, A. Block-Bolten, C. Allemand,
D. Hardt, J. Katz, C. Huntington, G. Hunter, G. Dunn,
S. K. Fan, A. Lynch, D. Ries, R. Schoder, B. Wilson, M. Lin

Second Annual Technical Report

Contract N00014-80-C-0384

to

Office of Naval Research

Department of the Navy

Arlington, VA 22217

Attention: Dr. Bruce B. MacDonald

April 30, 1982

Reproduction in whole or in part is permitted for any purposes of the
United States Government. Distribution of this document is unlimited.

HEAT SOURCE - MATERIALS INTERACTIONS DURING FUSION WELDING

April 30, 1982

Table of Contents

	<u>Page</u>
ABSTRACT	4
INTRODUCTION	5
1. SPECTROGRAPHIC STUDIES OF THE ARC AND WELD POOL	6
A. Infrared Spectrometer System Dr. C. Allemand and G. Hunter	6
B. Measurement of Metal Vapors in the Arc Plasma Dr. A. Block-Bolten and G. Dunn	13
2. JOINING OF HEAVY SECTION TITANIUM	17
A. Electroslag Welding of Titanium S. K. Fan, A. Lynch, Prof. T. DebRoy and Dr. A. Block-Bolten	17
B. Gas Metal Arc Welding of Titanium D. Ries and R. Schoder	22
3. FRACTURE TOUGHNESS OF HY-80 WELD METAL	27
A. Submerged Arc Welding B. Wilson	27
B. Effect of Nitrogen Contamination on Strain Ageing in HY-80 Weld Metal O. Boydas	27
4. SENSORS FOR AUTOMATED WELDING	31
A. Imaging of Weld Pool Surface Depression by Structured Laser Light M. Lin and Dr. C. Allemand	31
B. Signal Analysis of Voltage Noise in Welding Arcs	37
C. Ultrasonic Measurement of Weld Pool Shape Prof. D. Hardt and J. Katz	38
5. ADDITIONAL RESEARCH TOPICS	45
REFERENCES	46
APPENDIX A - Selective Evaporation of Metals from Weld Pools A. Block-Bolten and T. W. Eagar	47

	<u>Page</u>
APPENDIX B - A Fast Response Transistor Current Regulator for Welding Research D. Galler and A. Kusko	66
APPENDIX C - Signal Analysis of Voltage Noise in Welding Arcs E. Elias and T. W. Eagar	74
APPENDIX D - Laser Welding of Aluminum and Aluminum Alloys C. A. Huntington and T. W. Eagar	82
APPENDIX E - On the Relationship Between the Phase Diagram and the Temperature Dependence of the Equilibrium Oxygen Pressure in Metal Oxide Systems A. Block-Bolten and D. R. Sadoway	100

Accession For	
NTIS GRA&I	
DTIC TAB	
Unannounced	
Justification	
By _____	
Distribution/ _____	
Availability Codes _____	
Dist	Avail and/or Special
A	



ABSTRACT

This report summarizes the second year of research involving spectrographic and thermodynamic studies of vapor emission from welding arcs, infrared measurement of the weld pool surface temperature, electroslag welding of titanium, fracture toughness of HY-80, sensors for weld automation and laser welding of aluminum. All results are preliminary except for preprints of five technical papers which have been submitted for publication.

INTRODUCTION

This report describes work performed in the MIT Welding Laboratory under Office of Naval Research sponsorship. The work is generally fundamental in nature but attempts have been made to interface the studies with several specific U.S. Navy programs. The best examples of these directed programs include evaluation of special joining technologies for heavy section titanium and evaluation of the fracture toughness of HY-80 weld metal. Direct contact with DTNSRDC-Annapolis, General Dynamics/Electric Boat Division and Alcoa Technical Center has been helpful for several of the studies. Each of these three laboratories has contributed in some manner to the progress reported here through either consultation, materials and/or services.

The research conducted from 15 February 1981 to 14 February 1982 can broadly be divided into four main topics, viz.

1. Spectrographic studies of the arc and weld pool
2. Joining of heavy section titanium
3. Fracture toughness of HY-80 weld metal
4. Sensors for automation of arc welding.

The work performed in each of these areas will be discussed. Whenever possible, papers submitted for publication will be used in place of a separate progress report.

1. SPECTROGRAPHIC STUDIES OF THE ARC AND WELD POOL

Spectrographic studies are being conducted to measure the surface temperature of the weld pool and to determine the dominant metal vapors present in the arc plasma. The two studies are coupled through a thermodynamic upper bound analysis of the surface temperature at the pool which also predicts the metal vapor concentration as a function of alloy composition. A technical paper discussing this model is presented in Appendix A. Descriptions of the surface temperature measurement apparatus and results of metal vapor measurements are presented below.

A. Infrared Spectrometer System

Dr. C. Allemand and G. Hunter

In order to develop an understanding of heat transport, fluid convection and metal vaporization in arc weld pools, work has continued on a system to measure the surface temperature gradients across the weld pool. This will be achieved by use of an infrared microscope which has been designed during the previous year of study. Purchase and construction of the optical, mechanical and electrical components has progressed sufficiently during the past year that data collection can begin. The computer software necessary to calibrate the equipment and calculate the weld surface temperatures has been developed this past year and will be described subsequently.

The optical train components (see Figure 1) have been assembled and tested. The reflective mirror lens, which was designed to eliminate chromatic and spherical aberrations, has been completed. The scanners are now complete and

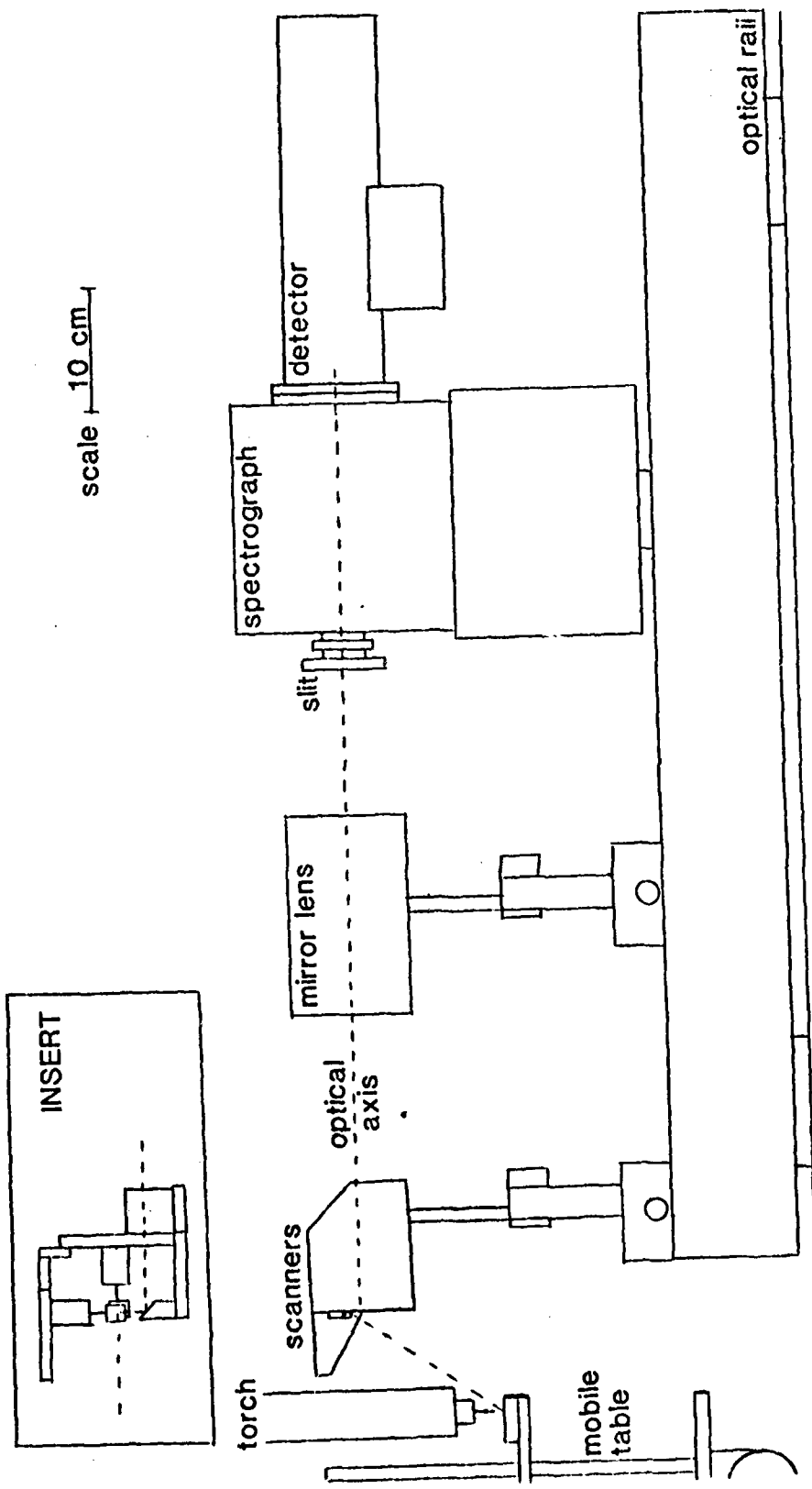


Figure 1: Side view diagram of the optical train with top view of the scanners inserted

will allow for faster scanning of the weld pool surface so temperature maps can be created. A rigid mobile welding station has been constructed so studies on both stationary and moving welds can be made.

The detector is connected to an Optical Multichannel Analyzer (OMA), which has been used to acquire data during the previous year of this study. The OMA has been linked to a DEC MINC 11/23 minicomputer (see Figure 2) for increased memory and data handling capability. The MINC will perform most of the system calibration, as well as calculate the surface temperatures from the spectral data gathered by the OMA.

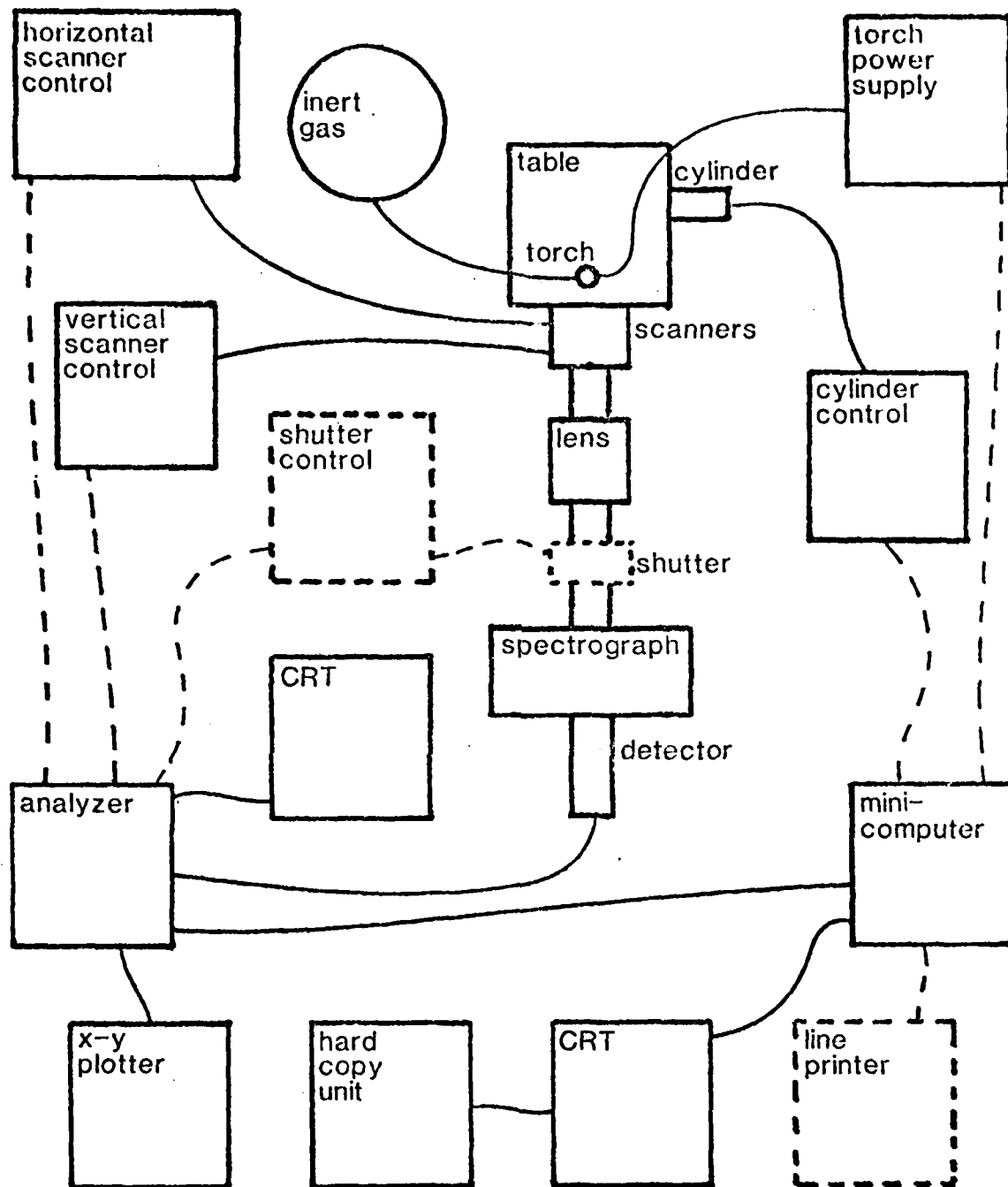
Initial experiments will be performed to measure the temperature at a single point on a stationary weld pool. Later experiments will attempt scanning measurements and moving welds as the capabilities of the scanners and the mobile table, controlled by the OMA and the MINC, are developed. Should the detector prove incapable of making accurate measurement within a millisecond (the approximate time constant of a target point), a shutter or chopper may also be required in the optical train to shorten the measurement time. In order to calculate the temperature of the pool from the spectral data and in order to reduce experimental error, computer software has been developed during the past year. The following section describes the general approach.

A thermal radiator, such as a weld pool surface, will emit spectral radiation accordingly to Plank's radiation law:

$$S = \epsilon C_1 \lambda^{-5} (e^{C_2/\lambda T} - 1)^{-1}$$

where S is the spectral radiant emittance, ϵ is the emissivity, λ is the wavelength of the radiation, T is the temperature of the emitter, and C_1 and C_2 are radiation constants. The emissivity is generally a function of material, temperature, wavelength, surface condition, and viewing position.

The OMA measures the spectral intensities at 500 different wavelengths. By



(dotted lines are proposed additions)

Figure 2: Block diagram of component linkages

the use of appropriate standards, the spectral intensities and channel numbers can be calibrated to spectral radiances and wavelengths, respectively. The MINC 11/23 computer can then fit the resulting curve to the calculated Planck curves to find a best fit for a particular temperature.

Since the material, temperature, surface condition, and viewing position are all constant at each target point, the emissivity will only vary with wavelength. Unfortunately, little is known about the emissivity behavior of liquid metals. A model for emissivity as a function of wavelength must be assumed in order to calculate the temperature by a curve fitting technique. The curve fitting procedures and programs developed during the past year are based on those of Bevington (1). One program has been developed that assumes a constant emissivity function with wavelength. This program is insensitive random proportional noise as shown by the examples in Figures 3 and 4. Other programs which have been developed during the past year assume an exponential emissivity function (2):

$$\ln \epsilon = \epsilon_1 + \epsilon_2 \lambda$$

or a quadratic emissivity function:

$$\epsilon = \epsilon_1 + \epsilon_2 \lambda + \epsilon_3 \lambda^2.$$

These programs perform a least squares fit with a linearization of the fitting function to calculate the emissivity coefficients and the temperature. A program is under development to take advantage of both the noise insensitivity of the first program and the non-constant emissivity behaviors of the other programs. Calibration of the detector with a black-body source should be completed during the spring after which measurement of weld pools may begin.

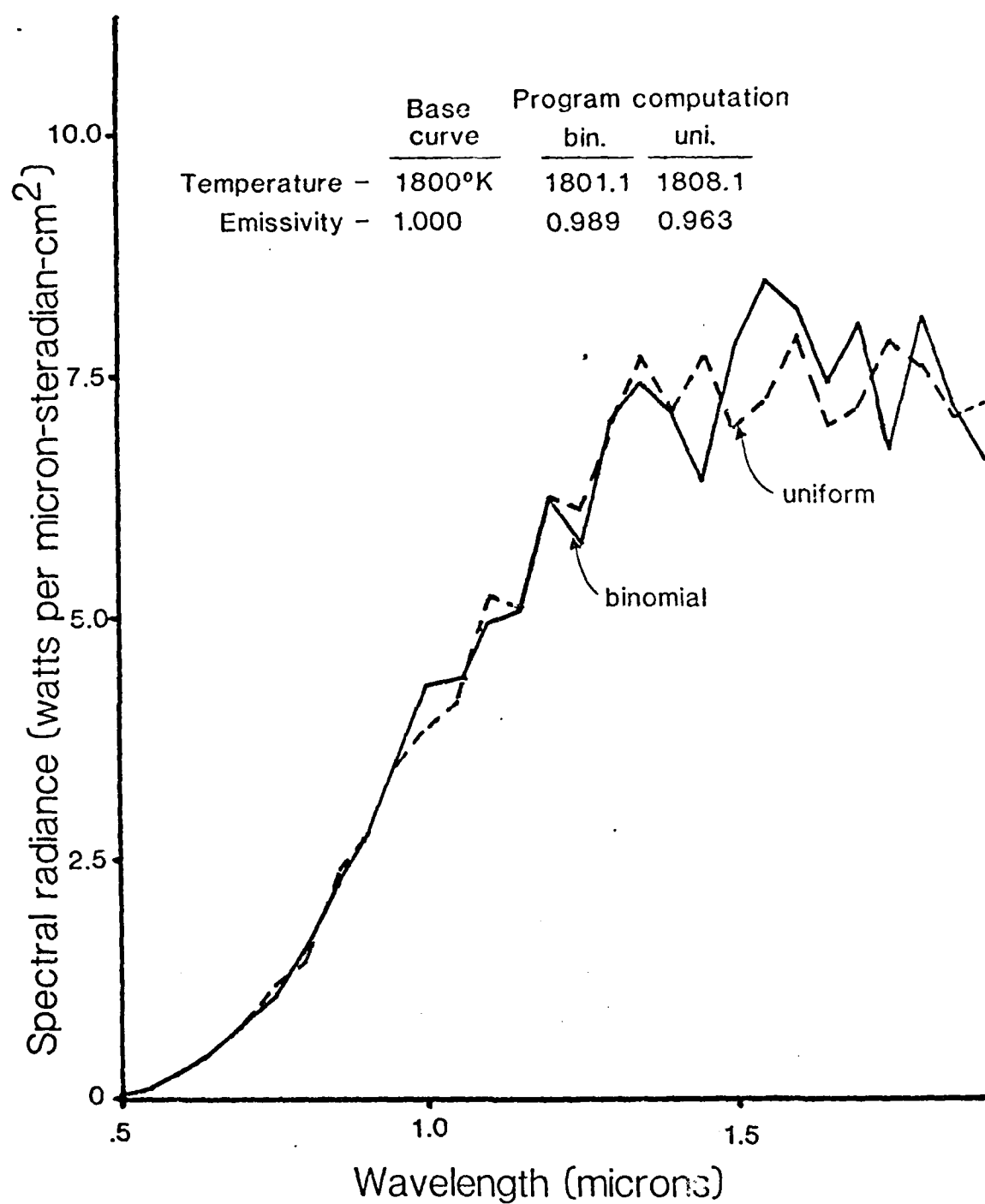


Figure 3: Plot of data with 6.8% rms noise used in curve fitting program

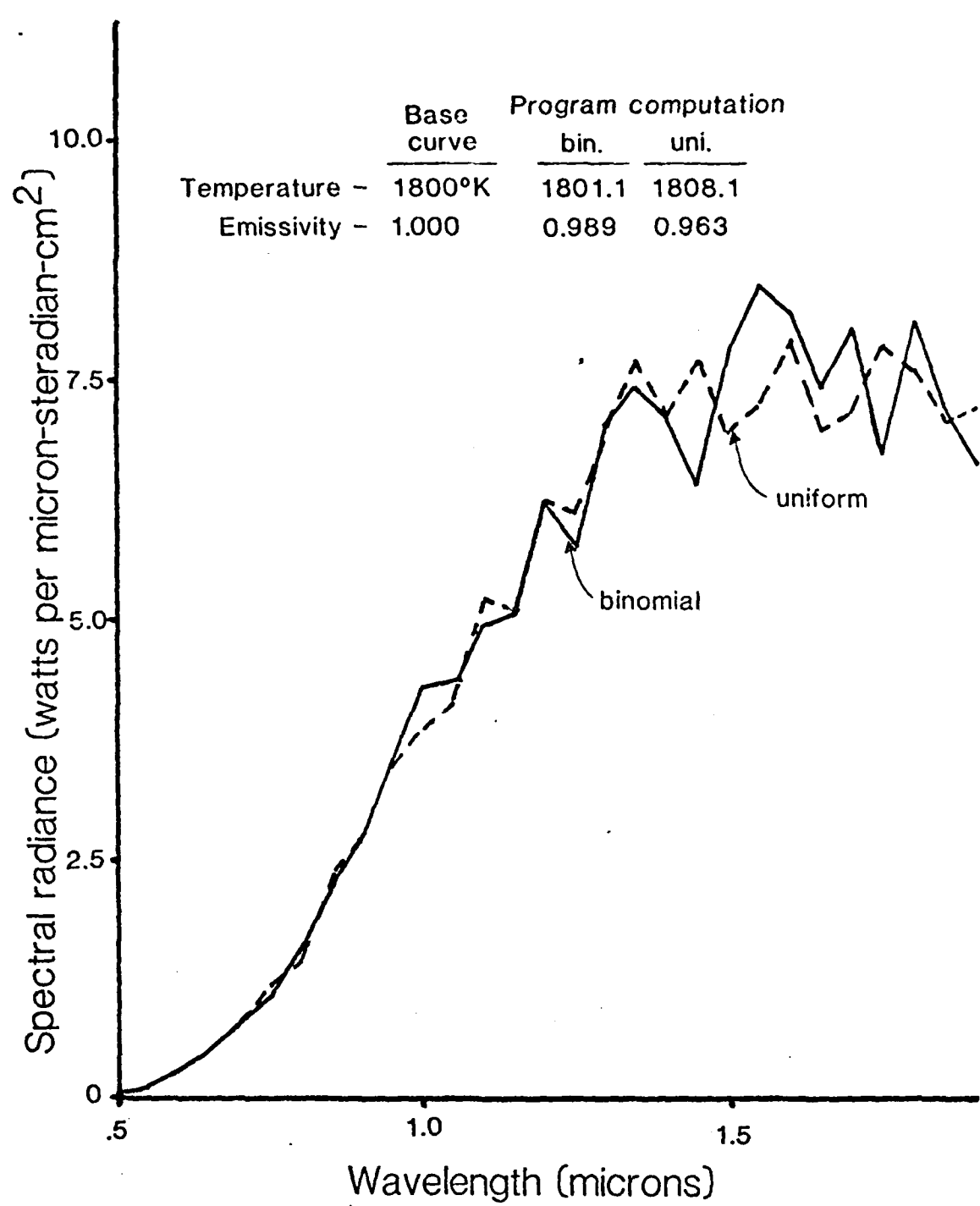


Figure 3: Plot of data with 6.8% rms noise used in curve fitting program

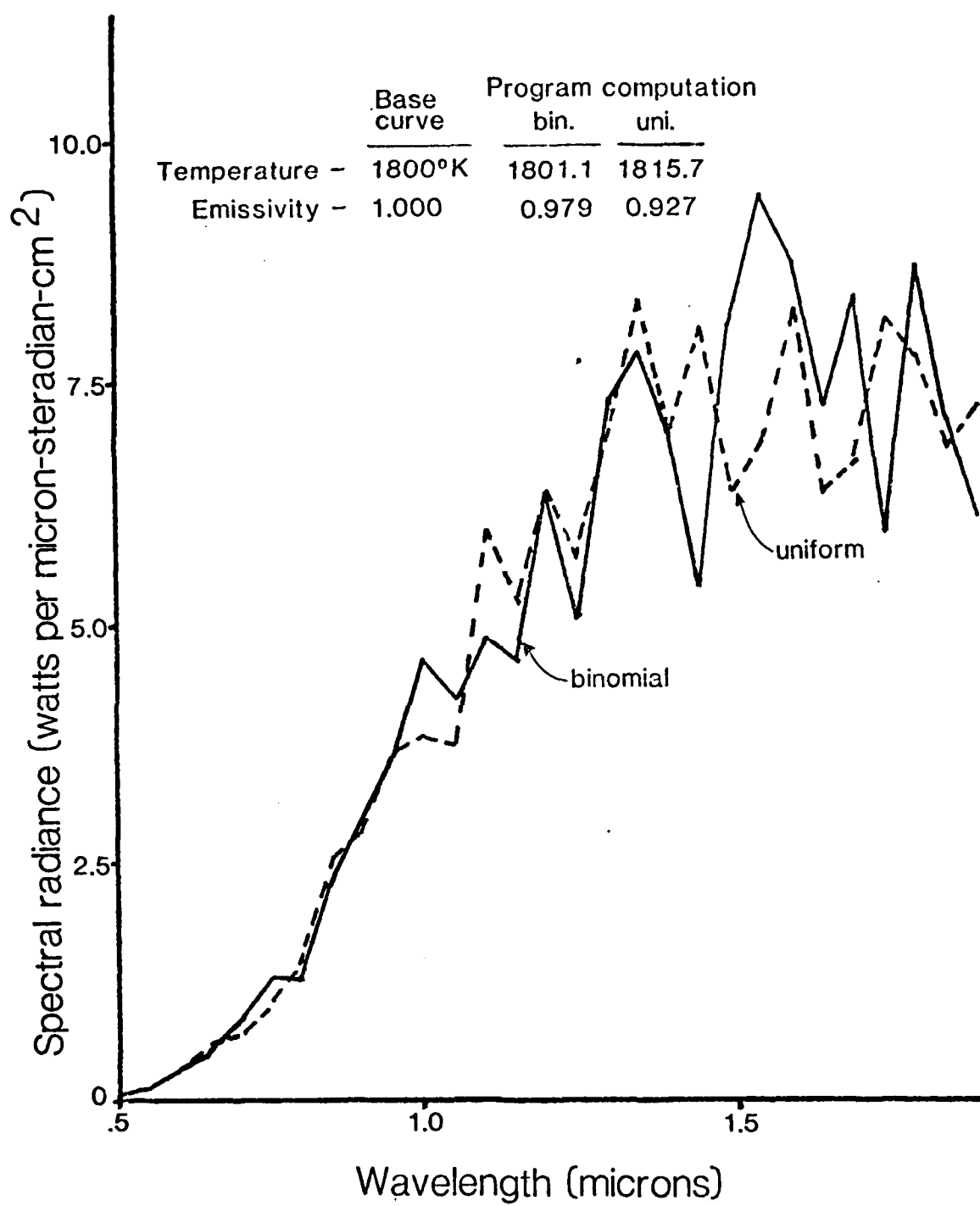


Figure 4: Plot of data with 13.5% rms noise used in curve fitting program

B. Measurement of Metal Vapors
in the Arc Plasma

Dr. A. Block-Bolten and G. Dunn

There is increasing evidence suggesting the importance of determining the species and concentration of metal vapors which are present in the welding arc. A thermodynamic model is presented in Appendix A which accounts for selective evaporation of metal vapor from a steel weld pool. Work is continuing on evaporation losses from aluminum and copper weld pools as well.

In order to measure the metal vapors present in the arc, a UV-visible optical train similar to the infrared system shown in Figure 1, has been constructed such that spectra can be recorded over a range of approximately 560 nanometers. A sodium salicylate ultraviolet scintillator has been placed in front of the detector to allow investigation in the ultraviolet wavelength range, previously impossible due to a lower detection limit of 360 nm in the OMA Model 1254 SIT vidicon detector.

Dark current background and linearity of response of the SIT detector have been studied for increased accuracy of the proposed quantitative analysis of the metal vapors. The research will use the scanners described in Section A above to determine the distribution of various metal vapors in the arc.

Spectra have been recorded for 304 stainless steel over the entire spectral range of 560 nm and for titanium 6Al-4V over approximately half of this range. The effects of different shielding gases and electrodes have also been investigated. In the stainless steel spectra (Figure 5), argon, iron, manganese, calcium, chromium and tungsten lines have been identified. In the titanium spectra (Figure 6), argon, titanium, aluminum, calcium and tungsten lines have been identified.

The calcium lines are a subject of great interest because evidence suggests that this calcium vapor is being emitted by the tungsten electrode. Savitskii and Leskov (3) reported that even a very small amount of Ca in the arc can significantly alter weld bead shape. For this reason, an investigation of different tungsten welding electrodes is being conducted. Electrodes are being obtained from all four major U.S. manufacturers. These will be compared with pure tungsten, tantalum and graphite electrodes. In addition, a sample of high-Ca stainless steel is being obtained from Republic Steel Corp. It is hoped that these studies will lead to an explanation of the mechanics of Ca interaction in the arc.

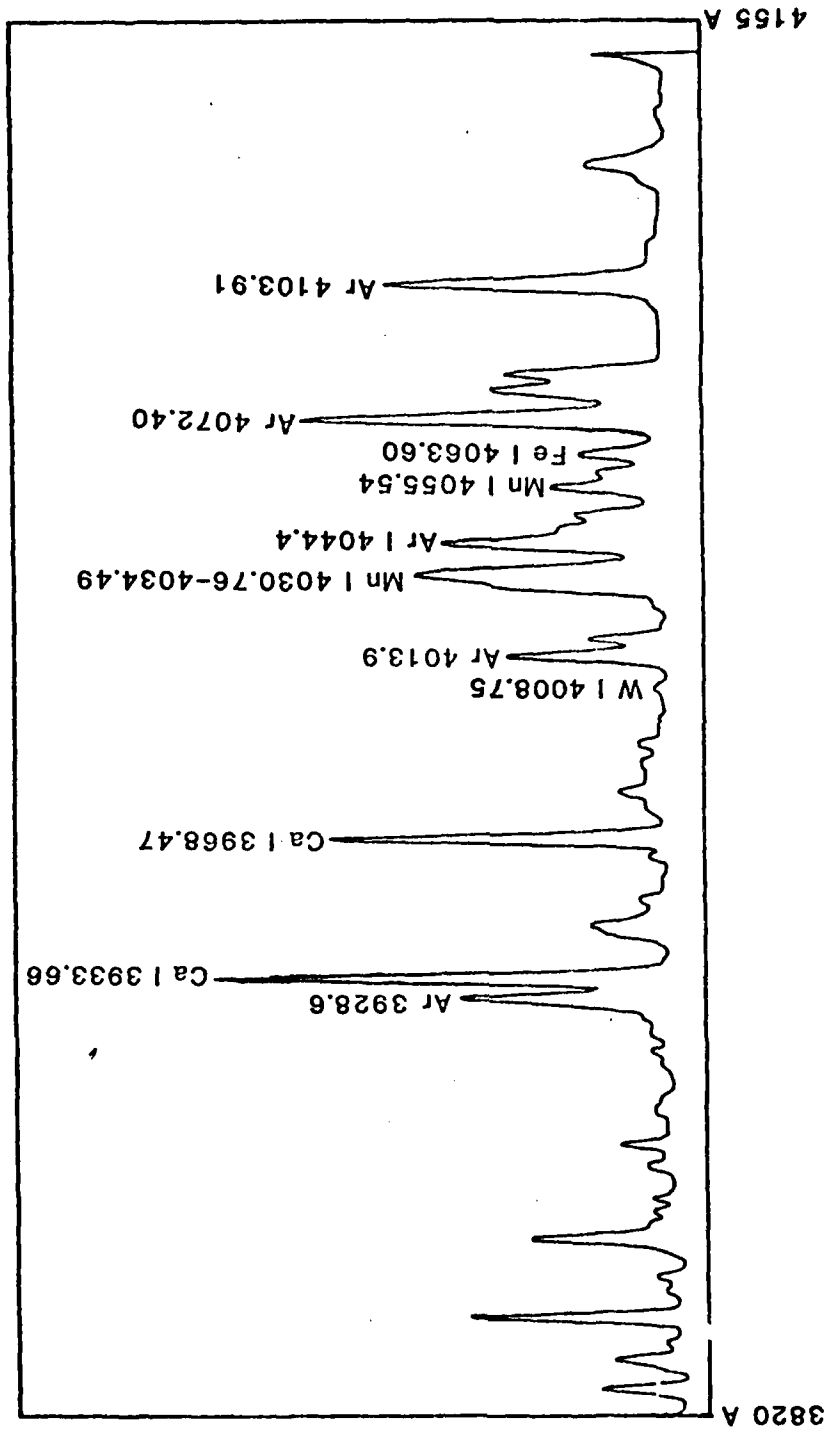


Figure 5: Spectrum for Stainless Steel

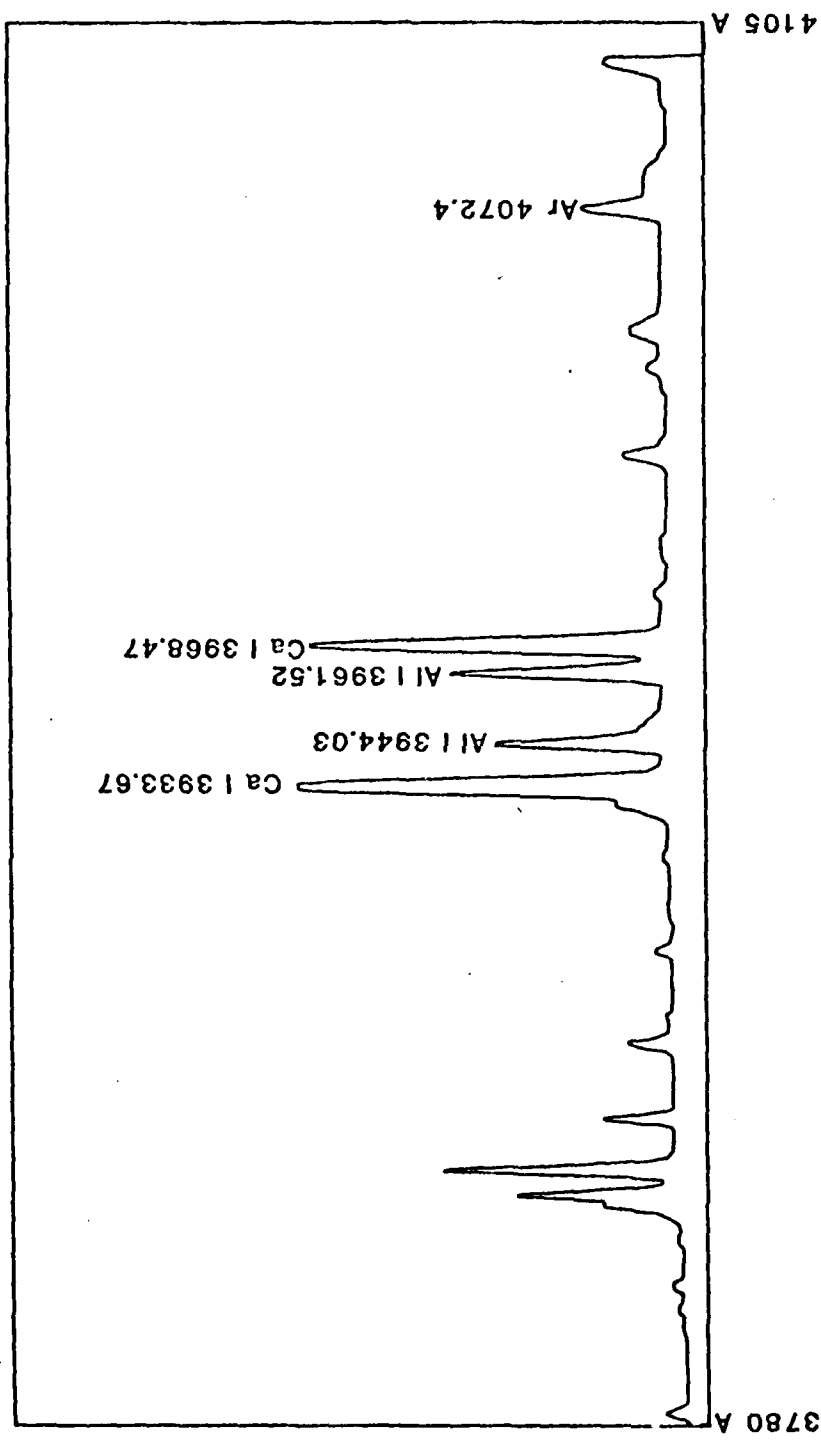


Figure 6: Spectrum for Titanium

2. JOINING OF HEAVY SECTION TITANIUM

Research on heavy section titanium has concentrated on two processes, viz. electroslag welding and pulsed current gas-metal-arc welding . Electroslag welds have been produced during the past year while the equipment and facilities for gas-metal-arc welding have been designed and built.

A. Electrosag Welding of Titanium

S. K. Fan, A. Lynch, Prof. T. DebRoy, Dr. A. Block-Bolten

A modified electroslag welding apparatus using movable copper shoes was constructed and tested successfully on steel plates. Attempts to weld one-inch thick titanium 6-Al-4V with CaF_2 flux were unsuccessful. The weld pool was stable but the electrode melting rate was three to four times greater than that experienced with steel electroslag welds. As a result, the weld metal did not have sufficient time to fuse to the sidewalls and the "weld" was more like a casting made between the two plates. Metallography and hardness tests of the deposited metal revealed a finer microstructure than was present in the base plates and an equivalent hardness.

A computer heat flow analysis of titanium electroslag welding was performed by Prof. T. DebRoy of Pennsylvania State University under a subcontract. Figures 7 through 10 show the results of several of his seven trials. Figure 7 is a plot the local heat generation pattern in an electroslag pool of 4.4 cm plate gap using 800 amperes and 20 volts on a 2.5 cm thick plate. Due to the low electrical resistivity of the CaF_2 slag, most of the heat is generated near the welding electrode, which causes it to melt rapidly. Under the conditions of

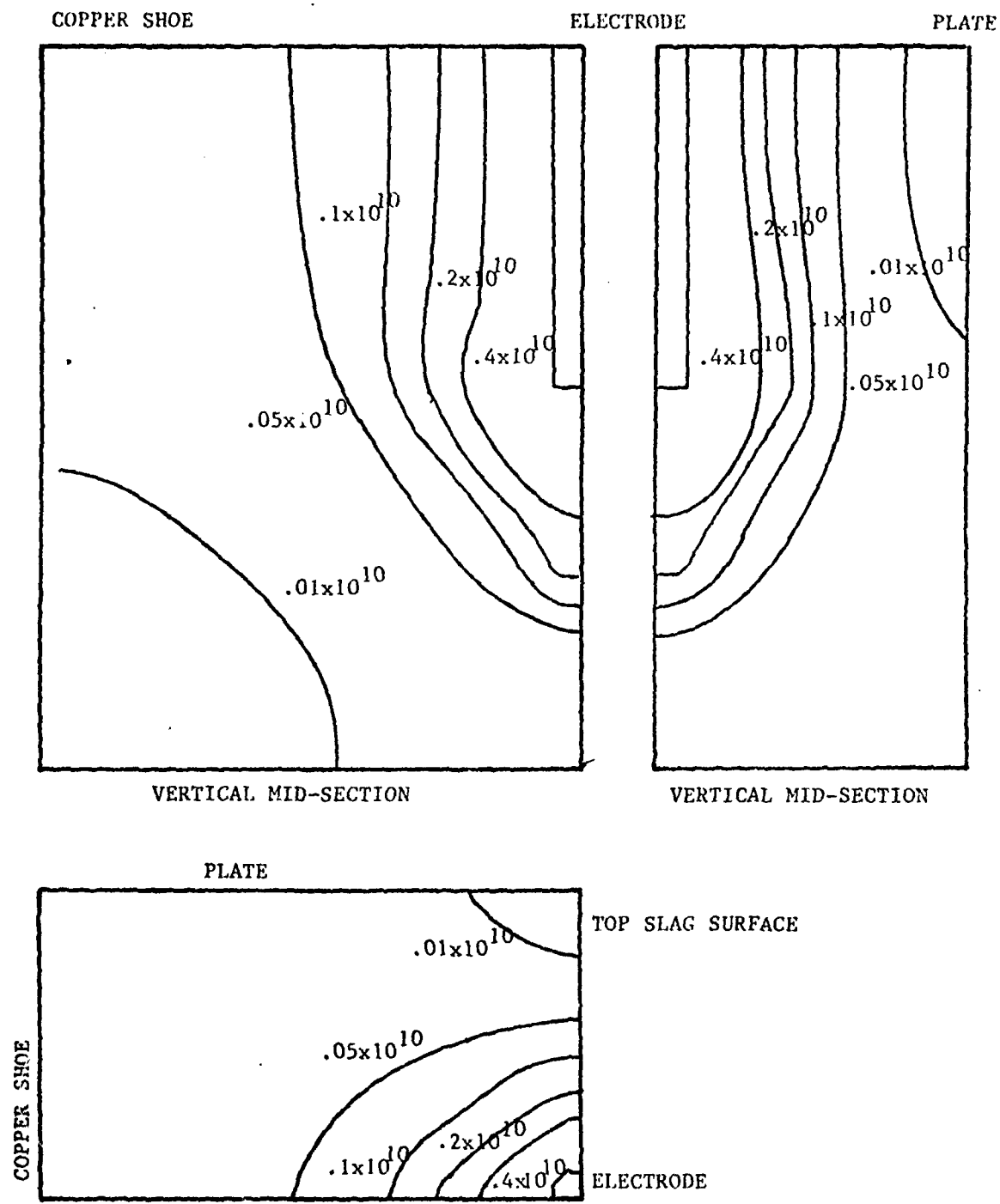


Figure 7

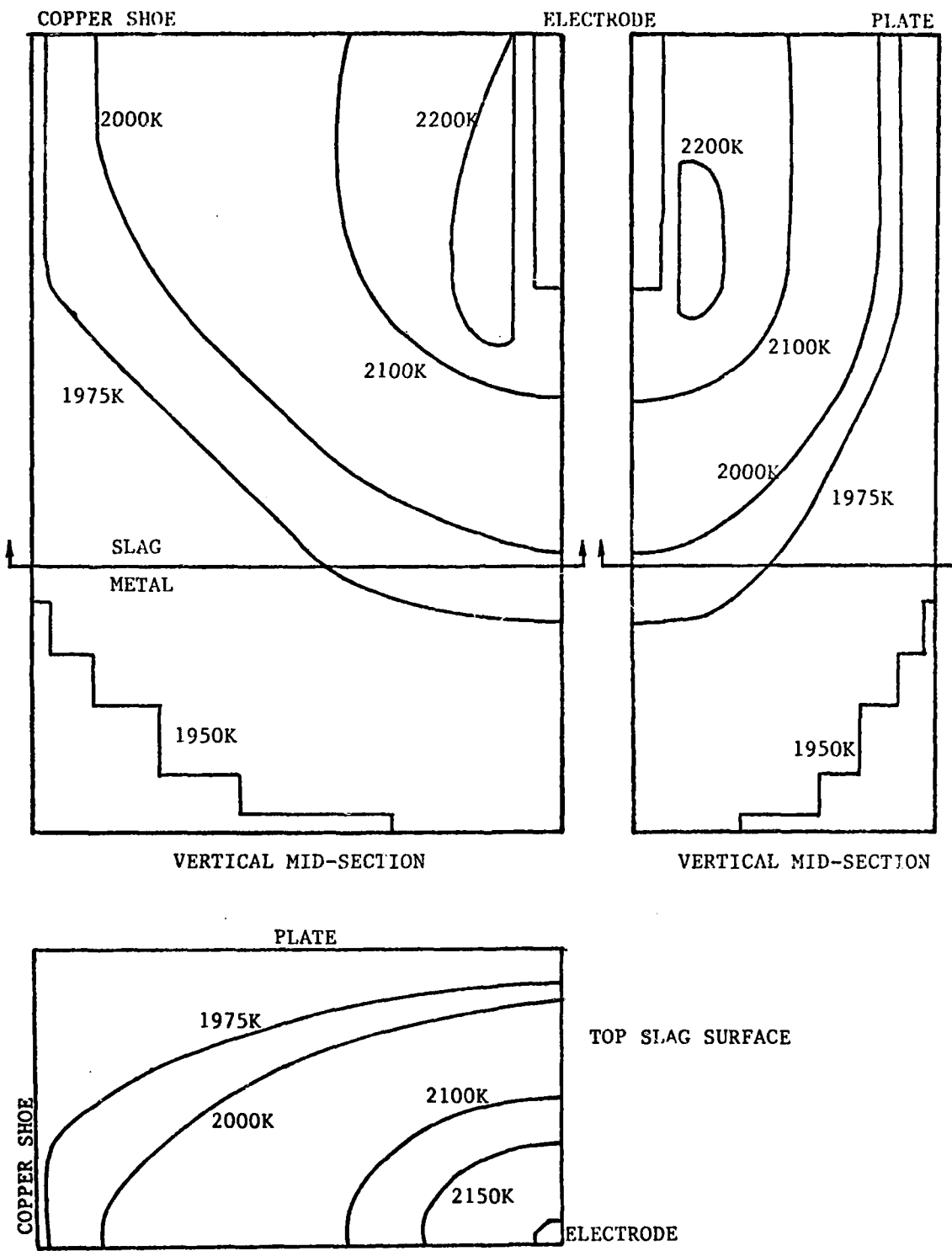


Figure 8

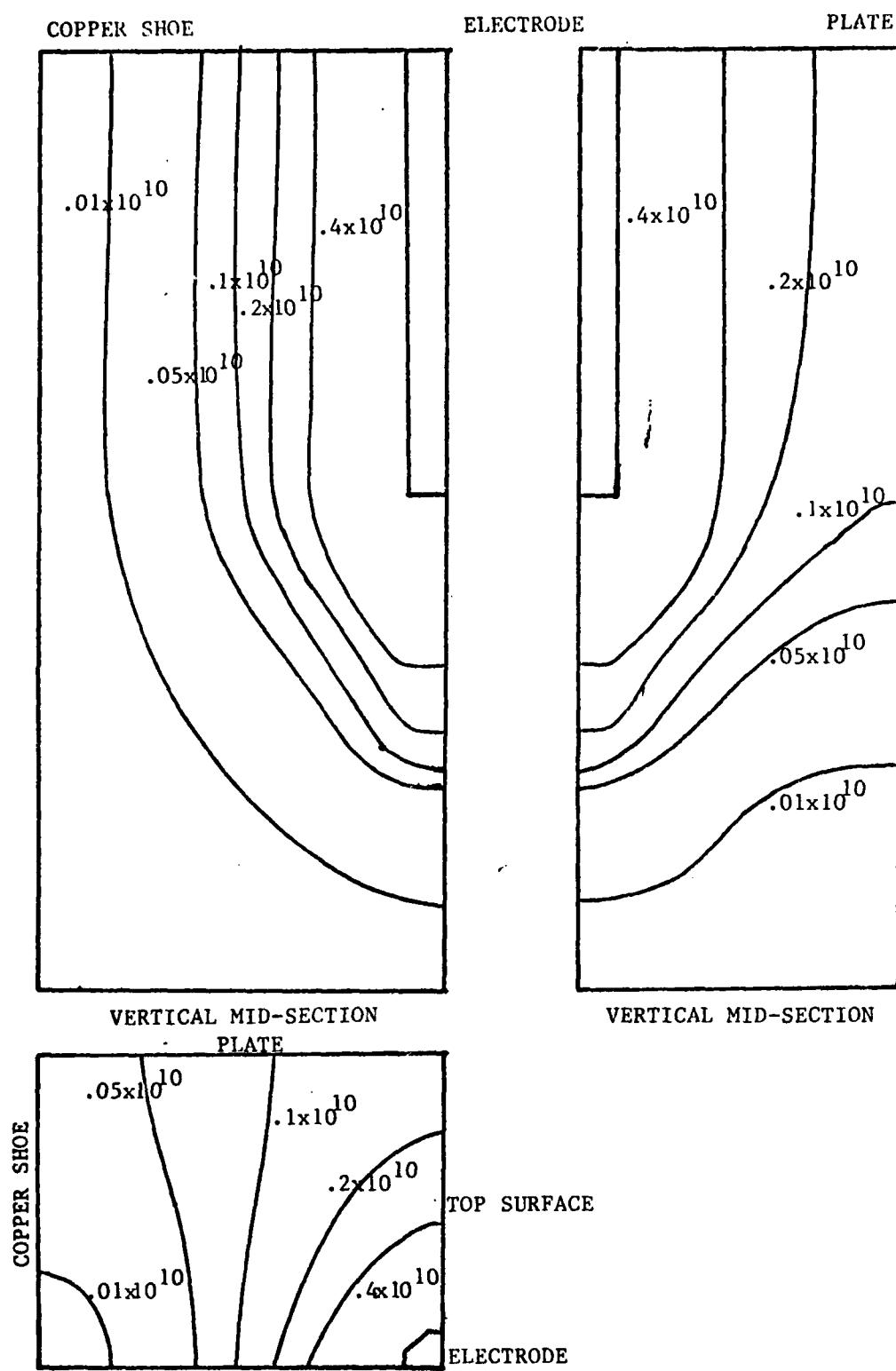


Figure 9

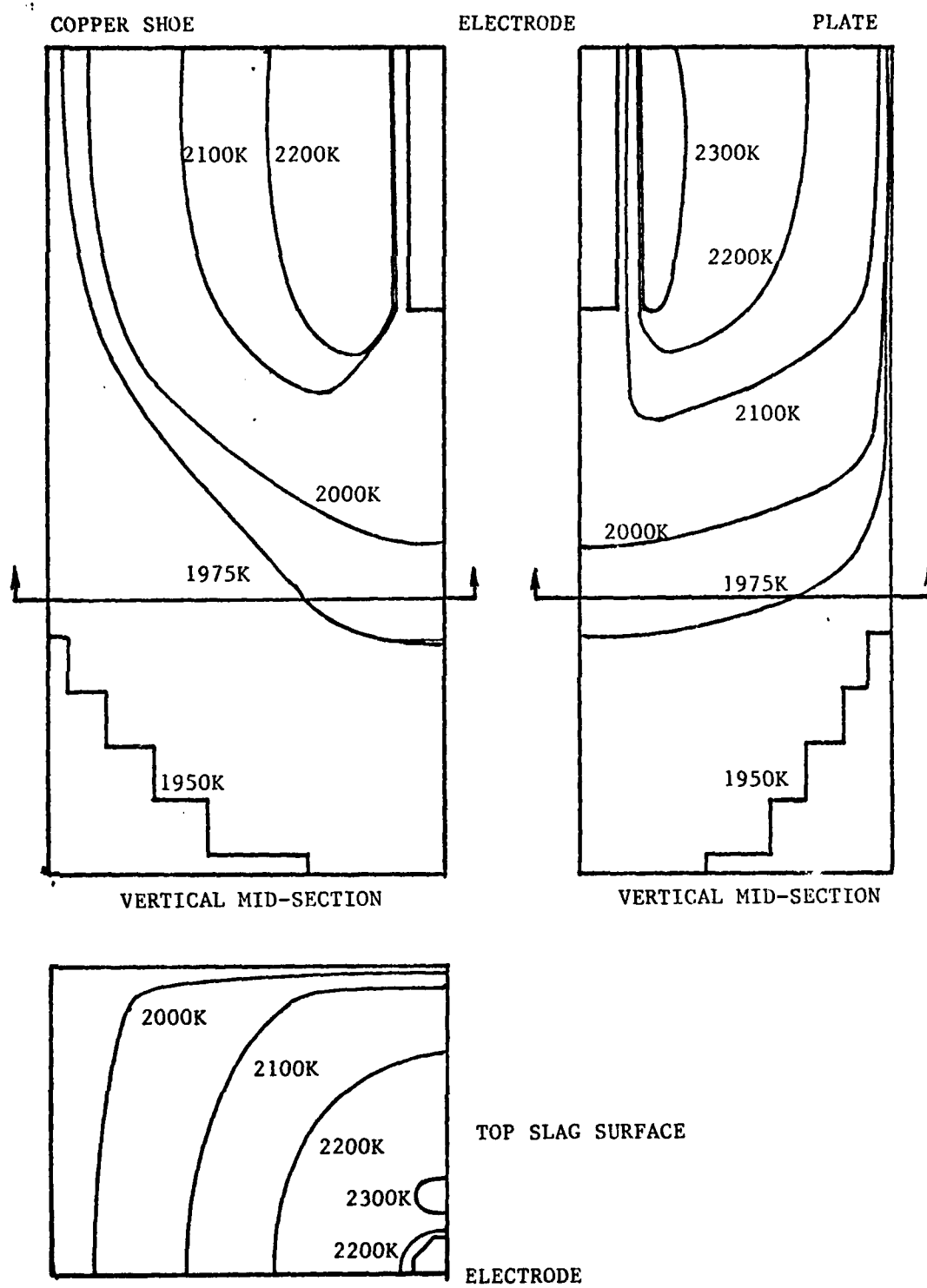


Figure 10

this calculation only 0.5 percent of the heat was transferred to the base plates. Figure 8 shows the calculated temperature distribution for the same system as Figure 7. The low temperature gradients clearly do not transport enough heat to fuse the sidewall.

Calculations were performed to test the effect of increased slag resistivity and decreased plate gap on improving the sidewall fusion. Figure 9 shows the improved heat generation pattern under these conditions, while Figure 10 shows much steeper temperature gradients in the slag phase which were calculated to transport 25 percent of the total heat to the baseplates. This was achieved by decreasing the plate gap to 2 cm and increasing the slag resistivity by 20 percent.

A thermodynamic assessment of potential fluxes for electroslag welding of titanium (4) has shown that MgF_2 and SrF_2 should have significantly higher electrical resistivities than pure CaF_2 . Studies using SrF_2-CaF_2 fluxes have begun and have produced significantly more sidewall fusion than pure CaF_2 fluxes.

B. Gas Metal Arc Welding of Titanium

D. Ries and R. Schoder

Gas metal arc welding is an attractive process for joining of titanium in all positions. Unfortunately, contamination can be a problem when operating in the spray transfer mode, and lack of fusion is a problem in the globular transfer mode. One possible improvement is pulsed current welding with one metal droplet per pulse which combines some of the advantages of spray (high deposition rate) and globular transfer. This process is sometimes referred to

as synthetic spray transfer. The major difficulty is that the study requires a transistorized welding power supply which is not commercially available. Such a supply was ordered early in 1981 and delivered a year later. This apparatus was specially designed for the MIT Welding Laboratory by Alexander Kusko, Inc. A paper describing the features of this equipment is given in Appendix B.

In order to monitor metal transfer across the arc, a gas-metal arc welding system has been constructed inside a glove box, and a high-speed camera using laser backlighting has been constructed. Welding tests using aluminum have confirmed the usefulness of the laser backlighting, the transistorized power supply and the glove box welding station. Titanium welds will be made in the near future.

The backlighting system involves the use of a 5 milliwatt He-Ne laser, a diaphragm, a 6328°A narrowband pass filter, and two 100 mm focal length lenses. These components are arranged as in Figure 11. The system functions by producing a shadow graph of the electrode of droplet formation and of droplet transfer. The optical system serves to filter any arc light from the shadow graph so that all pertinent information is carried by the laser and the intense arc light is not observed. This is achieved by shining the expanded laser beam through the welding arc, then focusing it with a 100 mm focal length converging lens, passing it through the diaphragm and then through the filter. The arc light is excluded by intercepting arc light entering the 100 mm lens and focussing it at a point different from the point at which the coherent (laser) light is focussed. Any remaining arc light that passes through the diaphram is removed with the 6328°A narrowband filter. It is true that a small fraction of arc light will pass through the filter, but the light intensity is small enough so that it is negligible compared with the laser intensity and has no effect on the performance of the optical system.

as synthetic spray transfer. The major difficulty is that the study requires a transistorized welding power supply which is not commercially available. Such a supply was ordered early in 1981 and delivered a year later. This apparatus was specially designed for the MIT Welding Laboratory by Alexander Kusko, Inc. A paper describing the features of this equipment is given in Appendix B.

In order to monitor metal transfer across the arc, a gas-metal arc welding system has been constructed inside a glove box, and a high-speed camera using laser backlighting has been constructed. Welding tests using aluminum have confirmed the usefulness of the laser backlighting, the transistorized power supply and the glove box welding station. Titanium welds will be made in the near future.

The backlighting system involves the use of a 5 milliwatt He-Ne laser, a diaphragm, a 6328°A narrowband pass filter, and two 100 mm focal length lenses. These components are arranged as in Figure 11. The system functions by producing a shadow graph of the electrode of droplet formation and of droplet transfer. The optical system serves to filter any arc light from the shadow graph so that all pertinent information is carried by the laser and the intense arc light is not observed. This is achieved by shining the expanded laser beam through the welding arc then focusing it with a 100 mm focal length converging lens, passing it through the diaphragm and then through the filter. The arc light is excluded by intercepting arc light entering the 100 mm lens by focussing it at a point different from the point at which the coherent (laser) light is focussed. Any remaining arc light that passes through the diaphragm is removed with the 6328 A narrowband filter. It is true that a small fraction of arc light will pass through the filter, but the light intensity is small enough so that it is negligible compared with the laser intensity and has no effect on the performance of the optical system.

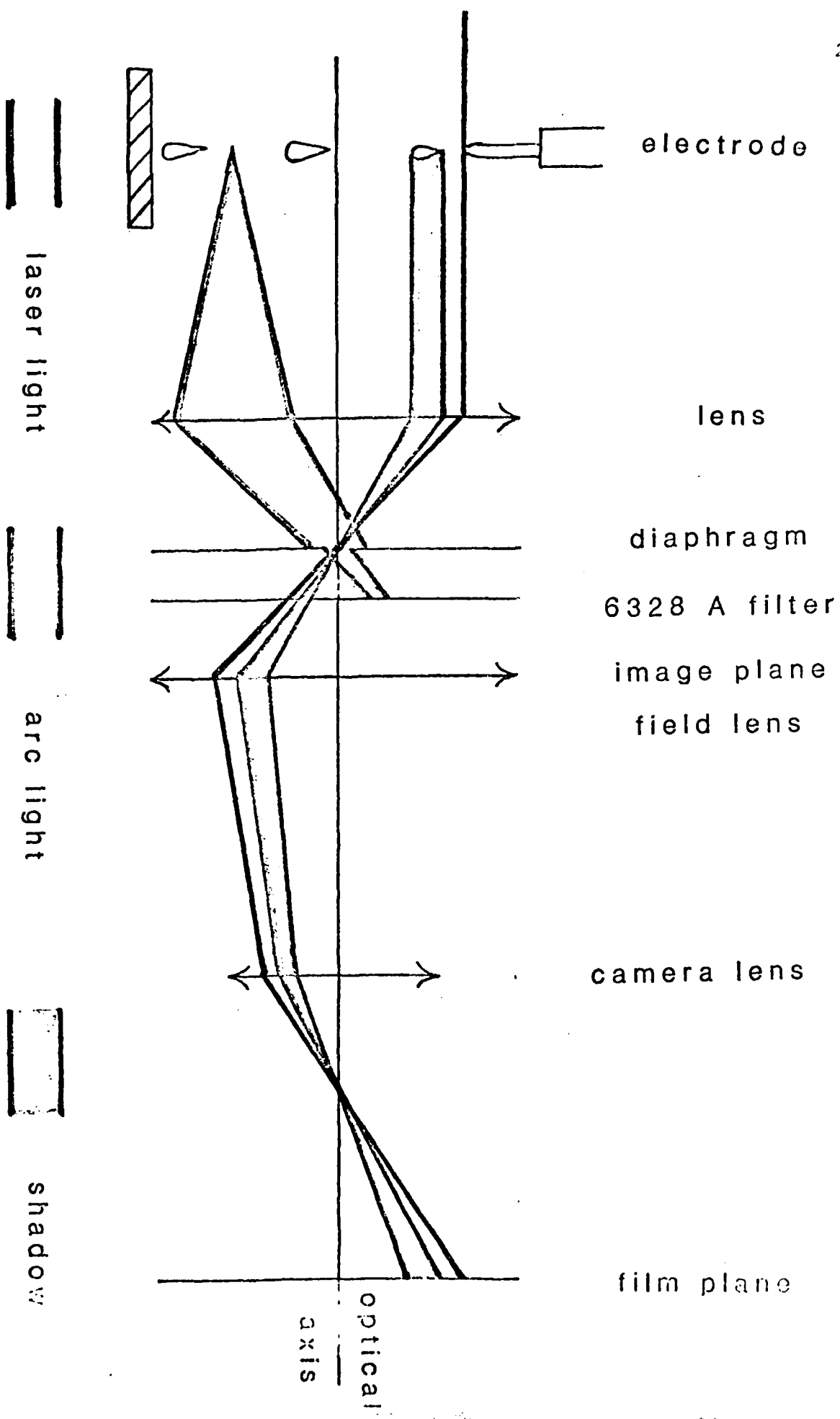


Figure 11: Laser Backlighting Theory

The second 100 mm focal length converging lens is placed at the image plane of the first lens. The second lens serves to change the laser light from its divergent nature (caused by the first lens) to a converging beam which can be focused by a camera lens.

Studies with different films have produced acceptable pictures of the droplet transfer at up to 3000 fps (frames per second). Densitometer exposure measurements indicate that pictures at speeds to 40,000 fps are practical with ordinary Tri-X film. It is doubtful, however, that such high speed will be necessary.

3. FRACTURE TOUGHNESS OF HY-80 WELD METAL

A. Submerged Arc Welding

B. Wilson

During the past year, a cooperative program has been developed with General Dynamics Electric Boat Division to study the factors influencing fracture toughness of submerged arc weld deposits. Over thirty welds were made at varying voltage, current and travel speed at heat inputs from 20 to 42 kJ per centimeter using two commercial fluxes. The experiment has been designed to allow statistical analysis of the results. As shown in Figures 12 and 13, there is no correlation of weld fracture toughness with welding heat input; however, higher welding currents do improve the toughness. An attempt is being made to correlate these results with weld deposit chemistry. Work at MIT on an NSF sponsored program is being used to explain the differences in manganese recovery with each flux. Later work is planned to study the transformation behavior of the weld metal.

B. Effect of Nitrogen Contamination on Strain Ageing

in HY-80 Weld Metal

O. Boydas

A second program developed with General Dynamics seeks to explain the loss of fracture toughness which occurs on the first side of a double V weld joint. It is hypothesized that strain ageing may be the cause. During the latter part of the year, an internal friction apparatus has been constructed to study the

ISO CHARGE ENERGY

LINCOLN 800

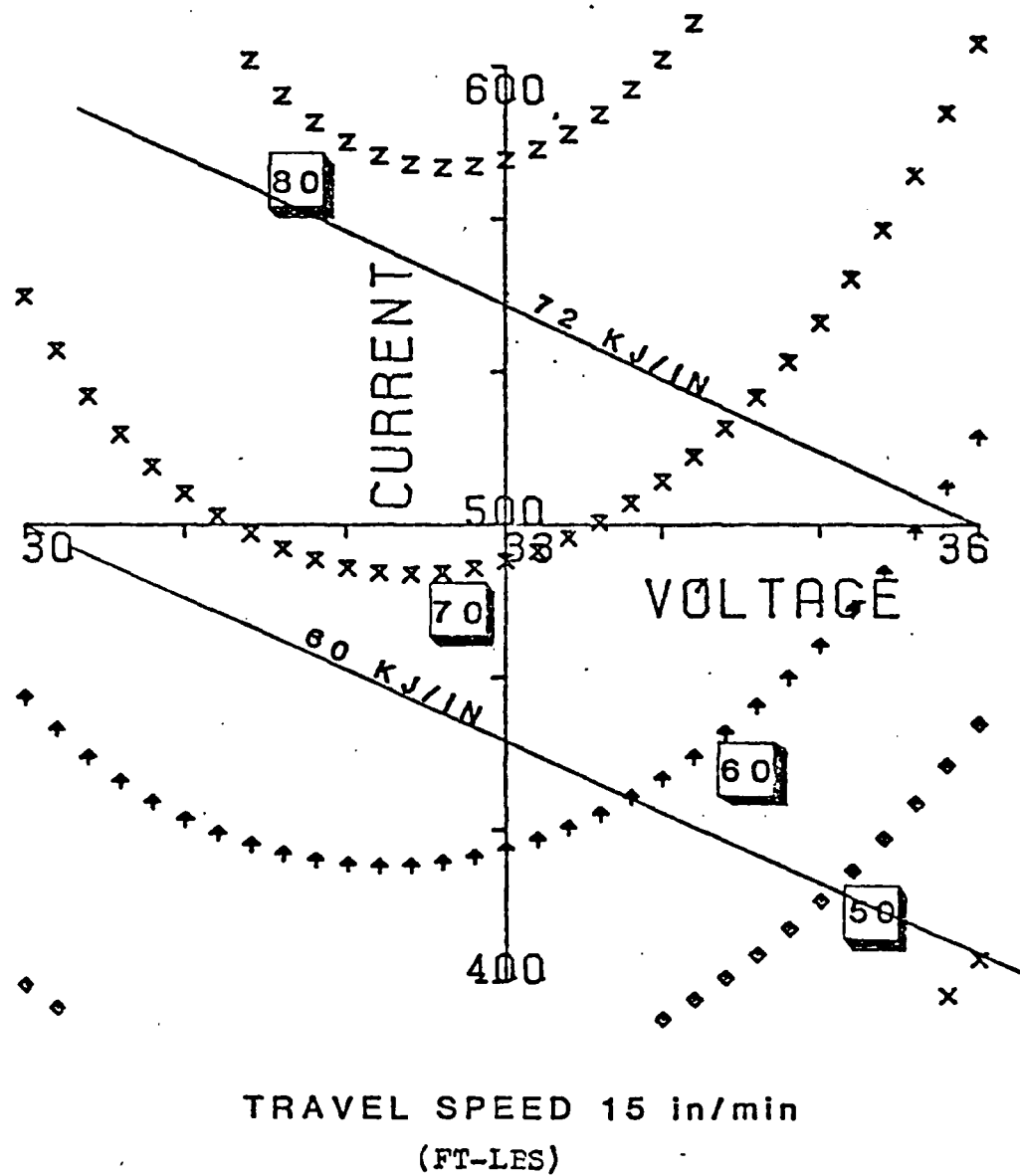
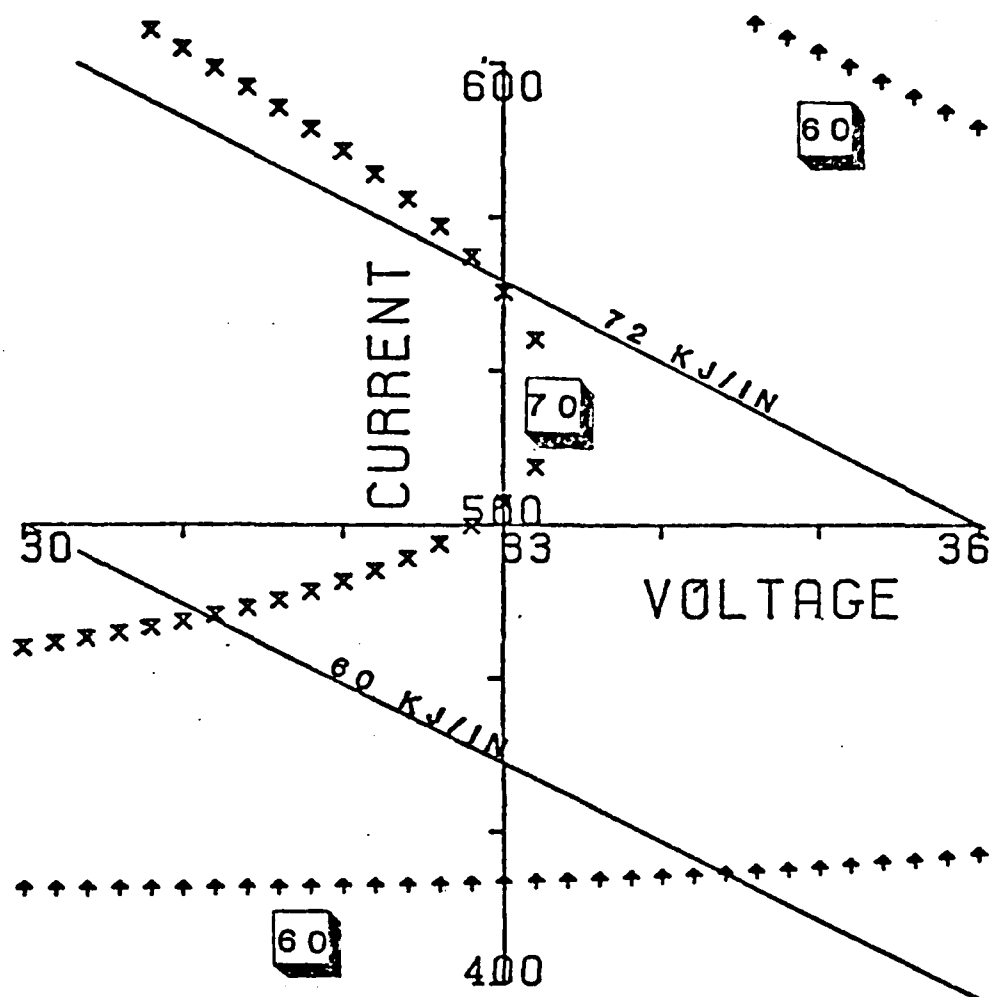


Figure 12

ISO CHARPY ENERGY

OP 121 TT



TRAVEL SPEED 15 in/min
(FT-LES)

Figure 13

effect of nitrogen of the weld metal. A number of plates have been welded by SAW and GMAW with differing nitrogen content, but no results are available at present.

4. SENSORS FOR AUTOMATED WELDING

Perhaps the greatest improvements needed to automate welding processes are new sensors. During the past year three sensor techniques have been studied. One involves the imaging of the weld pool surface to determine the shape of the surface depression. Another uses ultrasonics to measure the size of the liquid weld pool and a third uses variations in the arc voltage to detect changes in the process.

A. Imaging of Weld Pool Surface Depression

by Structured Laser Light

M. Lin and Dr. C. Allemand

The shape of the weld pool is determined in part by the depression of the surface. In this investigation, a photographic method is tested as a means of measuring the shape of surface depression. In this approach, the main difficulty comes from the high intensity of arc light which makes the weld puddle difficult to detect. After examining the spectrum of pure argon arc on AISI 304 stainless steel, as shown in Figure 14, a 4689A narrow band pass filter was chosen to block out the high intensity arc light.

A 35mm SLR Cannon F-1 camera with a narrow band pass filter attached in front of a f/2.8 135mm lens was used in this experiment. In order to magnify the image of the weld puddle, six M20 extension tubes were added to the camera. In addition, due to spatter from the puddle, a piece of glass was placed in front of the filter to protect the filter and lens.

Kodacolor ASA 100 was chosen as the film. Infrared film was also tried. As

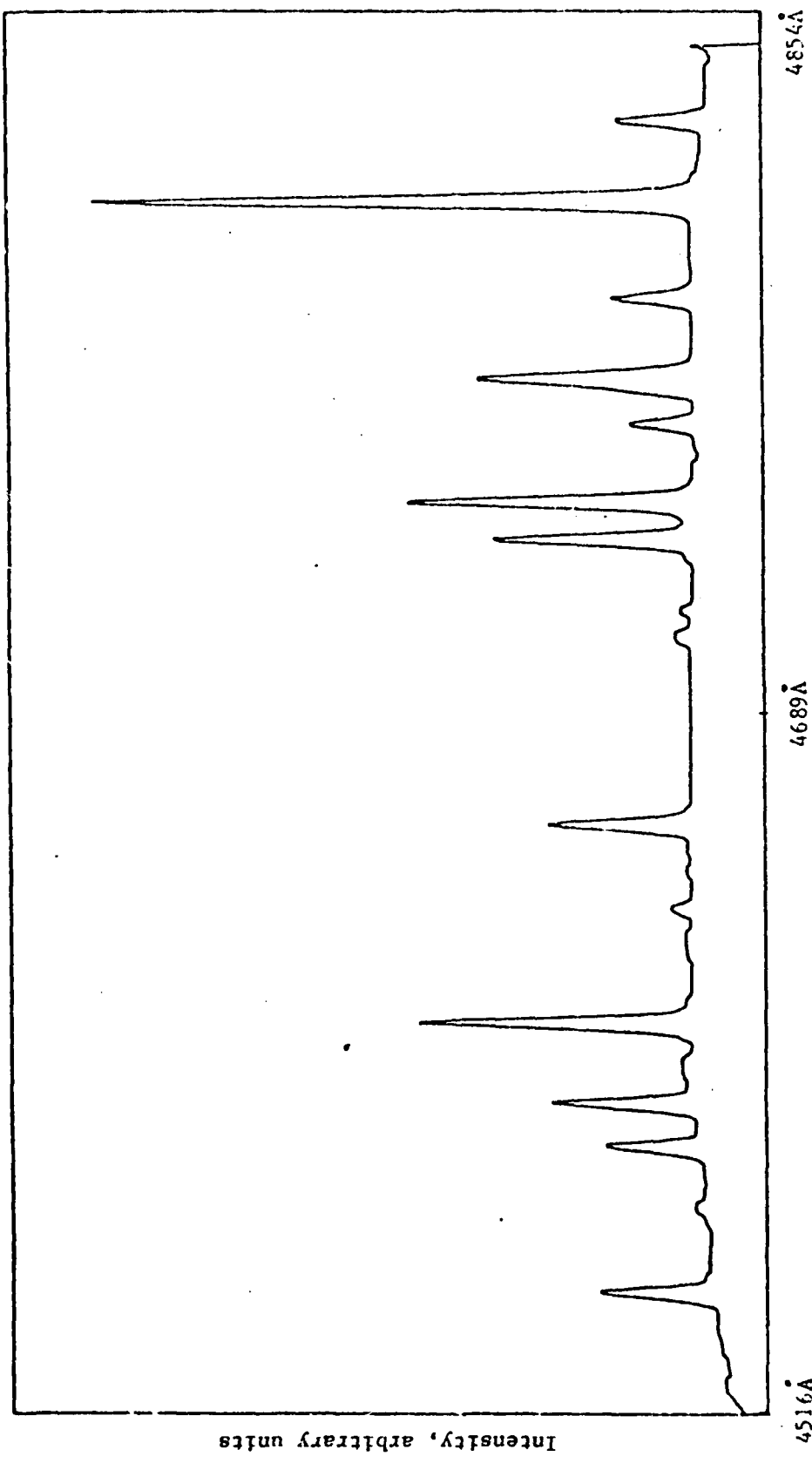


Figure 14: Spectrum of pure argon on AISI 304 stainless steel

the temperature increases, the maximum emission occurs at progressively smaller wavelengths. At the weld pool temperature of approximately 2800°K , the maximum gray body radiation occurs below one micron, and infrared film may sense more reflected light from the surface of the weld pool. Unfortunately, no appreciable improvement in the quality of the image of the weld pool was found when infrared film was used.

A stereoscopic viewer was also used to determine the depth of surface depression. Such a viewer is designed to measure three dimensional images from two photographs made of the object from different reference points, if the eyes can be separated so that each eye is seeing only one photograph. However, in application of this photogrammetric analysis, one of the two photographs is generally shot directly above the object and the other is taken at a very sharp inclination angle. This makes the application of the stereoscopic viewer in the welding experiment difficult, because the position of the weld head excludes the possibility of mounting the camera right above the weld pool. A number of errors are produced when both photographs are inclined.

As an alternate to stereophotography, imaging of the weld pool surface using structured laser light was also attempted. From the information on the photograph of such structured light, the shape of the weld puddle can be calculated. As a first step, a truncated ball bearing was used to simulate the geometry of a crater on the liquid pool*. The setup is shown in Figure 15. A grid pattern was produced by shining through a uniform wire mesh. A Melles Griot 5mW helium neon laser head with Spectra-Physics model 338 beam

* It should be noted that the image of a convex and a concave object using structured light produces an essentially equivalent picture.

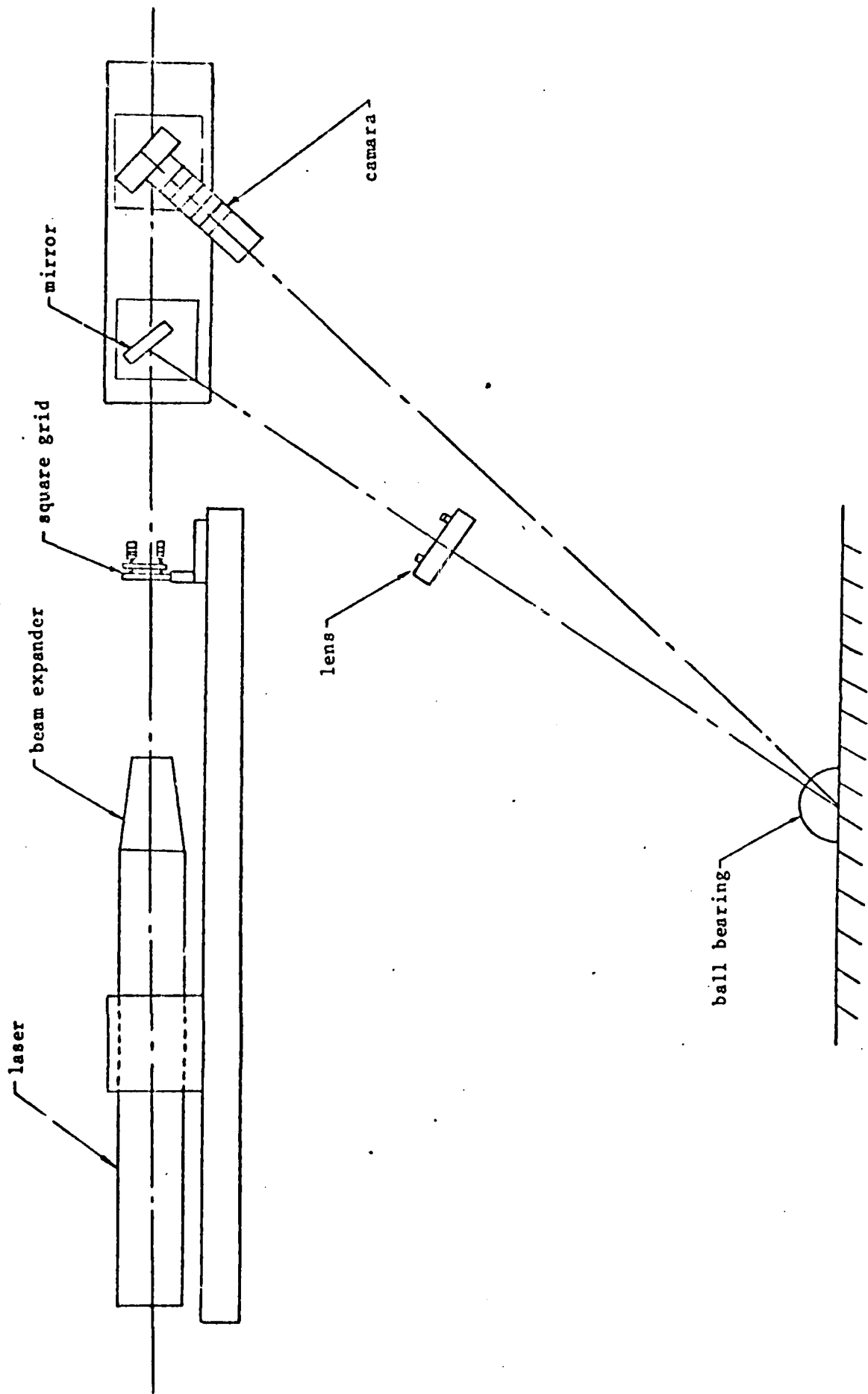


Figure 15: The setup of laser imaging using structured lights.

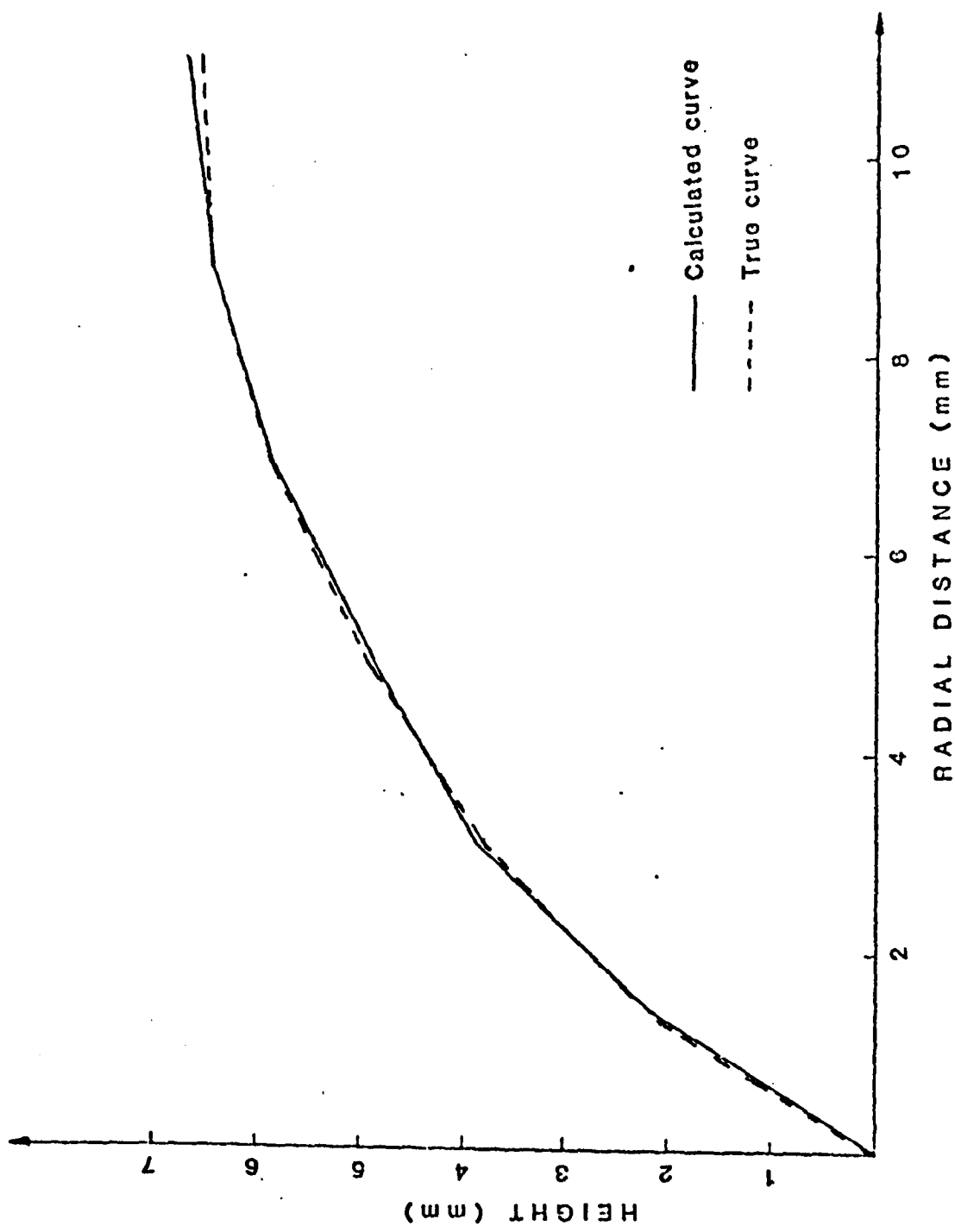


Figure 16: Result of the calculated curve and the true curve of ball bearing.

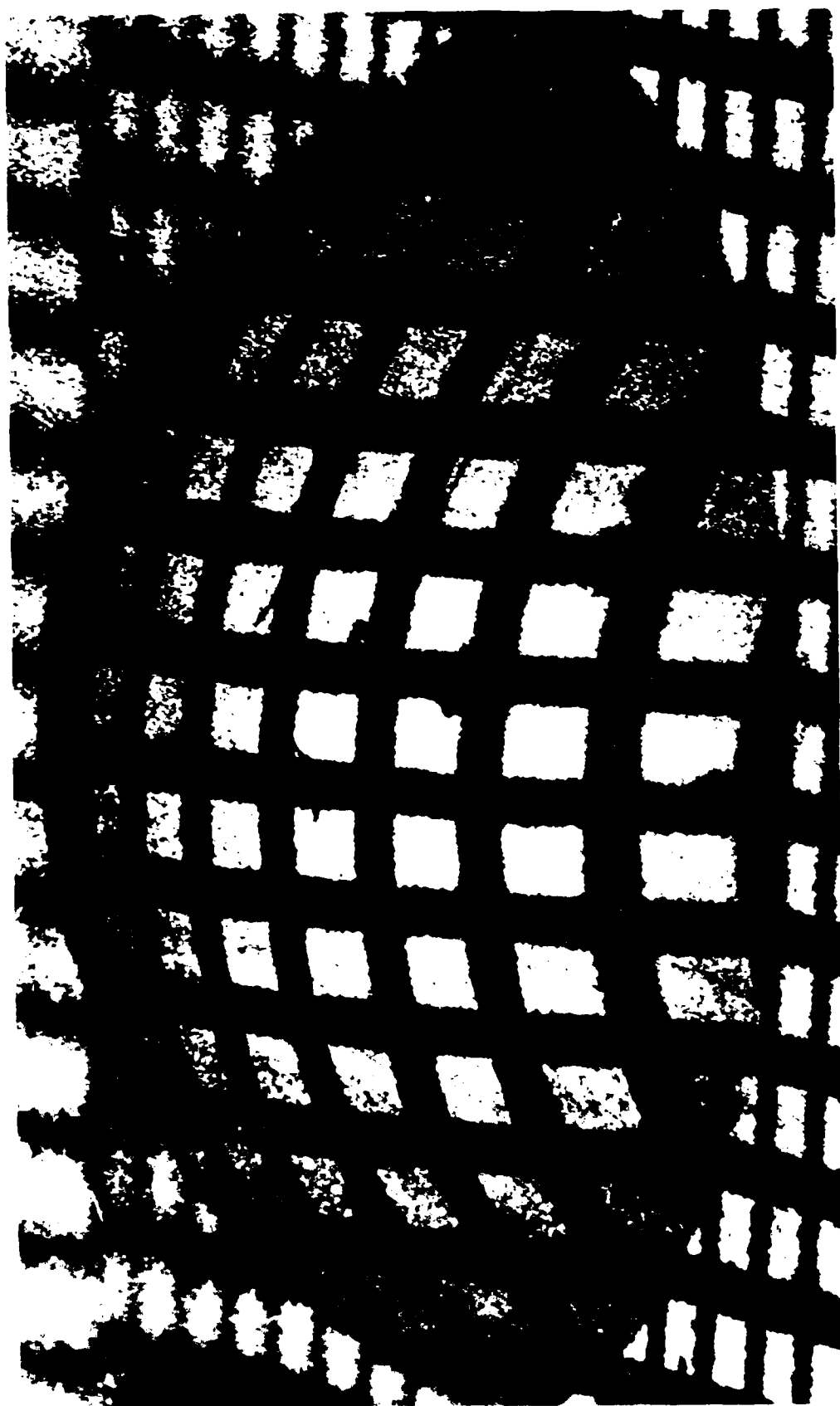


Figure 17: Square grid projected onto section of ball bearing with HeNe laser

expanding telescope was used. This gives a beam diameter of 30mm. The laser, grid, mirror and camera are all mounted on an optical rail which allows the alignment to be coplanar. Both the mirror and the camera are mounted on rotary stages which allow adjustment of the inclination angle. The image of the distorted pattern on the truncated ball bearing is then taken by the camera.

Results of Structured Light Measurement

Using the laser illumination method described above to determine the height and curvature of the truncated ball bearing, the values shown in Figure 16 were measured. The photograph of the ball bearing from which the measurements were made are also shown in Figure 17. It can be seen that the measured curve is very close to the true curve and error in the maximum height of the truncated ball bearing is only 1.25%.

Having proven that structured light can provide an accurate measurement of a three dimensional surface, an attempt was made to use this technique with an actual weld pool. Unfortunately, the liquid metal pool is too smooth to provide adequate diffuse reflection, and the image on the pool surface is not intense enough to be seen through the intense arc light. In spite of the successful application of structured light on the ball bearing surface, the technique is not applicable to arc welding.

B. Signal Analysis of Voltage Noise Welding Arcs

A paper on this topic is included in Appendix C.

C. Ultrasonic Measurement of Weld Pool Shape

Prof. D. Hardt and J. Katz

The improvement of automatically produced welds depends upon the ability to acquire an indication of the weld quality in process. Currently most efforts have concentrated upon the measurement and control of the penetration of a fusion weld. For example, Nomura, et al. (4) have developed a technique for measuring thermal radiation from the back side of a weld with photo diodes. The radiation is related to weld penetration and has been used as a feedback variable to modulate welding current. Researchers at the University of California at Berkeley have been considering a technique in which the top side weld bead width is measured and used as an indication of penetration. In either approach difficulties are encountered because the measured quantity is not unequivocably related to penetration.

As an alternative to these techniques, we have been investigating an ultrasonic pulse-echo technique for measuring weld penetration. Ultrasonic testing has been used effectively as a non-destructive evaluation technique of locating defects below the surface of various materials. It has become a standard technique for locating cracks, lack of fusion, porosity, and other defects in fusion welds. Ultrasonic depends on the material properties of the medium in which it travels. As these properties change, for example, and because a defect exists, partial reflections of ultrasound occur that can be detected by an ultrasound transducer. If the speed of propagation of the medium is known and the time required for ultrasound to travel between a transducer and some reflector is measured the position of that reflector can be determined.

Many non-destructive testing problems require knowledge of defect size and/or shape as well as the location of a defect. Several researchers have been

studying ultrasonic techniques of determining the size and shape of defects in materials. These techniques generally involve some deciphering of the characteristics of ultrasonic reflections from idealized defects like spheres, cylinders, and disks. These studies include both tie domain (5) and frequency domain (6) approaches and include techniques that determine size from a single reflection (7) or by observing the scattered intensity at several different locations (8,9). The results of these studies indicate that ultrasonic reflections from a given "target" are a function of both size and shape of the reflector/defect. If the essential features of ultrasonic reflections from known surfaces can be characterized, it should be possible to develop a means of measuring reflector dimensions from ultrasound traces. Sachse (7) has done this for the case of a fluid filled cylindrical inclusion in an aluminum block which Thompson and Thompson (10) have performed studies using a frequency domain scattering technique for identifying a more general target. In yet another approach, Rose (11) has used computer pattern recognition techniques to identify certain defects in welded steel plate.

The case of weld pool shape measurement presents a somewhat different physical situation. A molten weld pool should constitute a change in material properties that will result in the reflection of ultrasound. The manner in which ultrasound is reflected by the pool will be a function of the size and shape of the pool and the material properties of the weldment. A particular ultrasonic weld puddle measurement method that we have been investigating consists of one or more angle beam transducers that view the molten weld pool while tracking torch motion at all times. Figure 18 depicts one concept for such a measurement system. The transducer(s) reflect ultrasound from the molten weld pool, and their traces are interpreted to evaluate the pool shape and dimensions.

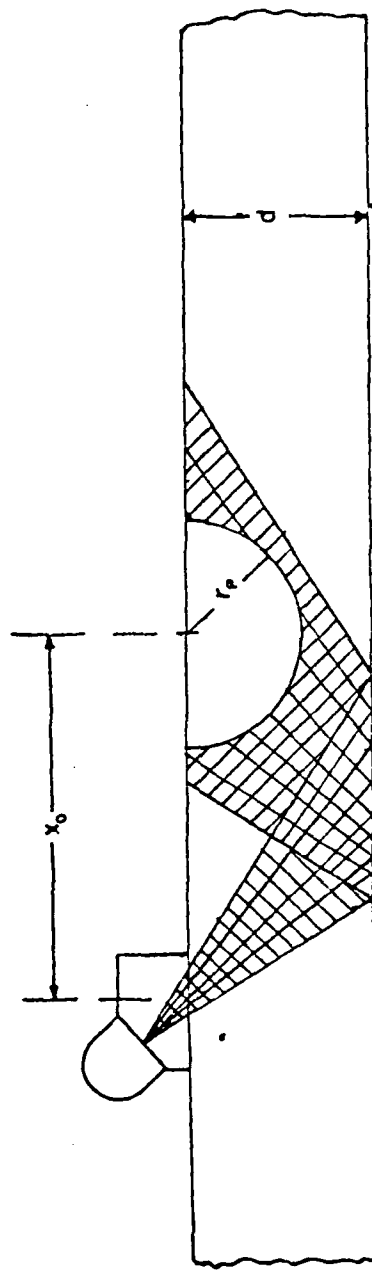


Figure 18: Weld pool in plate illuminated by angle beam ultrasound transducer

There are several justifications for the use of this particular configuration, and they are listed below:

1. The transducers can be positioned so that they are on the same side of the weldment as the welding torch.
2. The plate acts as a wave guide so that the only reflections that return to the transducer are from the joint or the weld pool.
3. An angle beam transducer produces shear waves, and since a liquid of low velocity cannot support the shear waves, the molten weld puddle should reflect all shear waves incident upon it.

There are however several areas of research that must precede the development of an ultrasonic pool measurement system. The bulk of these are the result of the large temperature gradients that exist within a weldment. The propagation speed of ultrasound is a function of the temperature of the medium. In general the speed drops as the temperature of the medium increases. This will result in an ultrasound velocity that varies with position (so called dispersion). Dispersion can cause shifting of the path followed by an ultrasound pulse and may make it difficult to "see" reflections from the molten/solid interface. High temperatures also cause an increase in attenuation (damping) of the medium. When the attenuation increases, larger amplitude ultrasound pulses must be applied in order to receive a measurable signal. In the heat affected zone of the weld, a solid phase transition can also cause reflections (12). If the magnitude of this reflection is large, it may not be possible to "see" the molten weld puddle. This would limit the ultrasonic technique to being a means of measuring the dimensions of the heat affected zone, however, if the magnitude of the reflection is small, it may be possible to locate both the heat affected zone and the molten weld pool. This would

present the opportunity for independent control of the HAZ and the penetration.

Ultrasound transducers must be mechanically coupled to the specimen they are used to examine and this can be done by using fluid contact between the transducer and the specimen to fill the asperities between the two or by physically compressing the transducer against the specimen. We have considered three coupling techniques for weld preparation measurement applications.

1. the transducer is dragged along the weldment surface and liquid couplant is continuously piped along the transducer path,
2. a fluid filled wheel transducer (commercially) available is used to provide contact between the transducer and the weldment,
3. a mechanism is used to compress the transducer against the weldment, take a measurement, and then step the transducer ahead to a new location, thereby giving a stepwise, static location measurement.

The development of an ultrasonic penetration measurement system requires that all of the above issues be addressed.

In order to evaluate the potential for measuring weld puddle dimensions, a series of semi-cylinders of size from .631 mm (.025 in) to 3.175 mm (.125 in) deep were machined into the top of mild steel plate. An angle beam transducer and a Krautkramer USM-2 ultrasonic flaw detector was then used to obtain reflections from the semi-cylinders. The results of these experiments indicate that the reflections from such a surface vary in a repeatable manner as the size of the reflector is varied. A simple geometric optics model of the ultrasonic reflections from a cylindrical reflector is being constructed to attempt to predict the ultrasonic traces that result. It will not completely describe the ultrasonic traces but will be an adequate predictor for size determination.

In order to obtain reflections from a molten weld pool, the simplest possible weld sample geometry was constructed. This is a 6 in long, 5/8 in

diameter steel rod. The rod was turned so that a longitudinal wave ultrasound transducer could be clamped on one end, and a weld pool could be melted at the other end. In this way, the ultrasound transducer was looking directly at the weld pool (see Figure 19). A series of welding tests were performed using this configuration. Then a series of hemispheres of increasing size were milled into the end of the rod. The following general observations were made:

1. As the rod heated up, the attenuation increased rapidly. The maximum phase energy and signal amplification of the USM-2 were required to obtain a return signal.
2. The time of travel between the rod ends increased as the rod temperature increased, indicating (as expected) a sound velocity decrease.
3. The location and shape of the ultrasonic reflection shifted as the weld pool size changed.
4. The shape of reflections from a rod with a weld pool at the end is qualitatively similar to the shape of the reflection from a milled hemisphere at the rod end.

The results of these preliminary experiments indicate that ultrasound reflections from the molten weld pool/heat affected zone region can be observed and do change as pool size changes. The experiments performed with machined surfaces indicate that ultrasound reflections vary repeatedly with the size of the surface. Further experimentation and analytical developments are clearly warranted to provide a quantitative statement concerning the capabilities of ultrasonic weld pool measurement, and to address questions of applications to active pool size control.

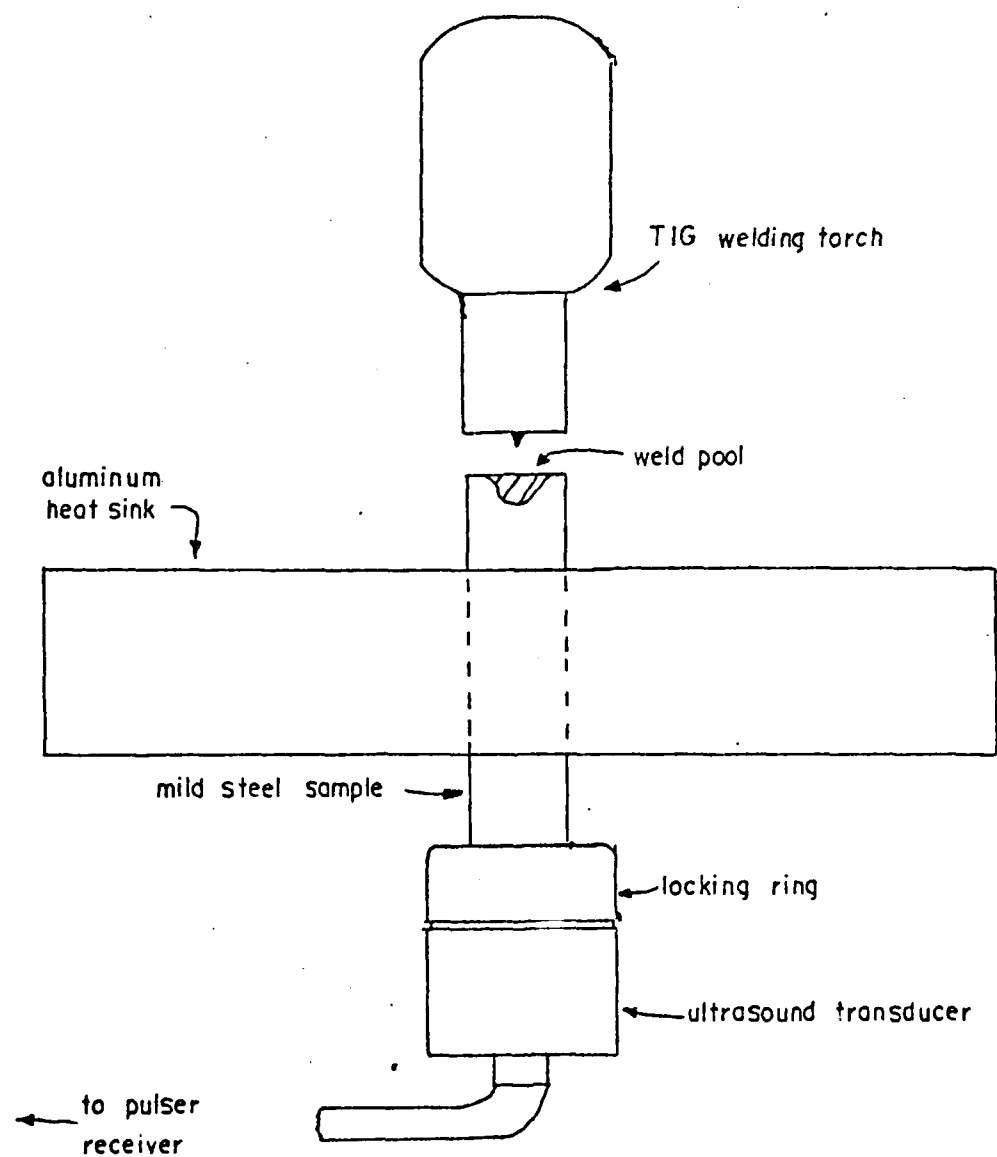


Figure 19: Configuration for detecting ultrasonic reflections from a weld pool

5. ADDITIONAL RESEARCH TOPICS

Two additional papers have been prepared based upon studies conducted under this contract. These are included in Appendices D and E. The studies reported in these two papers have been completed.

REFERENCES

1. P. R. Bevington, Data Reduction and Error Analysis for the Physical Sciences, McGraw-Hill, New York, 1969.
2. D. Ya. Svet, High Temp.-High Pres., 8, 1976, p. 493-498.
3. Savitskii, M. M. and Leskov, G. I., "The Effects of Electrically-Negative Elements on the Penetrating Power of an Arc with a Mechanism of the Tungsten Electrode," Automat. Weld., Sept. 1980, 33, (9), 11-16.
4. Nomura, H., et al., "Arc Light Intensity Controls Current in SA Welding Systems," Welding and Metal Fabrication, Sept. 1960, pp. 457-463.
5. Pao, Y. H. and Wolfgang Sachse, "Interpretation of Time Records and Power Spectra of Scattered Ultrasonic Pulses in Solids," J. of the Acoust. Soc. Am., 56(5), Nov. 1974, pp. 1478-1486.
6. Gericke, D. R. "Determination of the Geometry of Hidden Defects by Ultrasonic Pulse Analysis Testing," J. Acoust. Soc. Am., 35, 1963, p. 364.
7. Sachse, Wolfgang, "Determination of the Size and Mechanical Properties of a Cylindrical Fluid Inclusion in an Elastic Solid," Material Evaluation, 33, April 1975, pp. 81-88.
8. Tittman, B. R., et al., "Scattering of Longitudinal Waves Incident on a Spherical Cavity in a Solid," J. Acoust. Soc. Am., 63(1), 1978, p. 68.
9. White, R. M., "Elastic Wave Scattering at a Cylindrical Discontinuity in a Solid," J. Acoust. Soc. Am., 30(8), August 1958, pp. 771-785.
10. Thompson, D. O. and R. B. Thompson, "Quantitative Ultrasonics," Phil. Trans. R. Soc. London, 292, 1979, pp. 233-250.
11. Rose, J. E., et al., "Flaw Classification in Welded Plates Using a Microprocessor Controlled Flaw Detector," NDT International, 13(4), August 1980, pp. 159-164.
12. Papakakis, E. P., et al., "Ultrasonic Attenuation and Velocity in Hot Specimens by the Momentary Contact Method with Pressure Coupling and Some Results on Steel to 1200°C," J. Acoust. Soc. Am., 52(3), 1972, pp. 850-857.

APPENDIX A

Presented at a Conference on Trends in Welding Research
New Orleans, LA, November 1981

SELECTIVE EVAPORATION OF METALS FROM WELD POOLS

A. Block-Bolten and T. W. Eagar
Materials Processing Center
Massachusetts Institute of Technology
Cambridge, Massachusetts 02139

ABSTRACT

An analysis of metal vaporization from arc weld pools based upon thermodynamic data and the kinetic theory of gases is presented. It is concluded that Mn and Fe are the dominant vapors when welding steel and stainless steel, and that the maximum weld pool surface temperature of such steels is approximately 2500°C with an average temperature of 2050°C.

INTRODUCTION

It has long been recognized that metal vaporizes from the pool of a welding arc, yet it is commonly assumed that the dominant specie in the weld pool is also the dominant specie in the metal vapor. This is not true in general because the more volatile components will be concentrated more heavily in the gaseous phase. This fact has been recognized in recent studies of fume formation,⁽¹⁾ of electrode contamination⁽²⁾, of arc physics^(3,4) and of weld pool shape⁽⁵⁾, yet none of these investigators have attempted to quantify the composition expected in the gas phase as a function of the composition in the liquid phase. Such an analysis can reveal significant information concerning the effect of changes in base metal composition on the behavior of welding arcs. In addition, it will be shown that evaporative cooling of the surface of the liquid weld pool places an upper bound on the temperature of the weld pool which is much lower than previously thought. The process of selective evaporation may also be important in higher energy

density processes such as rapid surface heat treatment involving melting and laser or electron beam welding

APPROACH

For a pure metal, A, the free energy of evaporation, ΔG_e° is given by

$$\Delta G_e^\circ = -RT \ln p_A^\circ \quad (1)$$

where R is the gas constant

T is the absolute temperature, and

p_A° is the equilibrium vapor pressure of pure A at temperature T.

If A is not pure but is in solution, the free energy change on evaporation is given by $\Delta G_e^\circ - \Delta G$ where ΔG is the partial molar free energy of mixing of A for the reaction.

$$M_{\text{solution}} \neq M_{\text{gas}}$$

It is known that

$$\Delta \bar{G} = -RT \ln \bar{p}_A \quad (2)$$

where \bar{p}_A is the partial pressure of A above the alloy, so that the total free energy change on evaporation of metal A from an alloy is given by equation (1) minus equation (2).

$$\Delta G_{\text{tot}}^\circ = RT \ln \frac{\bar{p}_A}{p_A^\circ} \quad (3)$$

The term $\frac{\bar{p}_A}{p_A^\circ}$ is the thermodynamic activity, α_A of specie A in the alloy, or we may write

$$\ln \bar{p}_A = \ln p_A^\circ + \ln \alpha_A \quad (4)$$

Hence, if the composition of the melt is known, the activity can be calculated⁽⁶⁾; and using tabulated data for vapor pressures of pure metals,⁽⁷⁾ the equilibrium partial pressure of any specie in the gas phase as a function of temperature is readily calculated. Selections of such data for the

systems Fe-Mn, Fe-Cr, Fe-Ni and Fe-Al are given in Figures 1 through 4. It will be noted that low concentrations of metal A will give highly negative values of $\log \bar{Q}_A$ thus small changes in concentration of a minor element, A, in the melt may produce dramatic changes in the concentration of A in the gas phase expressed by p_A .

The vapor pressures calculated for Figures 1-4 are strictly valid only for binary melts; however, in the absence of strong interaction effects between atoms, the data presented in these figures can be used to approximate a more complex alloy. Figure 5 is a plot of the partial pressure of several components in Fe alloys, at constant temperature plotted versus the composition of the melt. It will be noted that iron being the solvent, has been plotted in reverse. From this graph, it can be seen that iron behaves identically for Mn, Cr and Ni. Only aluminum exhibits a strong effect on the pressure of iron, and this occurs only at higher concentrations than normally encountered in steels. Hence, it is possible to estimate the vapor pressures in a complex alloy such as 304 stainless steel as shown in Figure 6. By using the overlapping grid points which are placed on Figures 1-4, it is possible to construct such a plot for any Fe-Mn-Cr-Ni-Al alloy. A similar set of graphs can be constructed for other alloy systems as well.

It will be noted that the slopes of the Fe-Mn plots are significantly different from the Fe-Cr or Fe-Ni plots. These slopes represent the heat of evaporation minus the heat of mixing of the metal in the alloy, divided by the gas constant. The differences in these quantities for Mn and Fe may provide information about the temperature of the process, as will be discussed subsequently.

Given the equilibrium pressure of a species over a melt, Dushman⁽⁸⁾ has derived a method for calculation of the vaporization rate based upon the kinetic theory of gases. Combining this vaporization rate with the heat lost by vaporization, one can calculate the vaporization power as described by Cobine and Burger⁽⁹⁾. If W is the rate of evaporation in $g \cdot cm^{-2} \cdot sec^{-1}$, then evaporation power in watts $\cdot cm^{-2}$ is given by

$$W(L_e - \bar{\Delta H})$$

where L_e is the heat of evaporation of the pure metal and $\bar{\Delta H}$ is the partial molar heat of mixing of the metal in the alloy.

The evaporation energy is obtained by multiplying the evaporation power by the time. Examples of this analysis for the Mn and Cr systems are given in Figures 7 and 8,

respectively. Values for Fe and Cu are shown on these figures for purposes of comparison.

Finally, the evaporation power as calculated in Figures 7 and 8, provides a method of describing the temperature on the weld pool surface. At higher input power levels, the surface will attain a higher temperature, however, the slopes of these curves are relatively steep so the maximum temperature is not found to vary widely for typical arc welding power densities. Nestor⁽¹⁰⁾ has shown that the maximum input power levels for arc welding are between 1000 and 10,000 watts cm^{-2} . These input power limits are shown on Figures 7 and 8; but there is more to be gleaned from this. Using Nestor's power distribution across the anode surface one can use the data of Figures 7 and 8 to calculate the maximum surface temperature across the weld pool. The results of this are shown in Figure 9. Nestor's heat input distributions, as well as an equivalent, cylindrical gaussian heat distribution of equivalent total power and peak power, have been used to calculate the maximum surface temperature across the weld pool.

DISCUSSION

Bennett and Mills⁽²⁾ and Heiple et al.⁽⁵⁾ have shown that differences in aluminum concentration in stainless steels on the order of several hundred parts per million can have a profound influence on the depth to width ratio of the resulting weld bead. Glickstein has shown that as little as 100 ppm Al in He shielding gas can drastically alter the properties of the welding plasma. From Figures 1 and 6 it may be seen that the small weld pool compositional changes described by Bennett and Mills could produce plasma compositional changes of the magnitude described by Glickstein; however, Figure 6 also shows that Al will not be the dominant metal vapor specie in the arc plasma. The calculations performed by Glickstein would not produce such dramatic changes in plasma properties if a ternary addition of a metal vapor, such as Mn, at 1000 times the Al concentration, were also added to the plasma gas. It would appear from these results that the effect of Al on stainless steel weld pool shape is more likely the result of changes within the weld pool, such as surface tension driven convection, rather than changes in the arc plasma. This conclusion is confirmed by the recent work of Heiple and Roper, as reported in this conference.⁽¹²⁾

Comparison of Figures 2, 3, 4 and 6 indicates that Mn vapor is the dominant metal vapor specie in the plasma of

stainless steel welds, but that Fe rather than Cr is the second most abundant specie. From this analysis it is concluded that the concentration of Cr vapor would be nearly an order of magnitude lower than the concentration of Mn vapor when welding most alloy steels. This result may be helpful in quantifying the spectrographic measurements of Shaw⁽³⁾ and Key⁽⁴⁾ while confirming the report of a nearly pure Mn halo formation around the tungsten welding electrode when welding high manganese stainless steels.⁽¹⁾ This halo has been observed to form within ten to fifteen minutes when welding other stainless steels as well.⁽¹³⁾ Spectrographic measurements in our laboratory have confirmed that the Mn/Cr ratio decreases considerably over a period of minutes when arc melting a Cr-Mn steel or stainless steel.

As noted previously, differences in the heats of evaporation and mixing for Fe and Mn cause a change in the relative concentration of these elements in the welding arc plasma as a function of temperature. The ratio of partial pressures is shown in Figure 10. It will be noted that the Mn/Fe plasma ratio is a very sharp function of both liquid metal composition and weld pool temperature. It is possible that this ratio could be used as a method of spectrographically monitoring the welding process.

From Figures 7 and 8, it can be seen that the surface temperature of the molten weld pool is a strong function of metal composition. In Fe-Cr alloys the surface temperature is controlled by iron vaporization for alloys of less than 30 to 40 percent Cr; however, in Fe-Mn alloys Mn vaporization will limit the weld pool temperature at concentrations greater than about 2 percent Mn. Below one percent Mn the dominant vapor in the arc will be Fe. Comparing this figure with Figure 9 at a peak power input of $6000 \text{ watts} \cdot \text{cm}^{-2}$ the maximum weld pool surface temperature in an iron dominated arc is barely more than 2500°C , whereas many investigators assume a peak temperature closer to the boiling point of Fe, i.e., 3000°C . If a weld were dominated by vaporization of Mn in a 0.5% Mn-Fe alloy, the 3000°C temperature would be appropriate, but in fact it is not because Fe will vaporize first, thereby cooling the weld pool to 2500°C . A drop in peak power input by a factor of three lowers the peak surface temperature by less than 200°C (cf. Figure 9).

It is interesting to note that the average value of a two dimensional cylindrical gaussian distribution is given by the value at which $r = \rho/\sqrt{2\rho}$. For the 2000 watt cm^{-2} peak power arc the average surface temperature is approximately 2050°C , which is not very different from the effective weld chemical reaction temperature found by Chai and Eagar.⁽¹⁴⁾

It will be noted from Figures 7 and 8 that the surface

temperatures in high energy density processes such as laser and electron beam welding at 10^6 watts \cdot cm $^{-2}$, will lie between 4000 and 5000°C. It will further be noted that the actual surface temperatures for these processes will be strong functions of the composition of the alloy. This has been confirmed by experiment.⁽¹⁵⁾

CONCLUSIONS

An analysis of metal vaporization from alloy weld pools has been performed by use of thermodynamic data and the kinetic theory of gases. The results indicate the following:

1. Mn and Fe are the dominant vapors when welding steels and stainless steels.
2. Although Cr vapor is present, it is a minor specie of the metal vapor.
3. It is unlikely that the effect of Al vapor on plasma properties can explain the differences in weld pool shape observed by other investigators, even though small changes in the base metal concentration of Al may produce large changes in the concentration of Al in the plasma.
4. The power lost by metal vaporization places an upper limit on the temperature of steel arc weld pools of approximately 2500°C.

These concepts may readily be extended to alternate alloy systems for which thermodynamic activity data is available.

ACKNOWLEDGEMENTS

The authors wish to thank the Office of Naval Research for sponsoring this work on contract N00014-80-C-0384. Helpful discussions with Professor D. R. Sadoway are appreciated.

REFERENCES

1. R. F. Heile and D. C. Hill, "Particulate Fume Generation in Arc Welding Processes," Weld. J. 54(7), 1975, p.201-s.
2. W. S. Bennett and G. S. Mills, "GTA Weldability Studies

on High Manganese Stainless Steel," Weld J., 53(12), 1974,
p.549-s.

3. C. B. Shaw, Jr. "Diagnostic Studies of the GTAW Arc,"
Weld J., 54(2), p.33-s.

4. J. F. Key, M. E. McIlwain and L. Isaacson, "A Plasma
Diagnostics Approach to Welding Heat Source/Molten Pool
Interaction," Proc. Conf. on Arc Physics, Edinburg Scotland,
September, 1980.

5. C. R. Heiple, R. J. Cluley and R. D. Dixon, "Effect of
Aluminum on GTA Weld Geometries in Stainless Steel," in Phys.
Metal. of Metal Joining, R. Kossowsky, Ed., TMS-AIME,
Warrendale, PA, 1980, p.160.

6. R. Hultgren, P. D. Desai, D. T. Hawkins, M. Gleiser, K.
K. Kelley, Selected Properties of Binary Alloys, ASM, Metals
Park Ohio, 1973.

7. I. Barin and O. Knacke, Vol. I, Thermochemical Properties
of Inorganic Substances, Springer Verlag, Berlin, 1973, and
I. Barin, O. Knacke, O. Kubaschewski, Vol. II (supplement),
Thermochemical Properties of Inorganic Substances, Springer
Verlag, Berlin, 1977.

8. S. Dushman (revised by L. R. Koller), Scientific
Foundations of Vacuum Technique, J. M. Laferty, Ed., 2nd
edition, Chapter 10: "Vapor Pressures and Rates of
Evaporation," pp.691-737, (also pp.15-21 of Chapter 1; John
Wiley, New York, 1962.)

9. J. D. Cobine and E. E. Burger, "Analysis of Electrode
Phenomena in the High-Current Arc," J. Appl. Phys. 26(7)
pp.895-900, 1955.

10. O. H. Nestor, "Heat Intensity and Current Density
Distribution at the Anode of High Current, Inert Gas Arcs,"
J. Appl. Phys. 33(5), pp.1638-1648. 1962.

11. S. S. Glickstein, Proceedings of the International
Conference on Arc Physics and Weld Pool Behavior, London, May
8-10, 1979, W. Lucas, Ed., The Welding Institute, Cambridge,
England, 1979.

12. C. R. Heiple and J. R. Roper, "Minor Element Effects on
GTA Fusion Zone Geometry," Proceedings of this Conference.

13. A. Block-Bolten, "unpublished research, Massachusetts Institute of Technology, Cambridge, MA, 1981.
14. C. S. Chai and T. W. Fagar, "Slag-Metal Equilibrium During Submerged Arc Welding," Met. Trans., 12B, 1981, p.539.
15. D. A. Schauer, W. H. Geidt and S. M. Shintaku, "Electron Beam Welding Cavity Temperature Distributions in Pure Metals and Alloys," Yale J., 57(5), 1978, p.127-s.

APPENDIX

The normal distribution curve of power density is given by

$$y = Ce^{-1/2(r/\rho)^2}$$

where y is in watt \cdot cm $^{-2}$

C is the peak power density in watt \cdot cm $^{-2}$

and r/ρ is the dimensionless radial distance.

The two dimensional gaussian distribution forms a three dimensional volume which represents the total power of the arc. This volume is given by

"Volume" V in watts

$$V = C \int_0^{2\pi} d\rho \int_0^{\infty} r \cdot dr \cdot e^{-r^2/2\rho^2}$$

Using the transformation

$$x = r/\sqrt{2\rho} \text{ and } dx = dt/\rho\sqrt{2}$$

$$V = 2\pi C \rho^2 \int_0^{\infty} x e^{-x^2} \cdot dx$$

$$V = 2\pi \rho^2 C, \text{ or}$$

$$\rho = \sqrt{V/2\pi C}$$

Using Nestor's data, where $C = 6120$ for the Cathode Spot Mode and $C=2180$ for Normal Mode, the following data are obtained:

$$\rho_{CSM} = 0.277$$

$$\rho_{NM} = 0.452$$

FIGURE CAPTIONS

Fig. 1 Vapor pressures over the Fe-Mn system. Note grid points at $\log p = -3.0$ and -5.0 to overlap with Figs. 2, 3 and 4.

Fig. 2 Vapor pressures over the Fe-Cr system. Note grid points to overlap with Figs. 1, 3 and 4.

Fig. 3 Vapor pressures over the Fe-Ni system. Note grid points to overlap with Figs. 1, 2 and 4.

Fig. 4 Vapor pressures over the Fe-Al system. Note grid points at $\log p = -3.0$ and -5.0 to overlap with Figs. 1, 2 and 3.

Fig. 5 Partial pressure isotherms plotted against log of solute concentration in wt%. Fe as solvent is plotted in reverse.

Fig. 6 Composite diagram of vapor pressures for the 304 stainless steel, based on four overlapping binary systems.

Fig. 7 Manganese isopleths plotted against log of pressure, log of evaporation rate, log of evaporation power (which also represents log of evaporation energy per second). Iron and Cu evaporation curves are plotted for comparison and apply only to the pressure scale. Input power limits used by Nestor are plotted, as well as the black body radiation curve. The diagram is valid only in the manganese m.p.-b.p. range.

Fig. 8 Chromium isopleths plotted against log of pressure, log of evaporation rate, log of evaporation power (which also represents log of evaporation energy per second). Iron and

Cu evaporation curves are plotted for comparison and apply only to the pressure scale. Input power limits used by Nestor are plotted, as well as the black body radiation curve. The diagram is valid only in the chromium m.p.-b.p. range.

Fig. 9 a, b Maximum surface temperatures across the weld pool for Cathode Spot Mode and Normal Mode, respectively. Curves represented are those for 0.5% Mn in Fe, 2.0% Mn in Fe and pure iron. For comparison, a temperature curve based on normal distribution of power is plotted. This diagram is constructed on the basis on Fig. 1 and on Nestor's power distribution data.⁽¹⁰⁾.

Fig. 10 Mn/Fe partial pressure ratio as temperature probe. Sharp dependence of the Mn/Fe ratio on the local liquid alloy concentration and on temperature may serve as a monitoring device for the welding process.

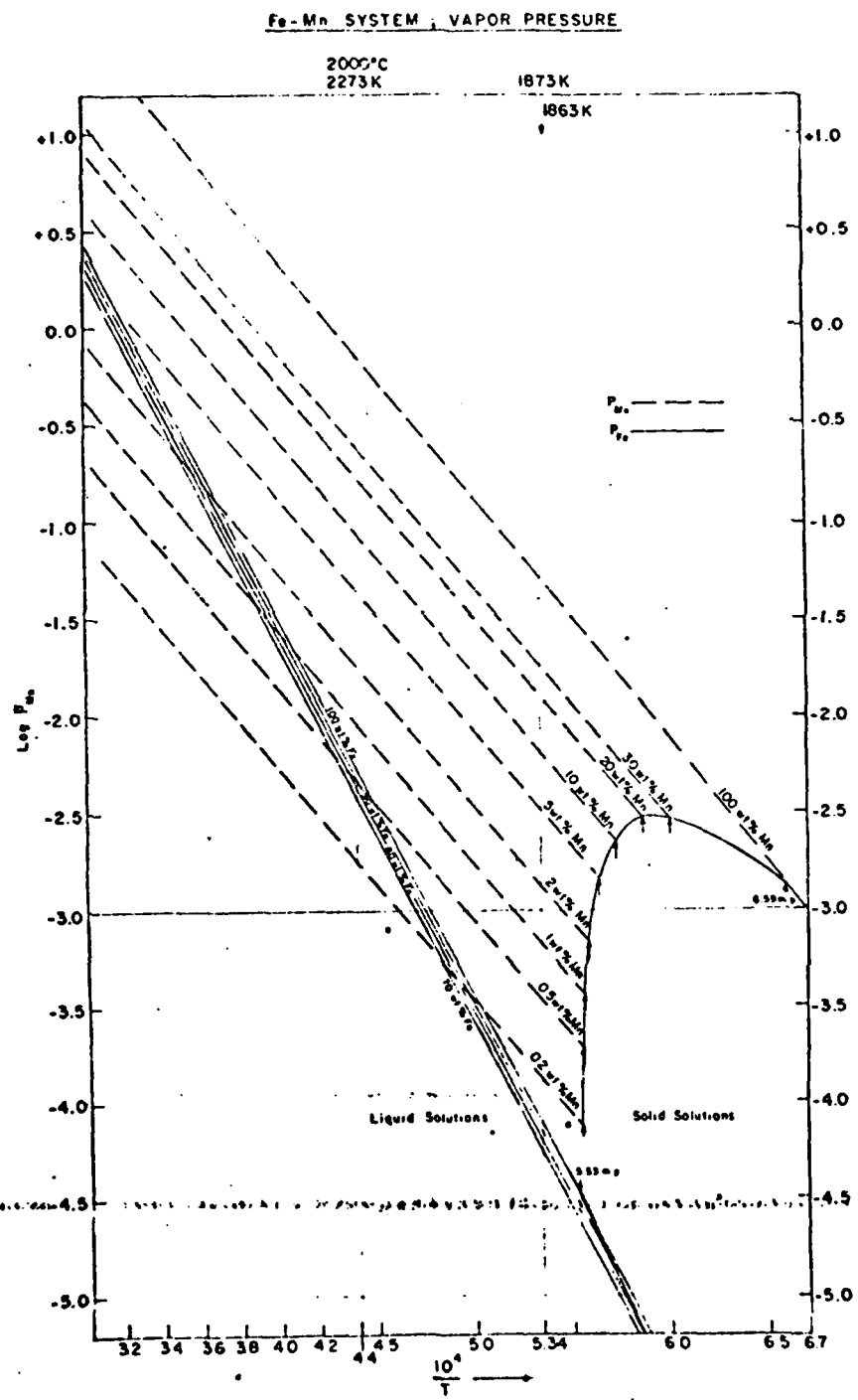


Figure 1

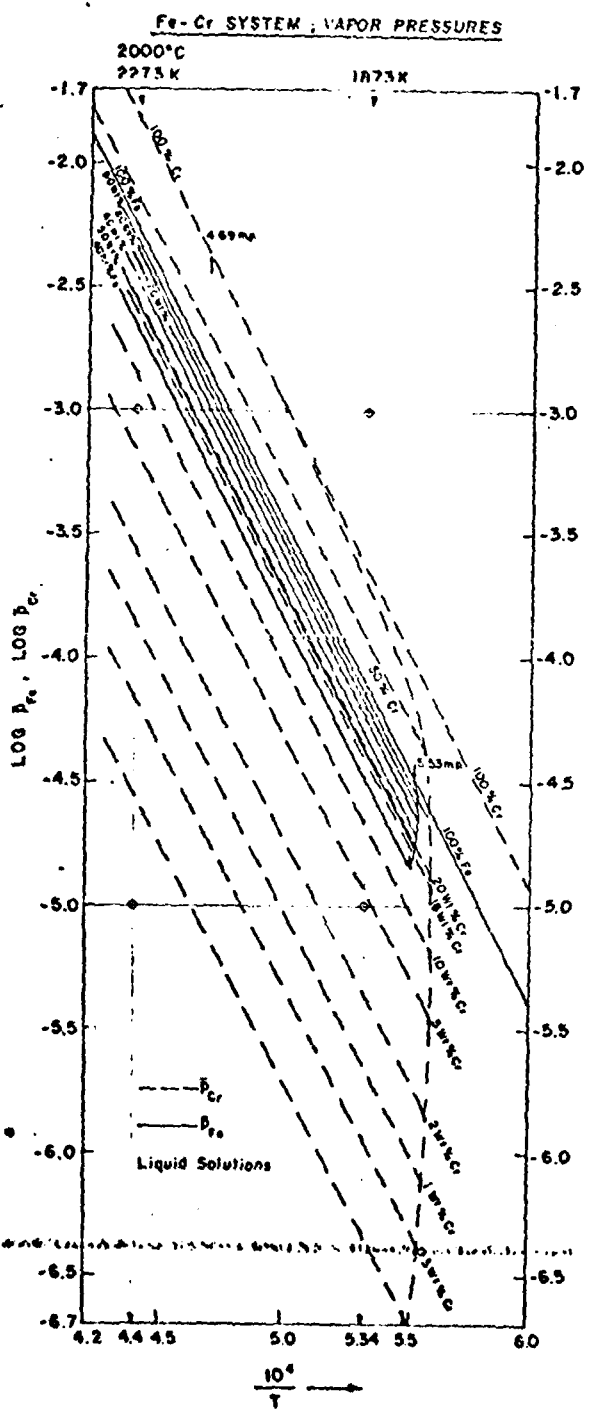


Figure 2

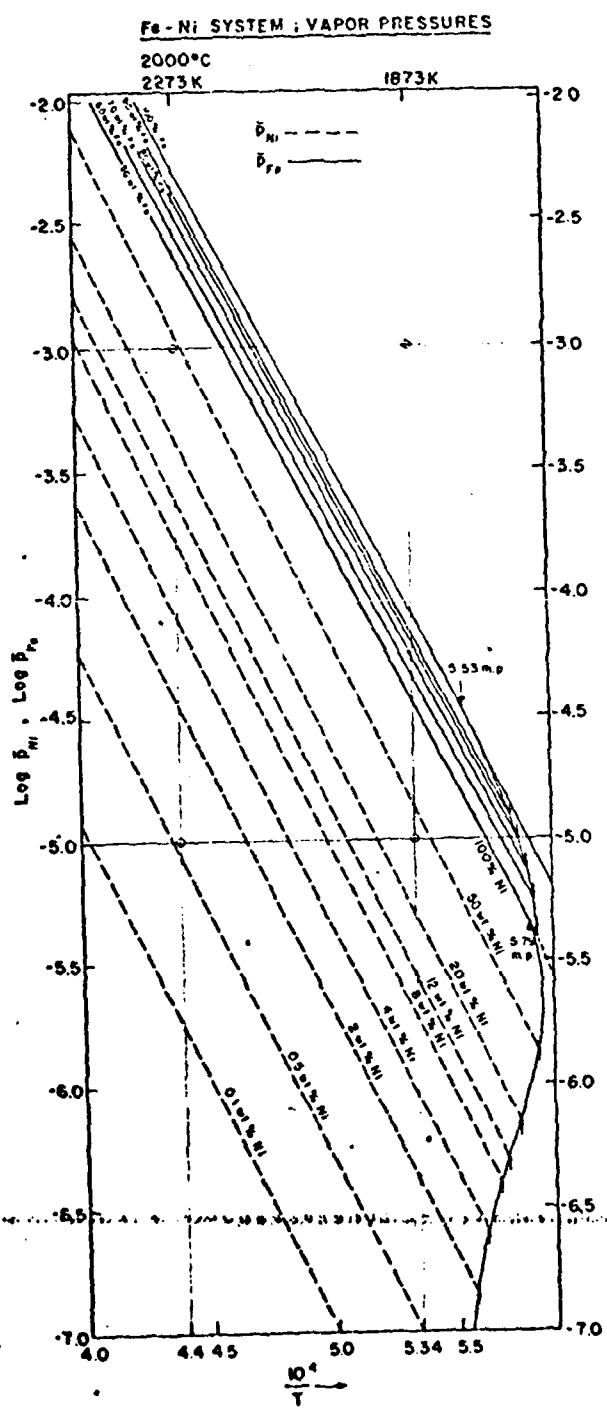


Figure 3

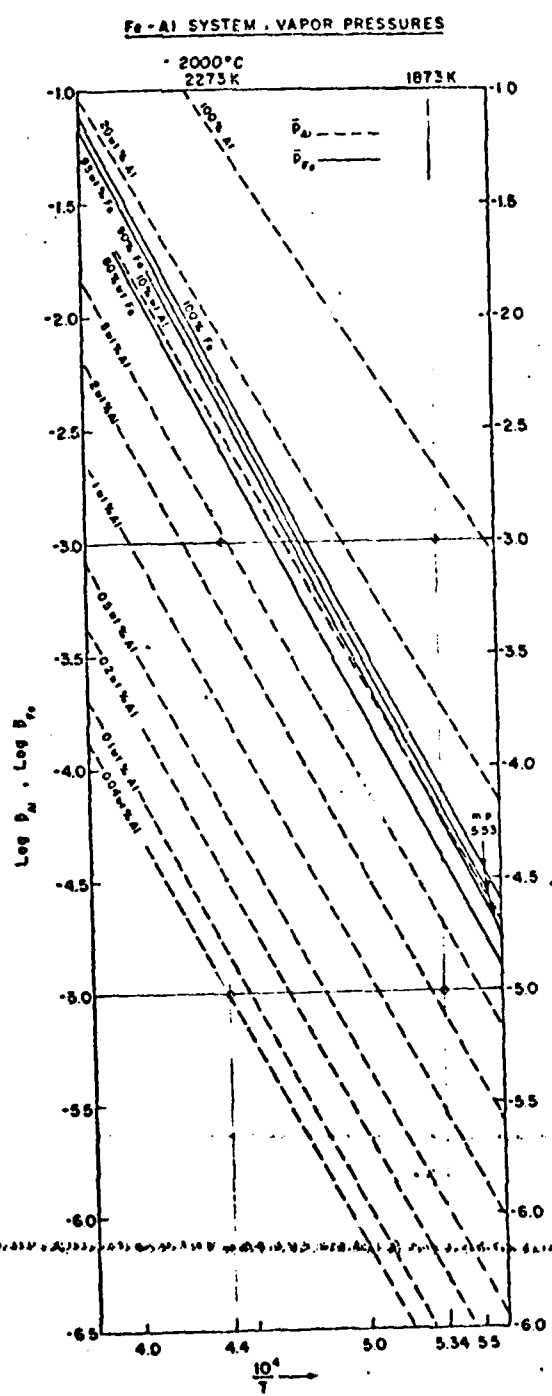


Figure 4

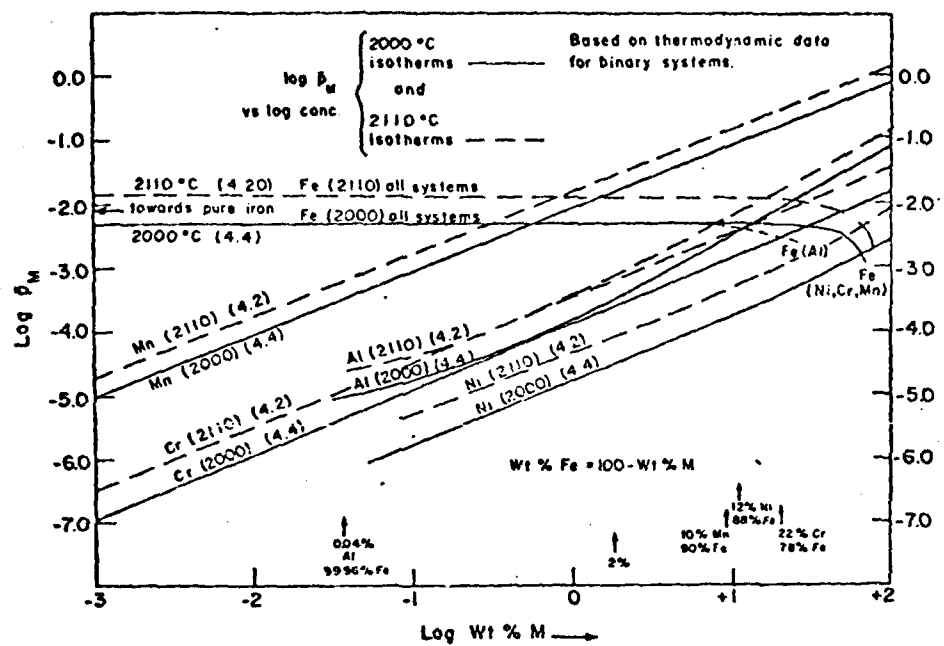


Figure 5

STAINLESS STEEL 304; VAPOR PRESSURES
I-ST. APPROXIMATION

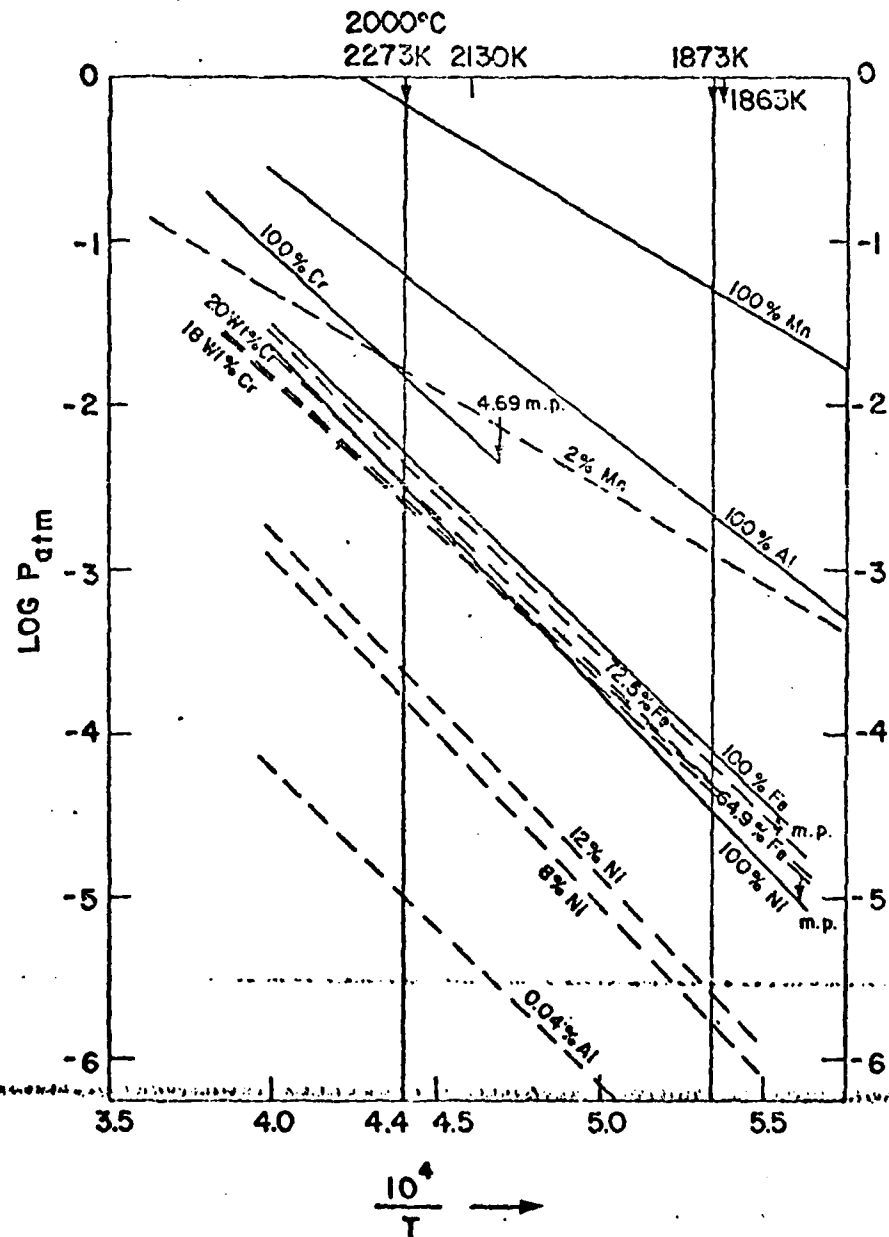


Figure 6

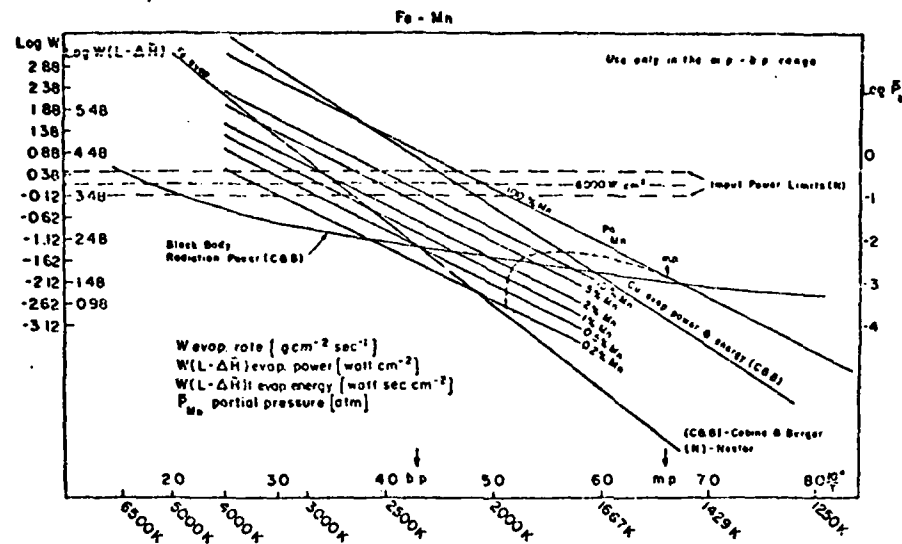


Figure 7

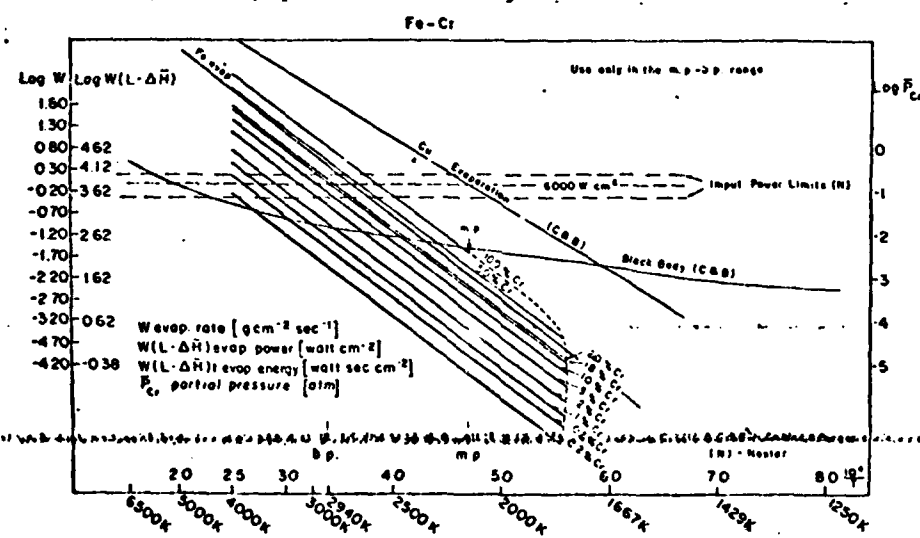


Figure 8

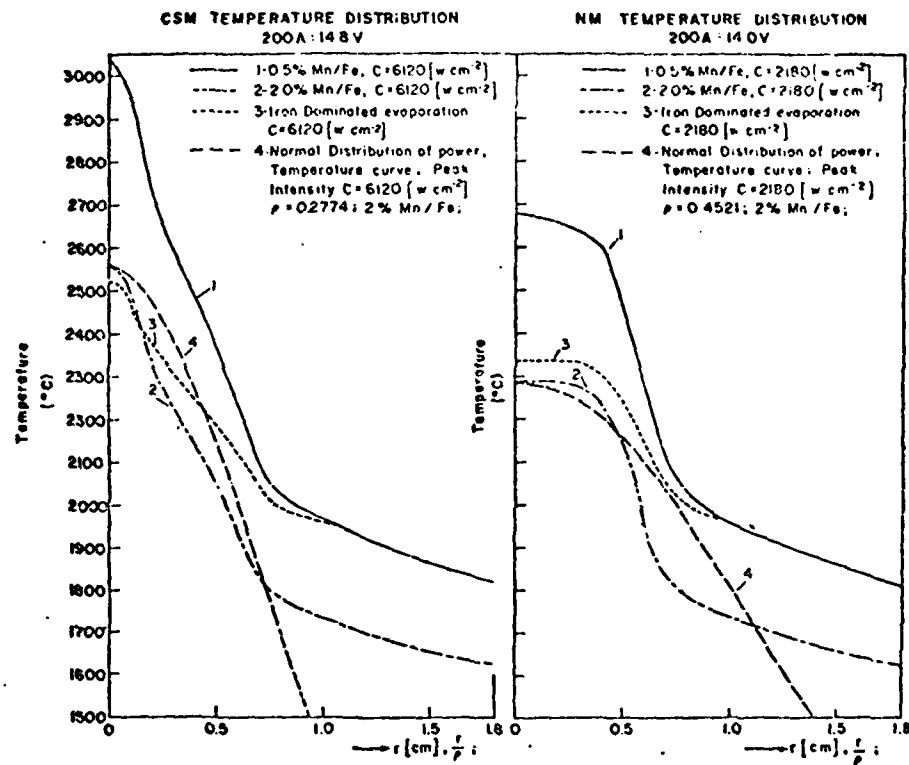


Figure 9a and b

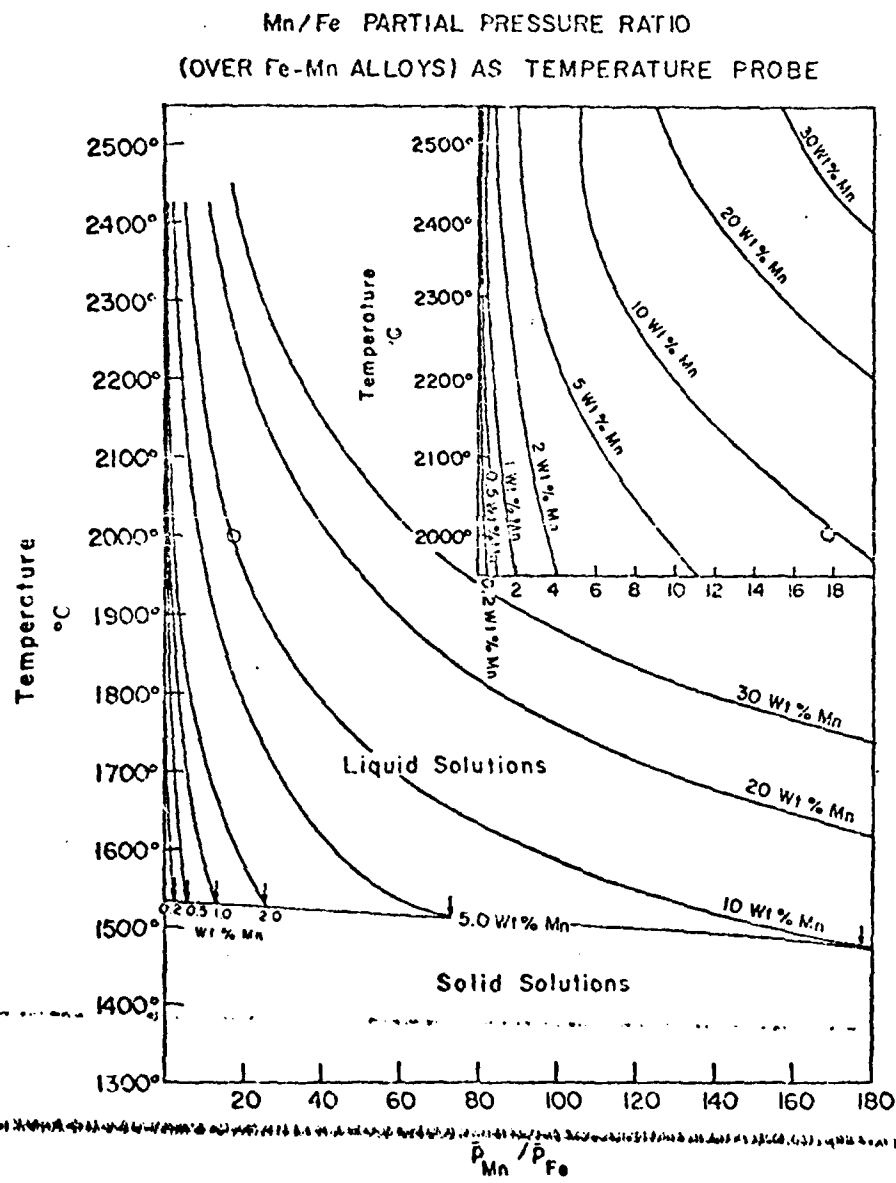


Figure 10

Presented at IEEE-IAS 1981 Annual Meeting, Philadelphia, PA.,
October 5-9, 1981

**A FAST RESPONSE TRANSISTOR CURRENT REGULATOR
FOR WELDING RESEARCH**

D. Galler, Member IEEE
Alexander Kusko, Inc.
Needham Heights, MA.

A. Kusko, Fellow IEEE
Alexander Kusko, Inc.
Needham Heights, MA.

J. Converti
Massachusetts Institute of Technology
Cambridge, MA.

ABSTRACT

The paper describes the design, construction and performance of a 300 A dc transistor current regulator for welding research. The current regulator responds to an external low-voltage reference signal and is designed to operate with a large signal bandwidth of 20 kHz. The purpose of the current regulator is to provide fast risetime high-current waveforms to use as an effective research tool and as a means of providing significant improvements in commercial welding quality as well. Preliminary results of Gas-Tungsten-Arc (GTA) and Gas-Metal-Arc (GMA) welding research projects using the current regulator are presented. The application of transistor regulated power supplies to commercial welding is discussed.

I. INTRODUCTION

The current regulator described in this paper was developed to provide an adjustable current source with fast response for welding research, with the following features:

- Input voltage of 60 V dc and an output voltage of at least 25 V dc for arc loads.
- Output current rated at 300 A dc continuous, adjustable over the range 0-300 A by means of a low voltage reference signal.
- Arc current response to a step change in the reference signal to have a settling time of 100 μ s or less for 100 A step changes. The small signal bandwidth from the reference input to be at least 20 kHz.
- Accuracy of the output current to be $\pm 1\%$ of 300 A as set by the reference signal.
- Output current to be maintained to $\pm 1\%$ of 300 A for 20% input or 100% load voltage disturbances.

To meet these requirements three methods of current control were considered:

- phase controlled three-phase thyristor rectifier,
- transistor or thyristor chopper,
- series-pass transistor regulator.

The phase controlled thyristor rectifier is commonly used in commercial welding power supplies. The output voltage of the power supply is controlled by the time or angle in each cycle at which the thyristors are fired. Advancing the firing angle increases the average output voltage; retarding the firing angle decreases the average output voltage. The output voltage has considerable ripple at 360 Hz. The firing angle control can be used to regulate the output voltage or current, but because of the thyristor firing periodicity the control bandwidth is limited to about 100 Hz. The ripple can be reduced by filtering with corresponding reductions in the bandwidth.

Transistor choppers are used in switching-type power supplies for electronic equipment, as well as in dc motor drives for transportation. The output voltage is controlled by the duration of the on and off times of the transistor or thyristor switch. A common scheme uses a fixed on/off cycle time and varies the "on" duration of the switch to control the voltage. Switching frequencies of 20 kHz to 40 kHz are common in transistor power supplies up to about 5 kW. Thyristor choppers for dc traction motors run at 200 Hz to 400 Hz with ratings up to about 1000 kW. The output voltage or current waveform is usually filtered to less than 1% ripple. For a 20 kHz switching frequency, the control bandwidth is about 5 kHz, which is further reduced to about 1 kHz by the filter. The chopper cannot provide the low ripple level and fast response required for this application.

In the linear series-pass transistor power supply, the transistors are used as adjustable resistors to absorb the difference between input and output. The output voltage or current is controlled by varying the base current applied to the pass transistor. An amplifier compares and processes the error between the measured value of current (in this case) and the reference value to provide the base current. The power supply output has essentially no ripple. The bandwidth is limited only by the response speed of the pass transistor. Because of their high power dissipation and consequent low efficiency, linear power supplies of this type are typically used only in applications below a few hundred watts. Bandwidths as high as 100 kHz can be achieved depending on the type of transistor and design of the amplifier circuits. Accuracy and stability as high as 0.01% can be attained; accuracy to 0.1% is typical in small commercial power supplies. We have selected the linear series-pass transistor regulator for this application.

This paper describes the design, testing and application of a 300 A linear series-pass current regulator, which is presently being used for research on arc welding at MIT. The current regulator itself was designed and constructed as a separate unit to be used in conjunction with a conventional transformer-rectifier welding power supply to provide the dc input voltage. The current regulator has demonstrated 200 A step changes in current into an arc load, with settling times less than 100 μ s.

II. DESIGN

Before starting the design, a complete specification of the current regulator was developed with the research staff of the Energy and Chemical Dynamics Laboratory at MIT to meet their requirements for a wide range of welding research tasks. The particular laboratory environment determined the best construction methods as well as the features to properly interface the regulator with existing equipment. The specification is shown in Fig. 1.

Electrical	
Input	60 V dc, 0.300 A dc
Continuous Output Rating	300 A dc, 25 V dc (10.5 kW)
Regulation	$\pm 1\%$, line and load
Reference Signal	0-10 V dc full scale
Step Response	
• Rise Time	50 μ s
• Overshoot	10%
Mechanical	
Cabinet Dimensions	13" x 36" x 24"
Cooling Requirements	
• Forced Air	100 CFM
• Open-Cycle Water	5 GPM, 25 psig max.
Protection	
Overcurrent	350 A dc fuse
Overtemperature	
• Thermal Sensing	65°C Thermal Switches
• Coolant Flow Sensing	5 psi Pressure Switch

Fig. 1. Specifications for the Current Regulator.

Functional Design

The functional diagram shown in Fig. 2 identifies the key design areas:

- the cooling system,
- the power output circuit,
- the current control circuit,
- the protection and sequencing circuit.

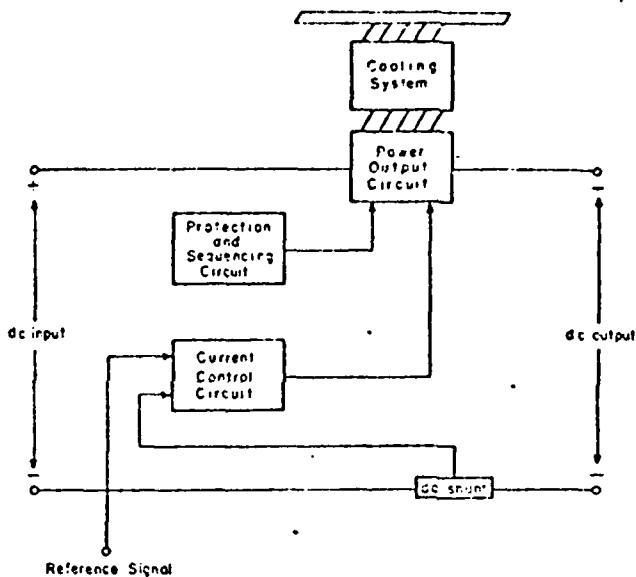


Fig. 2. Functional Diagram of the Current Regulator.

The cooling system dissipates the heat of the power transistors in the power output circuit. The power output circuit controls the output voltage in response to a signal from the current control circuit. The current control circuit compares the reference and shunt signals to drive the output circuit, and provide the necessary gain and compensation to stabilize the current feedback loop. The protection and sequencing circuits reduce the output voltage to zero when an overtemperature or loss of coolant is detected. The sequencing part of the circuit orderly activates the power output stage and auxiliary circuits (low voltage power supplies, fans, etc.), when the ac input power to the regulator is first applied. The operation of the circuits that perform each of these functions is described in detail in Section III.

Power Output Circuit Cooling

One of the major design problems is that of how to dissipate the power developed by the voltage drop across the transistors in the power output circuit. This power is maximum at full load current (300 A) and minimum output voltage (about 25 V dc). This is 35 V drop at 300 A, or a dissipation of 10.5 kW. We selected water cooling to dissipate this power in a reasonable amount of space.

In the laboratory at MIT open cycle water cooling was already in use for some of the welding experiments and could be used for cooling the regulator. About 5 GPM of water was available at 25 psig and a temperature of 20-25°C. The specific heat of water is equivalent to about 4°C/kW/GPM; 10.5 kW would produce a temperature rise of about 8.4°C at a flow rate of 5 GPM. The maximum water outlet temperature of about 33.4°C would be satisfactory.

Selection of Power Transistors

Candidate NPN silicon transistors with power ratings (P_T) from 100 to 1000 W and voltage ratings (V_{CBO}) from 80 to 100 V were considered and assembled into the list shown in Fig. 3. Only metal encased transistors were considered; plastic devices and epoxy cast packages with multiple devices for power switching applications, which cannot be cooled as effectively as metal encased devices, were not considered.

Device	P_T (W)	Approximate Cost, \$/each	Cost, \$/kW
WT4324	1000	100.00	100.00
2N3578	300	14.00	47.00
2N6258	250	4.50	18.00
2N3682	160	2.00	12.50
2N3772	150	2.50	16.70
2N3055	115	1.00	8.70
2N6056	100	1.50	15.00

Fig. 3. 1980 Cost in Dollars/kW of NPN Silicon Power Transistors.

The cost in \$/kW shown in Fig. 3 illustrates two things about the effectiveness of power transistor costs. First, the cost in \$/kW increases as the power rating increases. Apparently, an 'economy of scale' does not exist; production quantity is dominant. Second, the \$/kW cost is roughly linear with its power rating for the types of devices considered. The cost Q in \$/kW follows the approximate relationship $Q \approx 0.1 P_T$, where P_T is the power rating in watts. For example, for a fixed power requirement (say 10 kW) the total cost of the transistors will be about ten times more if 1000 W devices are used instead of 100 W devices.

We narrowed our consideration to three representative devices: the WT4325, the 2N6258 and the 2N3055, with an approximate cost of \$100/kW, \$20/kW and \$10/kW, respectively. The WT4325 required 20-25 parallel devices since the cooling system design only provided for about 500 W/device. Specially fabricated water cooled heatsinks are required because this device has a 3-in square base not easily accommodated by standard water cooled heatsinks. The 2N6258 design required 80-100 devices and the 2N3055 design required 180-200 devices. The WT4325 design was rejected because of its high parts cost while the 2N3055 design was rejected because of its high assembly cost. The 2N6258 was selected because it required a moderate number of devices and moderate assembly costs.

III. DESCRIPTION

The regulator consists of the power output circuit, the current control circuit, and the protection and sequencing circuit. The power output circuit itself consists of an output stage which uses 96-2N6258

parallel transistors and a driver stage. The 96 transistors in the power output stage are mounted 12 each on 8 Wakefield type 120-26 water cooled heatsinks. In order to achieve the specified performance with the large number of parallel transistors, and individually water cooled heatsinks, special care had to be taken in designing and building the cooling system and power output circuits.

Cooling System

A total of ten heatsinks are used in the regulator. Eight heatsinks are used for the power output circuit, one for the driver stage, and one spare for expansion of the output stage. The thermal resistance junction-to-case ($\theta_{j/c}$) of the 2N6258 is given by the manufacturer as $0.7^\circ\text{C}/\text{W}$ and the maximum junction temperature (T_{jmax}) is 200°C . The water cooled heatsinks are operated electrically hot so that the mica insulating washer on the transistors can be avoided. This reduces the thermal resistance case-to-heatsink ($\theta_{c/h}$) from about $0.5^\circ\text{C}/\text{W}$ to about $0.1^\circ\text{C}/\text{W}$. The thermal resistance heatsink-to-ambient ($\theta_{h/a}$) is a function of the water flow rate. The ten heatsinks are in flow parallel so that the flow rate for each heatsink is 5 GPM/10 or 0.5 GPM. From the manufacturer's data, $\theta_{h/a}$ at this flow rate is about $0.6^\circ\text{C}/\text{W}$.

The safe power dissipation (P_s) for the transistors is based on the "safe" maximum junction temperature T_s and the ambient water temperature T_a . The dissipation is given by,

$$P_s = (T_s - T_a)/(\theta_{j/c} + \theta_{c/h} + \theta_{h/a})$$

To accommodate inaccuracy in water flow rate and temperature a safe junction temperature of 175°C is used, while the maximum water outlet temperature of 33.4°C is used as the ambient. This gives for the allowable power per transistor.

$$P_s = (175 - 33.4)/(0.7 + 0.1 + 0.6) \approx 100 \text{ W}$$

The total dissipation of 10.5 kW consists of 9.6 kW for the 96 transistors plus 0.9 kW for the emitter sharing resistors.

Circuits

Power Output Circuit. The complete power output circuit acts as a power amplifier to provide 0-60 V output at 300 A with a 1 V change in input signal.

Each of the eight identical heatsinks shown in Fig. 4 contains 12 power transistors, emitter sharing resistors, fusing, varistors for voltage transient protection for each group, and a thermal overtemperature protection switch. The emitter sharing resistor R_e is selected to limit the variation in emitter current to 10% of the average full load per device current of 3.125 A for a variation of 0.25 V in V_{BE} . This gives

$$R_e = \frac{\Delta V_{BE}}{\Delta I_e} = \frac{0.25 \text{ V}}{0.1 \times 3.125 \text{ A}} = 0.8 \Omega$$

with 1 Ω selected for use in the final design. The power dissipated in each sharing resistor is about 10 W so

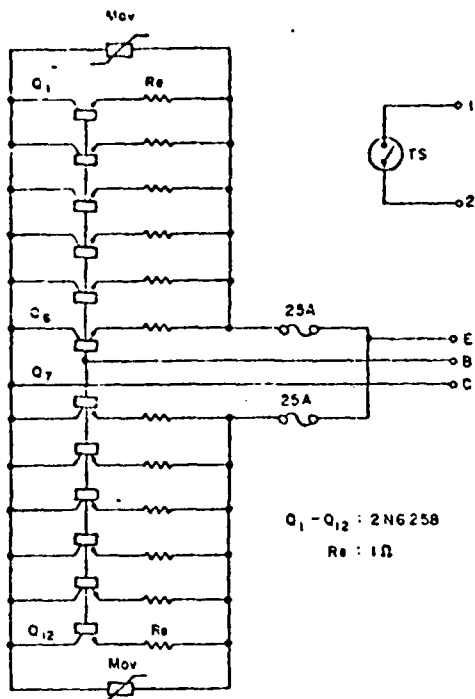


Fig. 4. Schematic of Output Stage Heatsink Circuit.

that the 96 resistors dissipate about 960 W. Each of the identical heatsink assemblies has an emitter, base and collector connection for the transistor and 2 connections for the thermal switch. These 5 connections per heatsink serve to parallel the 8 output stage heatsinks and connect the output stage to the rest of the current regulator.

The driver stage shown in Fig. 5 amplifies a 0-15 V signal provided by the current control circuit to provide the base drive for the output stage transistors. The driver stage uses 6 parallel 2N6258 devices to provide the required power dissipation.

The Current Control Circuit. The current control circuit maintains the output current of the current regulator within 1% of the level commanded by the reference signal. It also provides a bandwidth of the feedback loop to yield a response to a step change in the reference signal of a settling time of 100 μ s or less and an overshoot of 5% or less.

The current control circuit is illustrated by the block diagram of Fig. 6. The two input signals are the 0-100 mV feedback signal from the 300 A shunt and the 0-10 V current reference signal. These signals are scaled to 0-1 V full scale by a precision divide-by-ten and a precision multiply-by-ten circuit respectively. The two 0-1 V signals are subtracted to form an error signal which is then multiplied by 100 in two successive multiply-by-ten circuits, and amplified by a voltage following circuit to provide the current needed to drive the power output circuit.

The schematic of the current control circuit is shown in Fig. 7. In order to use standard components

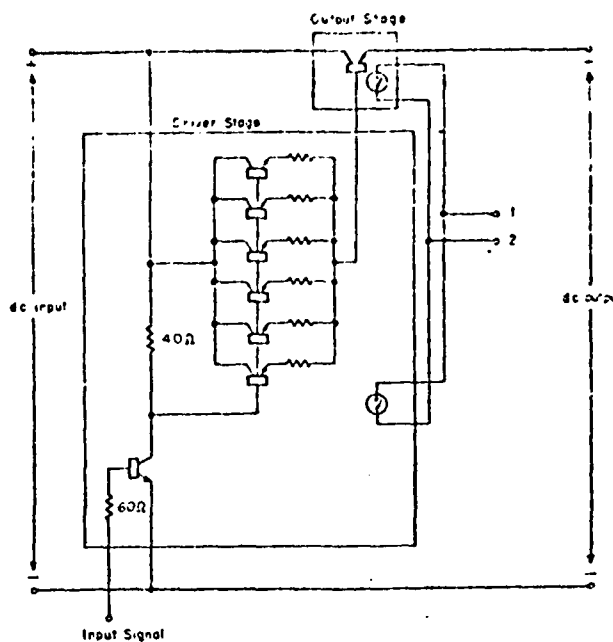


Fig. 5. Schematic of the Power Output Circuit Showing the Driver Stage Circuit.

throughout the regulator a standard IC OPAMP, the LM741 was used in the divide-by-10 and multiply-by-10 circuits. Since the gain-bandwidth product of the LM741 is 1 MHz, each of the gain stages using this amplifier is limited to a gain of 10. This gives the regulator a maximum bandwidth of about 100 kHz so that the feedback loop bandwidth of 20 kHz can easily be attained. The slew rate of the LM741, about 0.5 V/ μ s, led to the arrangement of the amplifier circuits so that the full scale voltage swing of the output signal is about 1 V. This does not reduce the slewing rate of the output current.

Protection and Sequencing Circuit. The purpose of the protection circuit is to disable the power output circuit, which reduces the output voltage to 0 V, when one of two conditions occur: (1) the loss of water pressure in the cooling system; (2) an overtemperature condition on one of the water-cooled heatsinks. The sequencing circuit also holds the power output circuit disabled for a delay period, about 1 s, after the power supply is first turned on. This delay period is used to charge a capacitor bank in the power supply to the potential of the dc input bus. It also allows the low voltage power supply used by the current control circuits to stabilize so that it is operational when the power output circuit is enabled after the delay.

The operation of the protection and sequencing circuit is illustrated in Fig. 8. When the 120 V ac power is first applied by closing switch S1, the internal 12 V dc power supply energizes relay K₁. A set of contacts on relay K₁ closes, causing capacitor bank C₁ to begin charging to the input bus voltage through R₁. During this period C₂ is charged through R₂ which delays the energizing of relay K₂ by about 1 s. When relay K₂ is energized, the K_{2A} contacts on relay K₂

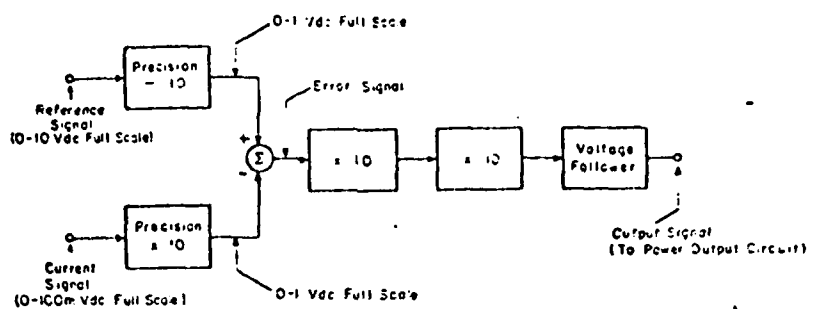


Fig. 6. Block Diagram of the Current Control Circuit.

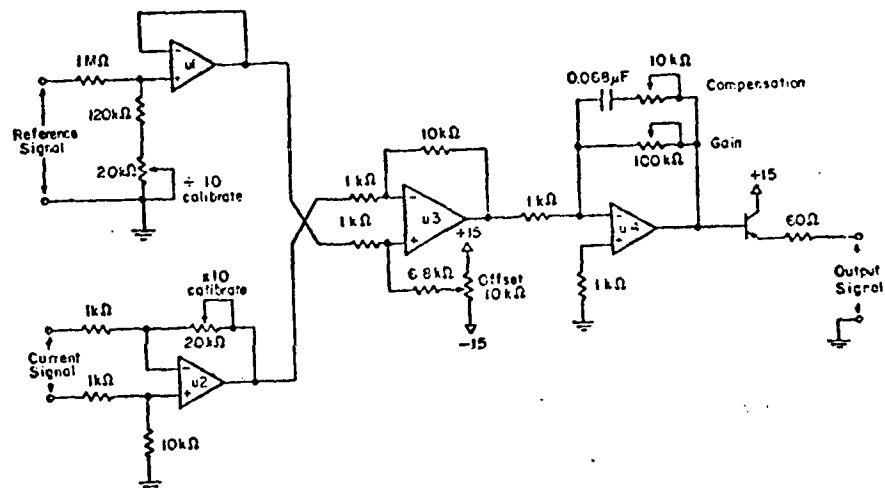


Fig. 7. Schematic of the Current Control Circuit.

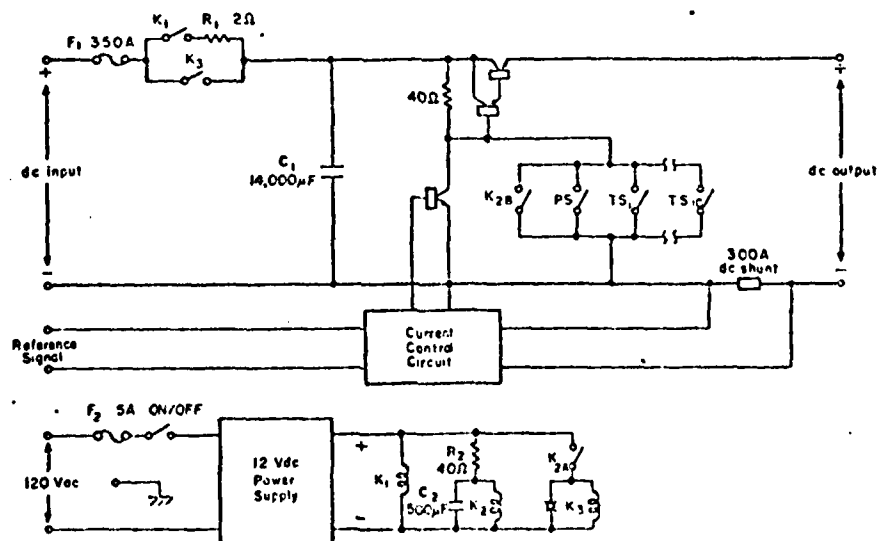


Fig. 8. Schematic of the Current Regulator Showing the Protection and Sequencing Circuit.

close and the K_{2B} contacts on relay K₂ open. The K_{2A} contacts energize relay K₃. The K₃ contacts connect the high current input bus to the internal collector bus of the power output circuit. At the same time the K_{2B} contacts open, enabling the drive signal to the power output circuit. At this point the power output circuit will be enabled as long as sufficient water pressure keeps switch PS opened and an over-temperature condition does not occur on any one of the water cooled heatsinks.

Performance

An Airco Model CV-450 welding power supply, rated at 450 A, 50 V dc was used as the dc input source to the regulator for most of the tests. The tests were performed once using a 0.1 Ω resistive load at reduced current and again using a Gas-Tungsten arc at full current. Fig. 9 is a photograph of the current regulator with the cover removed during testing at MIT.

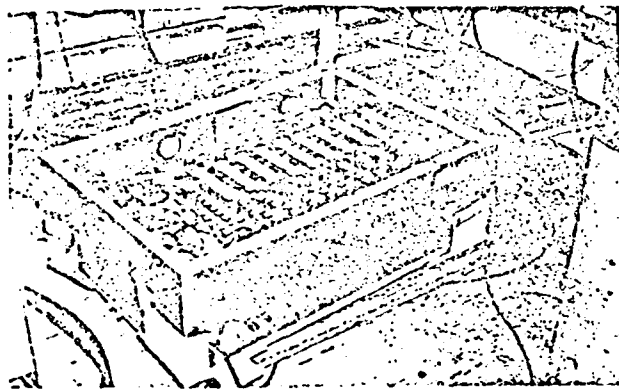


Fig. 9. Photograph of the Current Regulator.

The regulator was first tested against load variation by setting the load current to 20 A and observing the current variation while changing the load over the range 0.05 to 0.15 Ω. The current variation was measured using the front panel 3-1/2 digit digital panel ammeter calibrated for 1 count per A with an accuracy of $\pm 1/2$ count. The current variation could not be measured using this meter and was therefore less than 1 A. The line regulation was next measured by setting the current to 20 A using a 0.1 Ω load and then varying the input voltage from 35 to 50 V. A current variation of 1 A was measured using the front panel ammeter.

To test the power dissipation capability of the current regulator a 1-ft length of No. 6 wire was used to short the output terminals with the input voltage at 45 V. The power supply was then operated successfully for 5 s with the output current set to 100 A, 200 A and 300 A and about 5 GPM water flow to test the short time power rating. The test was repeated at 200 A to test the long-term power rating. After about 30 s the thermal protection circuit operated because of an apparent water flow blockage in one of the heatsinks.

Final testing was performed using an arc load. A 500 Hz square wave with a dc bias was applied to the reference signal input terminals of the power supply. The reference signal and the shunt signal from the power supply were then observed on a dual trace oscilloscope. Fig. 10a shows the response to a 400 Hz square wave signal with the current shifting between 60 A and 120 A. The risetime (from 10% to 90%) is about 15 μs, while the overshoot is about 25%. The response to a 1 kHz square wave signal is shown in Fig. 10b for a current between 50 A and 250 A. The risetime is about 50 μs and the overshoot is about 30%.

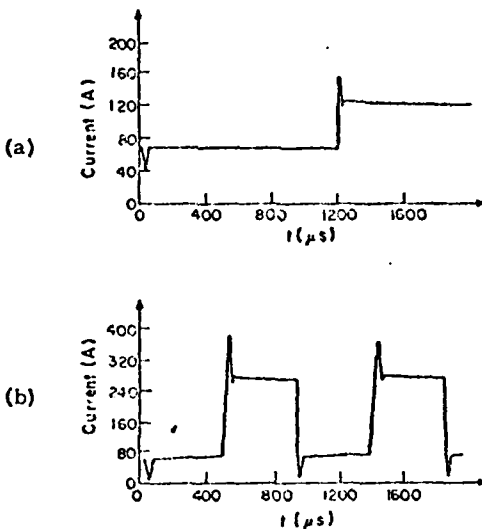


Fig. 10. Waveforms Showing (a) 400 Hz and (b) 1 kHz Square Wave Response.

IV. GTA WELDING RESEARCH

Pulsed current waveforms are used in advanced Gas-Tungsten-Arc (GTA) welding to improve weld quality. These waveforms usually consist of rectangular pulses superimposed on a constant current. Commercial thyristor power supplies for GTA welding can produce current pulses at frequencies up to about 25 Hz. The improvement in weld quality is attributed to enhancement of the arc stability, control of weld puddle motion and efficiency of the weld process.

The analysis of the thermal, electrical and fluid mechanism of the arc is complicated. Because of this, no analytical method exists as yet for predicting the influence of a particular waveform on these properties. One goal of GTA welding research using the fast response current regulator is to identify and measure basic arc properties that are affected by the ac components of the arc current. These properties include: the force exerted on the weld puddle by the arc; electromagnetic stirring of the arc; skin effect in the weld puddle.

Measurement of Arc Velocity

The force exerted on the weld puddle by the arc is related to the plasma jet momentum, which varies directly with arc velocity [1]. This force depresses the surface of the weld puddle as shown in Fig. 11. In one of the experiments using the fast-response current regulator, a step change in the arc current alters the arc velocity which is measured using a novel optical method.

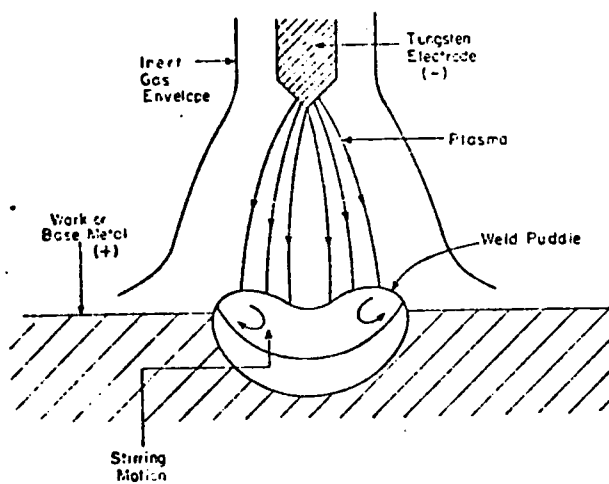


Fig. 11. Diagram of GTA Welding Setup Showing the Shape of the Weld Puddle.

The arc current is subjected to a 60 A step increase with a 15 μ s rise time and a 50 μ s settling time. The increase in arc current causes the arc to become hotter and emit more light. The light intensity is measured by projecting the arc image onto a viewing screen as shown in Fig. 12. The light intensity of a particular region of the arc as the arc responds to the change in current is measured by a photodetector behind a hole in the viewing screen. The light intensity of the arc is observed on an oscilloscope and is photographed along with the arc current as shown in Fig. 13 for increasing distances from the electrode.

Fig. 13 shows that, for each particular distance from the electrode, the light intensity increases at two distinct rates after the change in arc current. The intensity increases at one rate up until a small bend or glitch in the rate occurs. After the bend the intensity increases at a higher rate. The timing of the bend in the waveform is proportional to the distance from the electrode because the bend represents a "wave" of hotter plasma produced by the increased arc current. As the wave travels from the (-) electrode to the (+) electrode or work plate, it separates a cooler region of the arc (in front of it) from a hotter region (behind it). The velocity of the wave is related to the velocity of the plasma, so that measured data like Fig. 13 can be used to calculate the velocity of the plasma.

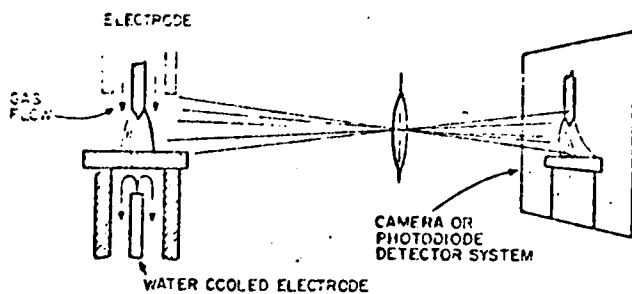


Fig. 12. Test Setup for the Arc Velocity Experiment.

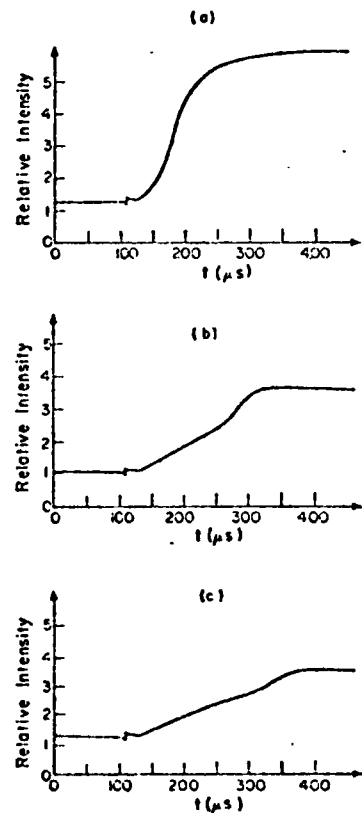


Fig. 13. Waveforms Showing Relative Light Intensity After a 60 A Step Increase in Arc Current. Measurements Taken at (a) 4.5 mm; (b) 9 mm; and (c) 11 mm From the Electrode.

V. GMA WELDING RESEARCH

Gas-Metal-Arc (GMA) welding differs from GTA welding; the electrode material (not Tungsten) is consumed in the welding process. In automatically controlled welding, a wire-type consumable electrode is fed into the arc from a spool at a

constant rate. The wire is of a material similar to the base metal on which the welding is being performed. As the welding progresses, the metal of the wire is melted, transferred by the arc to the work and is deposited in the weld puddle where it becomes part of the material in the welded joint or seam.

The melting process of the consumable electrode is an important factor in the quality of GMA welding. As the electrode material melts, it forms small droplets at the end of the electrode. The melting continues until the droplet is large enough and then is transferred by the plasma to the work. Several mechanisms which initiate the transfer of the droplets include, the rate at which the electrode is melting; electromagnetic effects which shape the droplet; surface tension which shapes the droplet; vibration, gravity, etc. which separate the droplet from the electrode. The improper or irregular formation of droplets can cause an uneven distribution of metal in the weld or splattering of the metal, generally decreasing the quality of the weld. The time for droplet formation is on the order of 1 ms for materials such as aluminum and titanium. The droplet information is more regular for constant control of arc current with corresponding improvement on weld quality.

In GMA welding research pulse currents are used to investigate the formation and transfer of electrode material droplets. Because the natural time period for droplet formation is on the order of 1 ms, a current regulator with response about ten times faster is needed to perform properly controlled experiments. One goal of the research is to identify pulse current waveforms which will induce droplet formation and transfer in a controlled fashion, thereby producing highly regular metal transfer across the arc, to increase the uniformity and quality of the welded seam. Results of this research were not available at the time of writing of this paper. Changes from baseline waveforms will be used to identify changes in weld quality with parameters such as pulse width, shape, repetition rate, average and peak currents. The resulting body of data will be used as guidelines in the selection of pulse waveforms for various materials and current levels. The experiments will make use of a power supply with a fast response regulator similar in design to that presented in the paper. This power supply will be rated 600 A continuous output and peak currents to 1000 A. One of four identical power modules that will be used in this power supply is shown in the photograph of Fig. 14.

VI. COMMERCIAL APPLICATIONS

The fast response current regulator described in this paper is designed as a research tool. However, a power supply with this type of regulator can be applied to commercial welding. Such a fast response power supply is best suited to welding of commercial and military products where precise current control and/or special current waveforms are needed. These applications include, nuclear reactor vessels, cryogenic piping and containers, and submarine hulls.

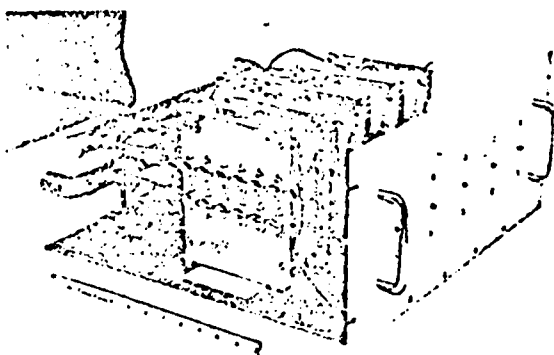


Fig. 14. Photograph of One of Four Power Output Modules for a 600 A Current Regulator.

In most commercial welding applications the wide range of waveforms that can be generated by the current regulator described in this paper are not needed. However, because of the versatility of this current regulator it can be used to investigate the requirements for any type of welding within the limitations of its current rating, in order to specify a special-purpose power supply that meets the exact needs of a particular type of welding. Compared to this research power supply, a special purpose power supply will probably use switching transistors or thyristors to be more efficient, less bulky, less costly and simpler to operate. The eventual result will be better welding quality control and higher productivity.

V. CONCLUSIONS

Our design, construction and testing of the fast-response current regulator lead to the following conclusions:

1. A linear transistor current regulator can be used to investigate arc phenomena with time constants as short as 1 ms. Thyristor phase-controlled rectifiers and transistors or thyristor chopper regulators are not fast enough to regulate the current while these phenomena take place.
2. A linear transistor current regulator using multiple parallel power transistors can achieve step changes in arc current in excess of 100 A, with settling time of less than 100 μ s. A small signal bandwidth of 20 kHz can be attained with this design.
3. The fast-response current regulator described in this paper is an effective research tool for both GTA and GMA welding.
4. Commercial welding where extremely stable arc current or special current waveforms are required can benefit from investigations using the fast-response current regulator described in this paper.

REFERENCES

- [1] J. Converti and W. Unkel, MIT, "Plasma-Jet Momentum", presented at 33rd Gaseous Electronics Conference, Norman, OK, 1980.

APPENDIX C

Presented at a Conference on Welding Consumables
and Process Developments
Peoria, IL, September 1981

SIGNAL ANALYSIS OF VOLTAGE NOISE IN
WELDING ARCS

E. Elias[†] and T. W. Eagar ^{*}
Massachusetts Institute of Technology

ABSTRACT

Gas tungsten arc welds have been made on low alloy steel plates to which intentional defects (discontinuities) have been imposed. Disruption of shielding gas, welding over surface films, tack welds etc., all produce changes in what is otherwise a relatively uniform voltage signal. The arc voltage was 15 volts \pm 2 volts with 300 mV ripple noise from the power supply. The changes in this steady noise voltage varied from 50 mV to less than one millivolt depending on the severity and the type of change experienced. In some instances the changes are easily detected by analysis of the signal in real time, while in other cases the signal had to be transformed to the frequency domain in order to detect the changes. Although use of frequency spectrum analysis is currently too expensive for any but the most critical welding applications, the promise of low cost computation in the next decade makes even this complex technique potentially attractive in the future.

The technique has detected discontinuities as small as 1.5 mm in length. The ultimate sensitivity and reproducibility of the technique is still being investigated.

INTRODUCTION

Automation of welding is essential for improved productivity and reliability, yet one of the major problems

[†]Department of Electrical Engineering

^{*}Department of Materials Science and Engineering

associated with automation is development of low cost, rugged sensors. In the present study the noise voltage from a gas tungsten arc has been monitored as a means of detecting changes in the process. An advantage of this type of sensor is that the probe is simple and inexpensive. Indeed, the two voltage leads are probably the simplest of all possible probes.

The probe actually being used is the welding arc plasma itself. The plasma has the advantage of responding to both chemical changes and geometric changes on a time scale of microseconds. Chemical changes in the plasma are caused by vaporization of impurities on the surface or by vaporization of metal from the weld pool or by disturbances in the shielding gas. These ions alter the electrical conductivity of the gas, thereby altering the voltage. High speed spatially resolved spectroscopy indicates that the ions traverse the arc in a time of ten microseconds or less (1).

Geometric changes in the workpiece change the shape of the plasma, which in turn causes a change in the arc voltage. These changes also occur on a microsecond time scale. This voltage fluctuation with changes in joint geometry has been used commercially to control the length of the gas tungsten arc and to track a weld seam in a groove. Neither of these uses, however, has exploited time resolution of the changes above approximately 100 Hz. This is due primarily to the slow speed of the mechanical systems needed to move the electrode. In the present study, changes in the voltage signal have not been used to control the arc, but rather to determine if a disturbance has occurred. Mechanical restrictions do not apply, with the result that oscillations to 50 kHz or higher may be studied.

It is well known that an experienced welder listens to the arc to determine if it is operating properly. In many instances, disturbances in the process may be detected by this acoustic signal before their effects are seen in the weld pool. Partial loss of shielding gas may produce crackling sounds without altering the visual appearance of the weld at all, yet the resulting contamination from the atmosphere may reduce the mechanical properties of the joint significantly. Shaw has correlated the light emission from the plasma with the arc voltage fluctuations to frequencies of 20 kHz (2). It is likely that the acoustical signals detected by the welder are also correlated with the noise voltage. For these reasons, it was decided that fluctuations between 60 Hz and 10 kHz represented a useful starting point for the signal analysis. Voltage was chosen since it responds more

rapidly than current to changes in an inductive system. Acoustic techniques were not used as they are susceptible to interference from extraneous sources.

The major disadvantage to using the arc itself as the sensor is that the plasma responds to many different things. Reduction of the signal to a useable form is the most significant problem encountered. The purpose of the present study was to determine if intentional disturbances to a gas tungsten arc could be detected in the welding noise voltage signal.

EXPERIMENTAL

The measuring circuit for the welding voltage noise is shown in Figure 1. The welds were made with an SCR transformer-rectifier power supply at 100 amperes and 15 volts electrode negative. The signal was monitored on an oscilloscope and recorded on an open reel AM tape recorder. A

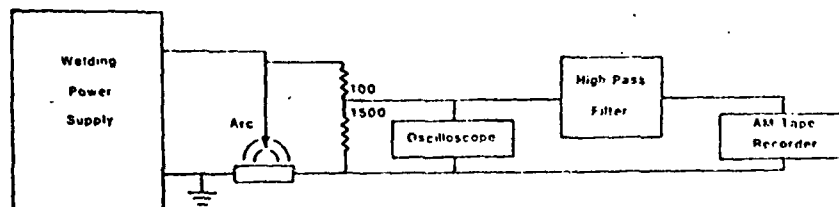


Figure 1

high pass filter with a cutoff of 20 Hz was used to reduce the low frequency noise coming from the power supply. The high frequency rolloff of the tape recorder was measured at approximately 24 kHz which is much higher than the frequencies of interest.

The base metal was sand blasted carbon steel plate. Argon gas at a flow rate of 30 CFH was used for shielding. Disturbances were introduced both by turning on a transverse

air jet and by welding over copper inserts in the steel plate. The inserts were brazed in place and machined smooth prior to welding. The second channel of the stereo tape recorder was used to mark the location of the disturbed signal on the first channel of the magnetic tape by imposing a constant frequency sinusoidal input during the time of the disturbance.

Considerable attention was given to detection of a reproducible signal. Several grounding and voltage lead configurations were tested until the background noise was reduced to several millivolts peak to peak. The remaining noise was periodic in time, and since only relative changes were of interest, this small noise signal was thought to be insignificant.

The recorded waveforms were transferred to a PDP 11/45 computer in the MIT Digital Signal Processing Laboratory. These signals could then be studied at length in either the time domain or the frequency domain by performing a Fast Fourier Transform (FFT).

RESULTS

Figure 2 shows several periods of a weld over a clean steel plate with no disturbance imposed. The period of these oscillations is 120 Hz with a range of 350 mV peak to peak. Numerous welds made at different times and different conditions confirmed that this signal was uniform and consistent

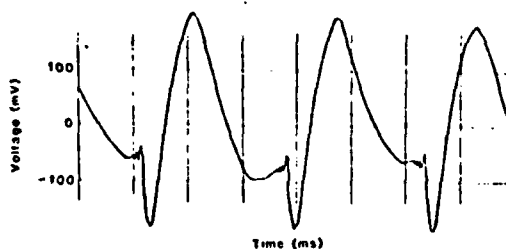


Figure 2

provided the arc was not disturbed. Indeed, the signal in Figure 2 is very similar to that obtained by running 100 amperes through a 0.3 ohm carbon block resistor using the same power supply. It was concluded therefore that the signal in Figure 2 is essentially the noise voltage generated within the power supply. These fluctuations are not due to changes in the welding arc plasma, yet they do induce a

disturbance at the arc itself.

Figure 3 shows the same signal with a disturbance in the arc caused by a transverse jet of air. It should be noted that the disturbance was minor, with little variation as

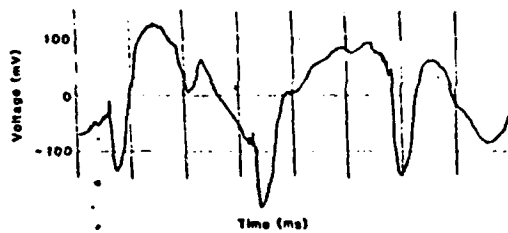


Figure 3

perceived by the operator. The signal has changed noticeably, nonetheless, portions of the power supply noise voltage (cf. Figure 2) may still be detected.

Figures 4 and 5 show "good" and "bad" welds produced by welding on a steel plate contaminated with a 3 mm bead of

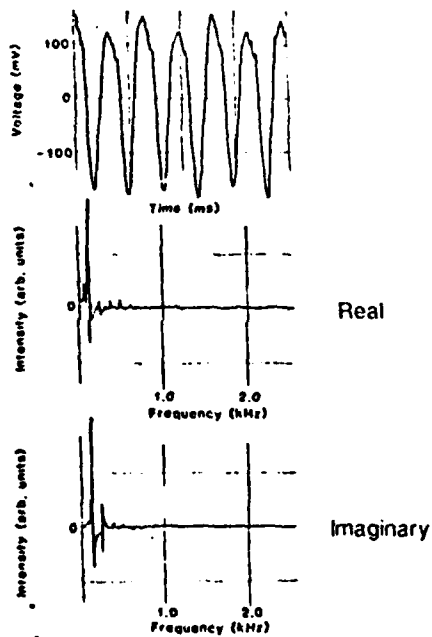


Figure 4

copper. Figure 4 shows both the time domain and frequency domain signals for the good weld made on the steel alone, while Figure 5 shows the same signals in the contaminated regions. It will be noted that the changes in the time domain are barely discernable while the frequency domain shows a significant difference.

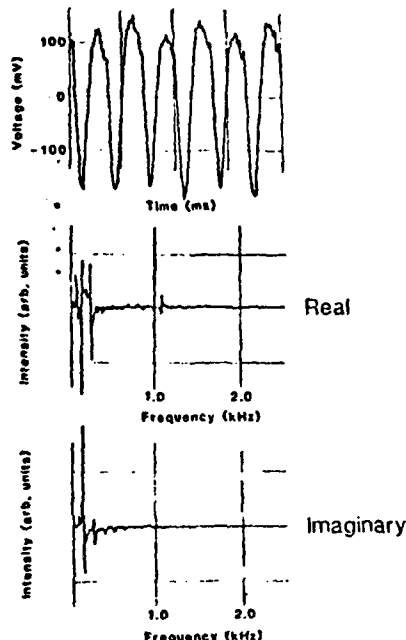


Figure 5

DISCUSSION

These studies have shown that disturbances in the welding arc plasma may be detected in the welding noise voltage signal. In some instances the changes are readily seen in the time domain, while in other cases, the change is more readily distinguished in the frequency domain.

The specific reasons for the changes are not well understood at this time. One observer has suggested that the arc oscillates about the electrode tip and that the period of this oscillation is a function of the arc length (3). This could easily explain the disturbance caused by the transverse air jet, yet it does not explain the distinct frequency observed when welding over the copper contamination at constant arc length.

Several important problems remain to be studied before this technique can be developed further. First, it is desirable to improve the signal to noise ratio. The power supply oscillations are many times greater than the disturbances which are of interest. Fortunately, at least for the gas tungsten arc process, the power supply fluctuations are periodic and may be subtracted from the total signal by using more complex signal analysis techniques. Alternatively, transistorized power sources can produce much cleaner signals.

Secondly, it is necessary to develop an understanding of the form of the voltage disturbance produced by a given disturbance in the weld. It is not clear at this point whether disturbances in the weld zone will produce characteristic signatures in the voltage wave form. If the response is not predictable, all that this technique can do is determine that some change has occurred. It would be much more valuable if the type of change could also be determined.

Thirdly, the process, if feasible, must be performed in real time. The off line analysis used in this study provided a number of simplifications. If the process is to be used in production, special equipment must be used. The prospect of very large scale integrated (VLSI) circuitry coupled with the speed of a hardwired FFT program at least yields the promise that the technique may be practical in future years. For the present, it is necessary to demonstrate the full potential of the signal analysis before contemplating the development of real time equipment.

It is unlikely that consumable electrode processes will be amenable to this technique of analysis unless the droplet formation and detachment is made more uniform. Pulsed current welding machines may provide the necessary uniformity.

SUMMARY

Signal analysis of the high frequency voltage fluctuation in gas tungsten arc welds has shown that disturbances in the process may be detected. It remains to be shown whether these fluctuations are specific enough to use as a means of controlling the welding process. If several remaining problems can be solved, noise voltage signal analysis could provide a sensitive technique for monitoring many changes in the welding process.

ACKNOWLEDGEMENTS

The authors wish to thank the Office of Naval Research and the National Aeronautics and Space Administration for partial support of this study.

REFERENCES

- (1) R. J. Klueppel, D. M. Coleman, W. S. Eaton, S. A. Goldstein, R. D. Sacks and J. P. Walters, "A Spectrometer for Time-gated Spatially Resolved Study of Repetitive Electrical Discharges," Spectrochimica Acta. 33B, 1978, p. 1-30.
- (2) C. B. Shaw, Jr., "Diagnostic Studies of the GTAW Arc," Weld J. 54(2), February 1975, p. 33-s.
- (3) R. W. Richardson, private communication, Ohio State University, Columbus, Ohio, 1981.
- (4) Y. Arata, K. Inoue, M. Futamata and T. Toh, "Investigation of Welding Arc Sound (Report III) - Effects of Current Waveforms on TIG Welding Arc Sound," Trans. JWRI, 9(2), 1980, p. 25.

Laser Welding of Aluminum and Aluminum Alloys
Submitted for publication in the Welding Journal

C. A. Huntington and T. W. Eagar

Materials Processing Center

Massachusetts Institute of Technology

Cambridge, Massachusetts 02139

ABSTRACT

The effects of surface preparation and joint geometry on laser power absorption by pure aluminum and by alloy 5456 have been studied. The results indicate that initial absorption varies from a few percent to more than 25 percent depending upon the surface preparation. The fraction of absorbed power increases dramatically upon formation of a keyhole. As a result, welds made with sharply beveled edge preparation are larger and more uniform than those made with either bead on plate or square butt preparations.

INTRODUCTION

The high energy density laser and electron beam welding processes characteristically produce a deep, narrow weld bead. This bead is formed by a keyhole mode of operation in which the keyhole cavity is produced by metal vaporization at power densities of 10^5 watts/cm² or greater. There are, however, significant differences between the two processes: lasers heat with photons of approximately 0.1 eV energy while electron beams use particles of 100,000 eV energy. This results in a beam of laser light which readily interacts with the free electrons found in the plasma. The plasma is formed by vaporization of the surface of the metal and this interaction defocusses part of the incident beam producing a characteristic "nail-head" type of weld. (1) The electrons of an electron beam, on the other hand, are too energetic to be deflected significantly by the plasma. As a result, it is possible to couple the energy much more efficiently with electron beam welding systems as compared with laser welding systems. One of the most dramatic illustrations of these differences in beam characteristics occurs when welding aluminum. Aluminum is one of the easiest metals to penetrate with an electron beam, while it is one of the most difficult to melt with a laser. The poor coupling of the laser energy is due in part to the high density of free electrons in the solid, which makes aluminum one of the best reflectors of light. In addition, many aluminum alloys contain magnesium or zinc which are easily vaporized thereby forming a plasma which blocks the incident beam.

Previous investigations have shown low power absorption (2), alloy compositional differences (3) and the importance of surface preparation (3) when laser welding aluminum. The power absorption changes dramatically at times, producing an unstable process with poor penetration control and a rough bead surface. It is commonly believed that the difference in the fraction of

absorbed power is caused by melting of the metal. (1, 4)

Although it is well known that alloy composition and surface preparation of aluminum influence the absorption of laser light, the purpose of this study is to quantify these differences in order to determine the degree of control that can be achieved by modifications of either the material or of the process.

EXPERIMENTAL

Both pure aluminum (99.999 percent) and 5456 alloy (5.1% Mg with minor additions of Mn and Cr) were used for the absorption experiments. Actual welds were made on 1100 (99.0% Al) and 5456 alloy plate of one quarter inch thickness.

Four different surface preparations were studied. The as-received surface of 5456 was mill finished while the pure aluminum was machined on a lathe. Other samples were sandblasted with -300 mesh glass beads, anodized to one micron thickness, or electropolished in an alcohol-water-perchloric acid solution.

The absorption studies employed a 0.375 inch diameter sample machined as a cone on one end with the flat test surface on the opposite end. This cone was pressed into a holder as shown in Figure 1. The holder surrounded the conical end and absorbed all light beamed into this cavity. A thermistor was mounted on the holder which recorded the temperature rise of the sample and holder after each laser pulse. By beaming into the cavity, the total beam power was measured. By turning the entire assembly around, the absorbed power of the laser pulse on the flat surface could be measured. The ratio of the temperature rise on the flat surface to that produced by beaming into the cavity gives a direct measurement of the absorbed power.

The entire holder and sample weighed 6.5 grams, which allowed accurate measurements of absorbed power as small as two joules. For lower power

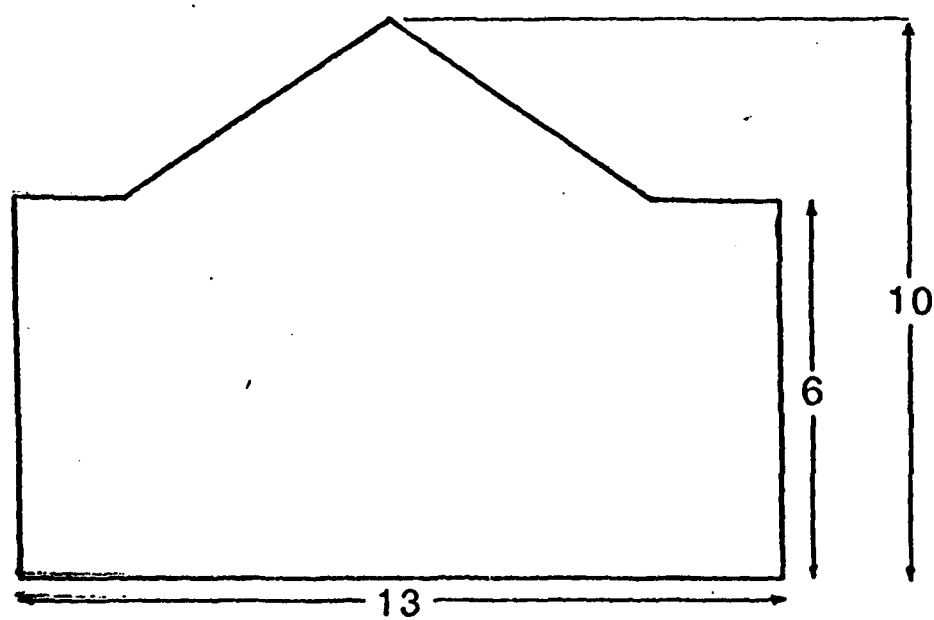
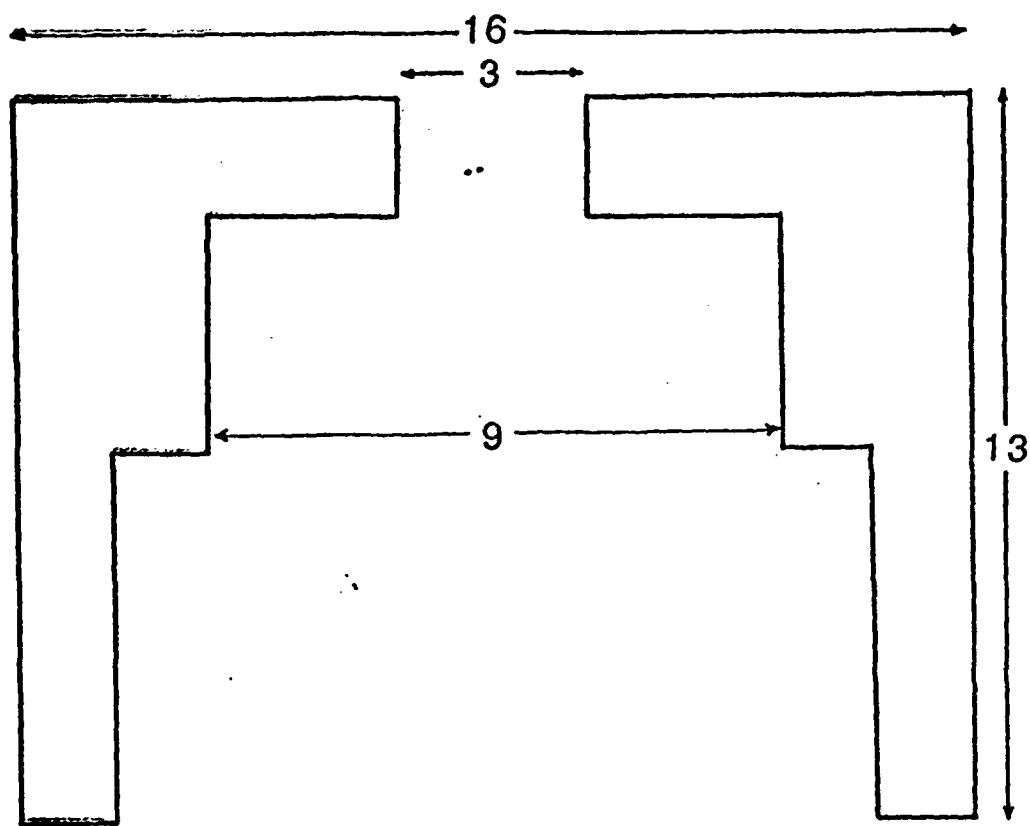


Figure 1

absorption a smaller holder and sample was employed which weighed 0.8 grams total.

The power absorption studies were performed with both a 200 Watt and a 1300 Watt Coherent Radiation CO₂ laser. The higher power laser was operated in the gaussian mode. Welds were produced on a Spectra Physics 5 kW laser operating in the unstable resonator mode.

RESULTS AND DISCUSSION

Table 1 illustrates the effect of surface preparation on power absorption for a 200 joule, 2 second pulse. It will be noted that sandblasting and anodizing significantly increase the absorbed power, while electropolishing decreases the absorption somewhat. The increased absorption of the anodized sample is no doubt due to the decreased free electron concentration at the surface. The one micron anodized layer is in principle too thin to interact directly with the 10.6 micron radiation, but the decrease in charge carriers near the surface still has an influence. Scanning electron microscopy revealed that the high absorption of the sandblasted samples was most likely due to light absorption by glass beads embedded in the surface. The as-received samples produced considerably more scatter in the measurements, presumably due to local differences in oxide thickness in 5456 alloy and surface roughness variations in the pure aluminum. The smooth electropolished samples have the highest reflectivity of all.

Although it is not immediately apparent from the data in Table 1, the 5456 alloy usually had a slightly higher absorption than the pure aluminum of similar surface preparation. This is confirmed by more than 100 measurements; the alloy has an absorption coefficient which is approximately 20 to 25 percent larger than the pure aluminum. The differences at low absorption powers are less

Table 1. Percent power absorbed from a 200 Joule,
two second pulse.

<u>Surface Preparation</u>	<u>5456 Alloy</u>	<u>99.999 pure Al</u>
Anodized	27	22
Sandblasted	22	20
As received	5-12*	7
Electropolished	4	5

* Mill finished samples exhibited considerably more scatter than laboratory prepared surfaces.

pronounced due to greater experimental error, but the trend is consistent throughout this study. The most likely explanation is the lower free electron concentration in the alloy material. It will be noted that the differences in absorption due to alloy composition are much less than those due to surface preparation.

At higher beam power, melting will occur as shown in Figure 2. This melting was confirmed by inspection in the scanning electron microscope as shown in Figure 3. It will be noted from Figure 2 that the absorption increases dramatically in some instances at the higher powers. SEM study confirmed that this high absorption coefficient is due to the formation of the keyhole rather than the onset of melting as commonly believed (1, 4). This is seen even more clearly in Figure 4 which indicates low absorption power over a range of power inputs even when surface melting occurs. If high absorption coefficients are to be achieved, a keyhole must be formed.

As a further test of whether a keyhole or melting is responsible for high power absorption, flat bottomed holes 2.4 mm in diameter by 6.2 mm deep were milled in each alloy. The absorption in each of these "keyholes" was measured with the results as shown in Table 2. It will be noted that the absorption coefficient power is generally much greater in the artificial keyhole than would be expected on a flat surface. In this case the keyhole acts like a cavity, reradiating the power between the walls until most of it is absorbed. It will further be noted that the absorption of the pure aluminum is greater than the 5456 alloy in the keyhole. This is believed to be due to generation of a magnesium vapor plasma in the 5456 alloy keyhole. This plasma absorbs the incident light, thereby reducing the effective depth of the keyhole. It appears from these results that the keyhole geometry is more important than surface preparation in determining the power absorption characteristics of pure

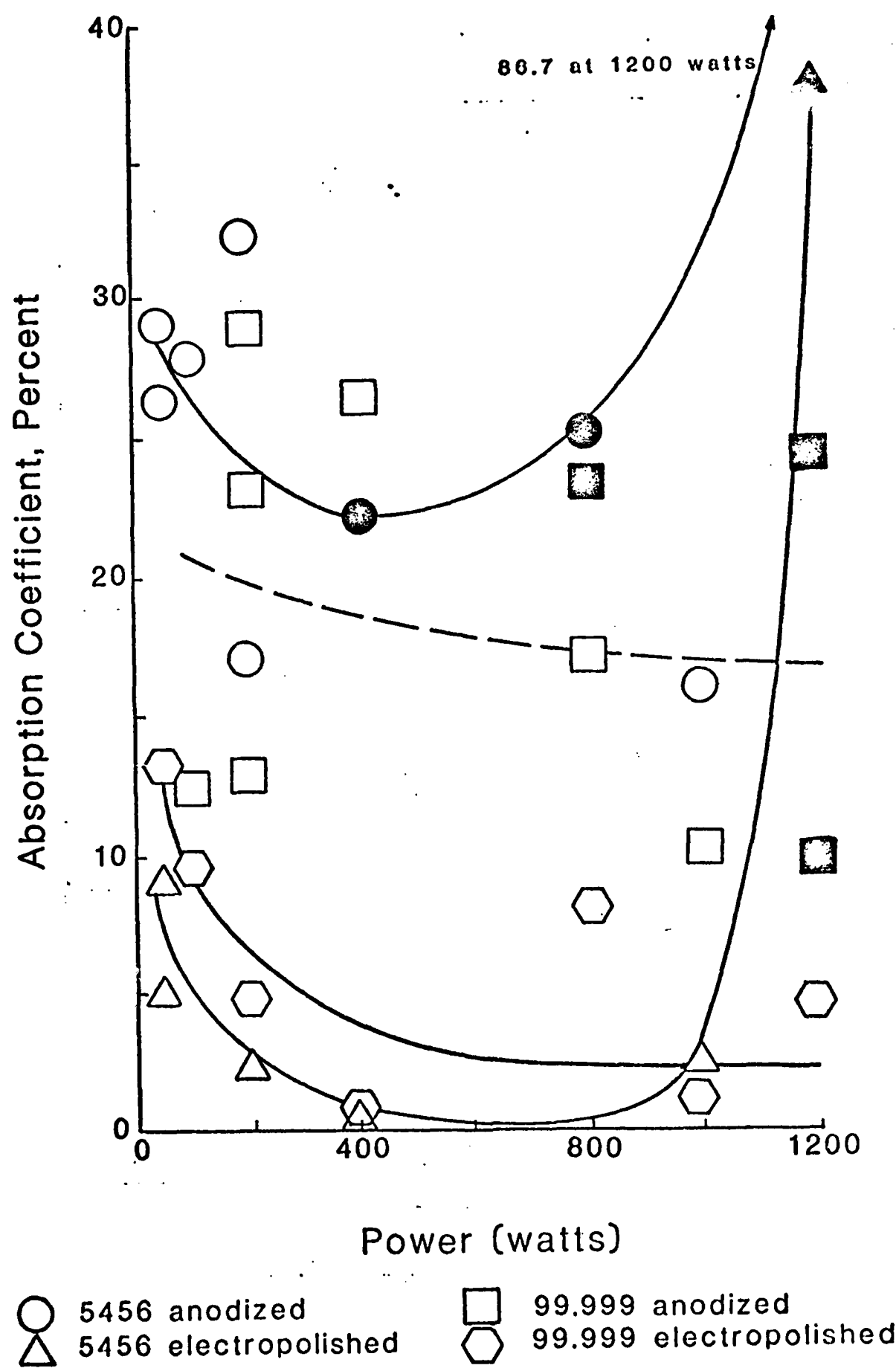


Figure 2

Table 2. Absorption in drilled keyhole,
percent, 0.5 sec pulse.

	<u>5456</u>	<u>99.999</u>
400 watts	3	100
500 watts	23	66
1200 watts	17	35



Figure 3

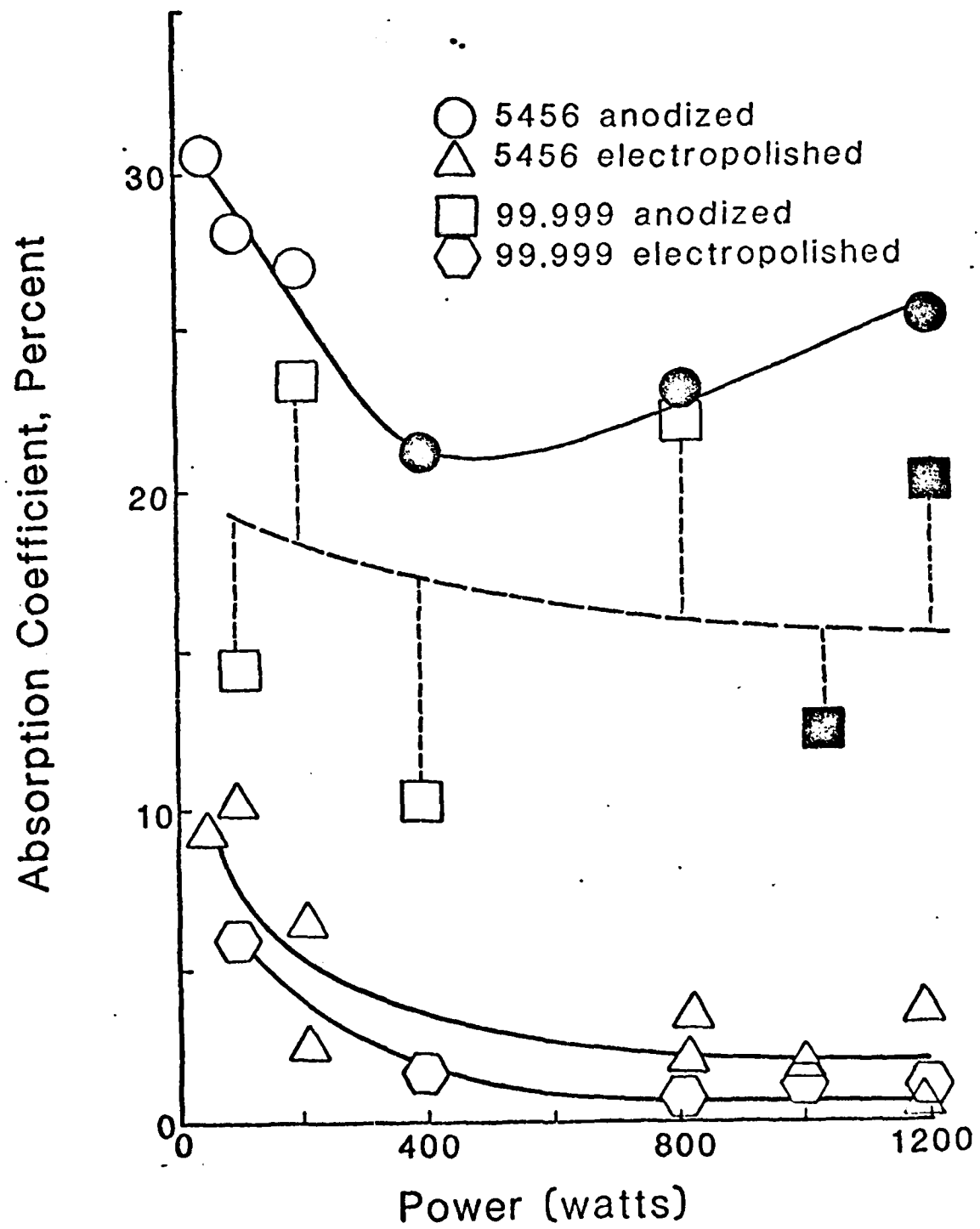


Figure 4



Figure 5a



Figure 5b



Figure 5c



Figure 5d

AD-A118 776

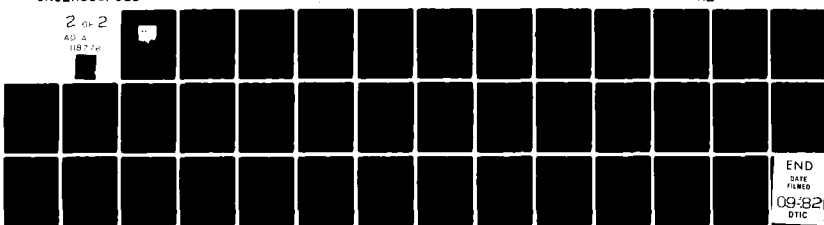
MASSACHUSETTS INST OF TECH CAMBRIDGE DEPT OF MATERIALS ETC F/G 13/8
HEAT SOURCE - MATERIALS INTERACTIONS DURING FUSION WELDING.(U)

APR 82 T W EAGAR, A BLOCK-BOLTON, C ALLEMAND N00014-80-C-0384

NL

UNCLASSIFIED

2 of 2
AD-A
118776



END
DATE
FILED
09-32
DTIC



Figure 5e

aluminum. The effect of joint geometry may be less important in the high magnesium alloy since the vapor reduces the effective depth of the cavity.

As a further test of the importance of keyhole geometry in laser welding of aluminum, a series of welds were made on 1100 and 5456 alloy at 15.2 cm/s travel speed and 3 kW beam power with helium shielding gas. Figures 5 a through e show a bead on plate weld, a 30° included angle groove weld, a 20° included angle groove weld and two square butt welds in 1100 alloy respectively. The very small amount of melting of the bead on plate geometry is increased with the V groove preparation which simulates a keyhole. The smaller weld cross section in Figures 5 d and e is due to the square butt acting as an average between a bead on plate and a near perfect keyhole. The difference in melting between Figures 5 d and e is probably due to small variations in either root gap or beam alignment in the gap. It appears that a square butt preparation is very sensitive to geometric changes which can significantly alter the percent of beam power absorption. The V groove preparation appears to be the best geometry for both weld consistency and efficient use of beam power. Similar results were observed with the 5456 alloy.

CONCLUSIONS

A study of laser light absorption on pure aluminum and 5456 alloy has shown the following:

1. Joint geometry has the greatest influence on beam absorption, while surface preparation also has a significant influence. Alloy composition is of lesser importance with bead on plate welds but could produce significant differences in the keyhole mode if volatile alloy additions are present.
2. Increased power absorption does not occur with the onset of melting but

rather with the beginning of keyhole formation.

ACKNOWLEDGEMENTS

The authors are grateful for the financial support of the Office of Naval Research under Contract N00014-80-C-0384. They are also indebted to Mr. Greg Dunn for assistance with many of the absorption studies and Mr. E. Prescott of the Alcoa Technical Center for production of the welded samples.

REFERENCES

1. R.C. Crafer, "Improved Welding Performance from a 2 kW Axial Flow CO₂ Laser Welding Machine," in Advances in Welding Processes, Fourth International Conference, The Welding Institute, Cambridge, England, 1978, p. 267.
2. Y. Arata and I. Miyamoto, "Some Fundamental Properties of High Power Laser Beam as a Heat Source," Trans JWRI. Vol. 3(1), 1972.
3. D.B. Snow, M.J. Kaufman, C.M. Banas and E.M. Breinan, "Evaluation of Basic Laser Welding Capabilities," United. Tech. Research Center Report R79-911989-17, July 1979.
4. Welding Kaiser Aluminum, 2nd Edition, Kaiser Aluminum Co., Oakland, California, 1978.

FIGURE CAPTIONS

Figure 1 - Schematic of cone and holder assembly used for absorption studies. Dimensions are in millimeters.

Figure 2 - Absorption versus power for a one second pulse. The open symbols represent samples without surface melting while the dark symbols represent samples that exhibited surface melting as viewed in the scanning electron microscope.

Figure 3 - Example of surface melting as seen in the scanning electron microscope. The specimen is 5456 alloy, anodized, 200 watts one second pulse, 200x magnification.

Figure 4 - Absorption versus power for a 0.5 second pulse. The dark symbols represent samples which exhibit surface melting.

Figure 5 - Welds made on 1100 aluminum with the following preparations: a) bead on plate, b) a 30 degree angle groove, c) a 20 degree angle groove, d) a square butt, and e) a square butt. All welds were made with equal power.

LIST OF TABLES

Table 1 - Percent power absorbed from a 200 Joule, two second pulse.

Table 2 - Percent power aborbed in a drilled keyhole 6.2 mm deep for a
0.5 second pulse.

APPENDIX E

100

Submitted for publication in Metallurgical Transactions

On the Relationship Between the Phase Diagram and the
Temperature Dependence of the Equilibrium Oxygen
Pressure in Metal Oxide Systems

A. Block-Bolten and Donald R. Sadoway*

ABSTRACT

A thermodynamic analysis of the concentration and temperature dependences of oxygen pressure in the Cr-Cr₂O₃ and V₂O₃-V₂O₅ systems is presented. The resulting plots of ln P_{O₂} versus 1/T show the various species in the context of relative reducibility or chemical reactivity not only for pure elements and compounds but also for the solutions and intermediate compounds which form. It is not necessary to presume a model for the thermodynamic behavior of solid and/or liquid solutions in this treatment. Verification is found in the previously reported data on the V₂O₃-V₂O₅ system.

INTRODUCTION

The search for alternative graphical representations of thermodynamic properties in binary and multicomponent systems is not new. Indeed, the

*A. Block-Bolten is Visiting Scientist, Materials Processing Center, and Donald R. Sadoway is Assistant Professor, Department of Materials Science and Engineering, both of the Massachusetts Institute of Technology, Cambridge, Massachusetts 02139.

method described herein has been used previously by Flengas et al. for binary systems of the types $ACl-A_2MC1_6$ (1-3) and $ACl-ANCl_6$ (4), where A is an alkali metal, M is one of Ti, Zr, or Hf, and N is one of Nb or Ta. The present report is the extension and modification of the treatment for application to "mainstream" systems of metallurgical interest. In particular, this article presents the detailed thermodynamic analysis of two oxide systems: $Cr-Cr_2O_3$ and $V_2O_4-V_2O_5$. It will be shown herein that when the total pressure of the gas phase can be equated to the partial pressure of one of the components, the method is extremely powerful in characterizing the system. Under such conditions a plot of $\ln P$ versus $1/T$ is a graphic illustration of the relevant phase equilibria. The adaptation of Flengas' representation to reactive metal oxide systems is the topic of this article.

The strength of the treatment is that the phase relationships are displayed to show the reacting species in the context of relative reducibility or chemical reactivity instead of in the context of state of matter and/or crystallographic modification as in the case of conventional phase diagrams, i.e., T versus X plots. From the standpoint of process design and optimization, the two representations complement one another, each providing vital information. Brewer and Searcy have examined the reactivities of various gaseous species over liquid Al_2O_3 and a mixture of liquid Al and solid Al_2O_3 (5). Knacke and Neumann used a similar approach in the analysis of oxide and sulfide systems of lead and zinc (6). However, in all cases partial pressures were those in equilibrium with pure elements or pure compounds in the condensed state. The present article extends the treatment to include the solutions and intermediate compounds formed by the principal components in question.

In doing so, it must be emphasized that it is not necessary to pressure a model for the thermodynamic behavior of the solid and/or liquid solutions which form. This keeps the treatment general and permits its applications to the most complicated of multicomponent systems.

In subsequent articles the treatment will be adapted to describe the phase equilibria in metal-metal nitride, metal-metal sulfide, and metal-metal halide systems. In addition, adaptation to systems in which more than one volatile component is present will follow.

FIGURES 1 and 2

THE THERMODYNAMICS OF OXIDE SYSTEMS

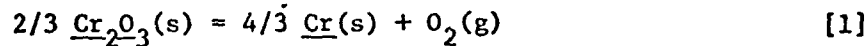
1. The Cr-Cr₂O₃ System

Figure 1 shows the schematic representation of the phase diagram of the Cr-Cr₂O₃ system. This representation follows closely that reported in the literature with the exception of allowing herein for a range of nonstoichiometry in Cr₂O₃ (7, 8). The various temperature-composition zones or phase fields have been labelled. Figure 2 shows the complete oxygen pressure plot for the Cr-Cr₂O₃ system. For the most part it is schematic, as there were few data in the literature on the oxygen pressures associated with the various phase equilibria in the system. In the low temperature range below the eutectic, oxygen pressures were estimated by extrapolation of data reported by Mazandarany and Pehlke (9).

To explain the derivation of the "pressure trees" on the Flengas

plot of Figure 2, the behavior of solutions of specific composition will be followed as they are heated through the various phase fields labelled on Figure 1.

Zone I is the region of nonstoichiometry in Cr_2O_3 and, as such, is a solid solution of Cr in Cr_2O_3 . The phases present are O_2 gas and the solid solution Cr- Cr_2O_3 . The equilibrium in this phase field may be written as



where the lines under Cr_2O_3 and Cr denote that each is in solution. The free energy change for the reaction is

$$\Delta G = \Delta G^\circ + \frac{4}{3} RT \ln a_{\text{Cr}} + RT \ln P_{\text{O}_2} - \frac{2}{3} RT \ln a_{\text{Cr}_2\text{O}_3} \quad [2]$$

where the activities of Cr and Cr_2O_3 are with respect to the pure solids, and it is assumed that the fugacity of O_2 is equal to its partial pressure. At equilibrium $\Delta G = 0$, and equation 2 may be rearranged as

$$RT \ln P_{\text{O}_2} = -\Delta G^\circ - \frac{4}{3} RT \ln a_{\text{Cr}} + \frac{2}{3} RT \ln a_{\text{Cr}_2\text{O}_3} \quad [3]$$

The temperature dependence of oxygen pressure is then

$$\frac{\partial \ln P_{\text{O}_2}}{\partial 1/T} = \frac{-\Delta H^\circ - \frac{4}{3} \bar{\Delta H}_{\text{Cr}} + \frac{2}{3} \bar{\Delta H}_{\text{Cr}_2\text{O}_3}}{R} \quad [4]$$

where ΔH° is the enthalpy of decomposition of pure solid Cr_2O_3 into pure solid Cr and O_2 gas at a pressure of 1 atmosphere (101.325 kPa), and $\bar{\Delta H}_{\text{Cr}}$ and $\bar{\Delta H}_{\text{Cr}_2\text{O}_3}$ are the partial molar enthalpies of mixing of Cr and Cr_2O_3 , respectively. Neglecting the temperature dependence of ΔC_p , for a solution of any composition in zone I a plot of $\ln P_{\text{O}_2}$ versus $1/T$ should be linear with a slope of $(-\Delta H^\circ - 4/3 \bar{\Delta H}_{\text{Cr}} + 2/3 \bar{\Delta H}_{\text{Cr}_2\text{O}_3})/R$. From the phase rule, the variance of the system in zone I is 2. Thus, solutions of different compositions should have different equilibrium oxygen pressures. The higher the oxygen content of the solution, i.e., the higher $X_{\text{Cr}_2\text{O}_3}$, the higher the equilibrium P_{O_2} . Assuming ΔH° to be large relative to $\bar{\Delta H}_{\text{Cr}}$ and $\bar{\Delta H}_{\text{Cr}_2\text{O}_3}$, in zone I a series of effectively parallel straight lines as shown in Figure 3(b) should represent the oxygen pressure above the solutions as selected in Figure 3(a). Table 1 summarizes these conclusions.

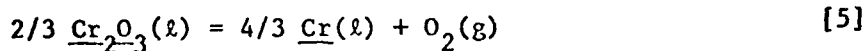
FIGURE 3

Zone II is defined by $T < T_{\text{eut}}$ and $0 < X_{\text{Cr}_2\text{O}_3} < X_\alpha$, where T_{eut} is the eutectic temperature of the Cr- Cr_2O_3 system and X_α is the composition of the chromium-rich end of the Cr- Cr_2O_3 solid solution of zone I. X_α is in fact a function of temperature, although in zone II it is expected to be effectively an isopleth as shown in Figure 1. The phases present are pure solid Cr, the α -solid solution of Cr- Cr_2O_3 and O_2 gas. The decomposition reaction is given in Table 1. Because the variance of the system in this phase field is unity, specifying the temperature is sufficient to fix the pressure. Thus, at a given temperature any mixture in zone II will have the same oxygen pressure, independent of its composition. Accordingly, the oxygen pressures for the entire range of mixtures of zone II fall on a single curve when plotted as a function of temperature

and composition. Assuming that x_α is effectively independent of temperature in zone II, the plot of $\ln P_{O_2}$ versus $1/T$ should be a straight line.

TABLE 1

Zone L is the all-liquid region where the phases present are oxygen gas and a homogeneous melt of Cr and Cr_2O_3 . The equilibrium is



The free energy change for this reaction is

$$\Delta G = \Delta G^\circ + \frac{4}{3} RT \ln \alpha_{Cr} + RT \ln P_{O_2} - \frac{2}{3} RT \ln \alpha_{Cr_2O_3} \quad [6]$$

where the activities of Cr and Cr_2O_3 are with respect to the pure liquids.

At equilibrium $\Delta G = 0$, and equation 6 may be rearranged as

$$RT \ln P_{O_2} = -\Delta G^\circ - \frac{4}{3} RT \ln \alpha_{Cr} + \frac{2}{3} RT \ln \alpha_{Cr_2O_3} \quad [7]$$

from which the temperature dependence of oxygen pressure is then

$$\frac{\partial \ln P_{O_2}}{\partial 1/T} = \frac{-\Delta H^\circ - \frac{4}{3} \bar{\Delta H}_{Cr} + \frac{2}{3} \bar{\Delta H}_{Cr_2O_3}}{R} \quad [8]$$

where ΔH° is the enthalpy of decomposition of pure molten Cr_2O_3 into pure molten Cr and O_2 gas at a pressure of 1 atmosphere

and $\bar{\Delta}H_{Cr}$ and $\bar{\Delta}H_{Cr_2O_3}$ are the partial molar enthalpies of mixing of Cr and Cr_2O_3 , respectively, in the molten solutions formed by them. The variance of the system in zone L is 2; hence, as in zone I, one expects P_{O_2} to be a function of both temperature and composition. Neglecting the temperature dependence of ΔC_p , for any given concentration the plot of $\ln P_{O_2}$ versus $1/T$ should be linear with a slope of $(-\Delta H^\circ - 4/3 \bar{\Delta}H_{Cr} + 2/3 \bar{\Delta}H_{Cr_2O_3})/R$. The ΔH° 's of equations 4 and 8 differ by the enthalpies of fusion of Cr and Cr_2O_3 :

$$\Delta H^\circ[8] = \Delta H^\circ[4] + 4/3 \Delta_{fus}^H Cr - 2/3 \Delta_{fus}^H Cr_2O_3 \quad [9]$$

On Figure 2 the oxygen pressure of solution 4 of composition, X_4 , which is at the eutectic composition, is represented by two straight lines intersecting at the eutectic temperature. The difference in slopes is due to the enthalpies of fusion of Cr and Cr_2O_3 and the partial molar enthalpies of solution in this melt.

Zone III is defined by $T_{eut} < T < T_{liquidus}$ and $X_{eut} < X_{Cr_2O_3} < X_\alpha$. This is the Cr_2O_3 -rich part of the Cr- Cr_2O_3 system between the melting point of Cr_2O_3 and the eutectic temperature. The phases present are O_2 gas, α -solid solution of Cr- Cr_2O_3 , and molten Cr- Cr_2O_3 saturated with respect to α -solid. The decomposition reaction is written in Table 1. With a variance of 1, the oxygen potential of the system in Zone III is fixed by temperature alone and is independent of composition.

Figure 4 indicates what happens when a solution of composition, X_2 , is heated through zone III. At temperature, T_A , a molten solution of

FIGURE 4

$\text{Cr-Cr}_2\text{O}_3$ of composition, X_{α_A} , is in equilibrium with α -solid solution of composition, X_{α_A} . The relative amounts of each phase are given by the lever rule applied along the tie line, $\bar{A}-\bar{A}$. As temperature increases from T_A to T_B , the composition of the α -solid solution changes to greater Cr_2O_3 content, i.e., $X_{\alpha_B} > X_{\alpha_A}$. The effect of this shift in oxygen content is to make the $\ln P_{\text{O}_2}$ versus $1/T$ plot nonlinear as shown in Figure 4(b). The previous description of the behavior of solutions in zone I showed that heating at constant composition, X_1 , from \bar{A} to \bar{B} should give a straight line on a plot of $\ln P_{\text{O}_2}$ versus $1/T$. Since at T_A , X_{α_A} is at \bar{A} which is lower in oxygen content than \bar{A} , P_{O_2} at \bar{A} must be lower there than at \bar{A} (recall that in zone I the variance is two and P_{O_2} is a function of both temperature and composition). At T_B , the α -solid composition has shifted to higher oxygen content so that its concentration, X_{α_B} , is identical to X_1 . Thus, at T_B the oxygen pressures in equilibrium with both solutions must be equal. Figure 4(b) shows this with two oxygen curves: the higher pressure straight line belonging to the homogeneous solid solution of composition X_1 , and the lower pressure line with positive curvature ($\partial^2 \ln P_{\text{O}_2} / \partial (1/T)^2 > 0$) that of the α -solid solution which lies on the boundary of zone III. Furthermore, since the variance in zone III is one, all solutions regardless of composition will show the same oxygen pressure dependence on temperature. This is shown in Figure 2 as the common curve EF.

The complete pressure curve for solution 2 is as follows. From room temperature up to the eutectic temperature the pressure is the same as that of solution 4. Then, as solution 2 is heated through

zone II from the eutectic to its liquidus temperature the pressure follows the curve GF. Increasing the temperature above the liquidus puts the solution into zone L where the pressure is shown in Figure 2 as a straight line emanating from GF.

The pressure in zone III having been described, it is instructive to return to solution 1 and to follow its behavior upon heating. At room temperature solution 1 is in zone I, the homogeneous solid solution, and, thus, has a pressure higher than that of solutions 2 and 4. The pressure curve in zone I is a straight line, essentially parallel to JG and extending up to the solidus temperature. From the solidus to the liquidus temperatures solution 1 is in zone III and, thus, its pressure follows curve GF over this temperature interval. At the liquidus the pressure breaks off curve GF into the all-liquid region and is represented by a straight line.

Zone IV is defined by $T_{\text{eut}} < T < T_{\text{monotectic}}$ and $0 < x_{\text{Cr}_2\text{O}_3} < x_{\text{eut}}$. This is the Cr-rich part of the Cr-Cr₂O₃ system between the eutectic and monotectic temperatures. The phases present are oxygen gas, pure solid Cr, and a liquid solution of Cr and Cr₂O₃ saturated with respect to solid Cr. With a variance of 1, the oxygen potential in zone III is fixed by temperature alone, is independent of composition, and, like that of zone III, is nonlinear on a Flengas plot. The difference is in the direction of curvature.

Figure 5 shows what happens when a solution of composition, x_6 , is heated through zone IV. At temperature, T_A , a molten solution of Cr and Cr₂O₃ of composition, x_g , is in equilibrium with pure solid Cr. As temperature increases from T_A to T_B , the composition of the melt

FIGURE 5

changes to lower Cr_2O_3 content, i.e., $X_{l_B} < X_{l_A}$. Since the liquid is the only oxygen bearing condensed phase in this case, the shift to lower Cr_2O_3 concentration will control the oxygen pressure in the gas phase so as to make the plot of $\ln P_{\text{O}_2}$ versus $1/T$ nonlinear with negative curvature. Figure 5(b) compares the pressure curves for two liquids, both initially of composition, X_{l_A} , at T_A . One melt is heated at constant composition, X_{l_A} , through zone L. A straight line is expected on a plot of $\ln P_{\text{O}_2}$ versus $1/T$. The other melt, which is equilibrated with pure solid Cr, follows the composition of the liquidus. At T_B , $X_{l_B} < X_{l_A}$; thus, P_{O_2} must be lower for the Cr saturated melt. Accordingly, the plot of $\ln P_{\text{O}_2}$ versus $1/T$ for this is nonlinear with negative curvature as shown in Figure 5(b).

Zone V is the miscibility gap. The phases present are oxygen gas and two molten phases, each consisting of Cr and Cr_2O_3 . One liquid is richer in Cr; the other is richer in Cr_2O_3 . With a variance of 1, oxygen pressure is fixed by temperature alone and is independent of composition along any isotherm. In this sense the situation is similar to zone IV. In both zones the oxygen-rich liquid at the right boundary of the phase field becomes depleted of oxygen as temperature increases. With the same rationalization given in Figure 5, it is expected that in zone V the oxygen pressure will have negative curvature. In Figure 2 this appears as the segment DC.

When solutions of conjugate composition, such as X_6 and X_7 , are heated from room temperature, P_{O_2} is expected to be the same for both of them up to the temperature of the boundary of the miscibility gap. At temperatures greater than this, the system is in zone L, the single-

phase liquid region. Since $X_{Cr_2O_3}$ is greater for X_6 than X_7 , P_{O_2} must be greater above solution 6 than solution 7. In both cases the temperature dependence of P_{O_2} in zone L is linear, the two lines diverging from a common point at the temperature of the boundary of the miscibility gap. The difference in slopes in zone L is related to the difference in the partial molar enthalpies of the two solutions. Furthermore, the very existence of a miscibility gap can be predicted from oxygen pressure data. Figure 2 shows that with pressure lines in the all-liquid region tending to intersect at temperatures above the eutectic, a liquid phase miscibility gap must result. Otherwise, below the temperature of intersection the oxygen pressure would be greater over the solution with the lower oxygen content. Instead, below the temperature of intersection the two solutions have a common equilibrium oxygen pressure and, thus, become conjugates of one another across the miscibility gap at temperatures down to the monotectic. The same predictive capacity applies in the identification of solid phase miscibility gaps.

Zone VI is thermodynamically identical to zone IV. Heating a solution of composition, X_9 , from room temperature one passes from zones II to IV to VI along the lowest curve through points E and B of Figure 2. Note that at high temperatures the segment BA in Figure 2 actually shows decreasing P_{O_2} as temperature increases. This is expected as one moves through zone VI where the oxygen bearing melt in equilibrium with pure solid Cr shifts with increasing temperature to lower and lower oxygen potentials.

This completes the description of the family of pressure curves for the entire Cr-Cr₂O₃ system.

FIGURES 6 AND 7

2. The V₂O₄-V₂O₅ System

Figure 6 shows a schematic representation of the phase diagram of the V₂O₄-V₂O₅ system (10, 11). Figure 7 shows the complete oxygen pressure plot for the system. For the most part it is schematic. Fotiev and Volkov reported measurements of oxygen pressure for temperatures below the V₂O₄-V₂O₅ eutectic (12). Block-Bolten has measured oxygen pressures up to 200 K above the V₂O₄-V₂O₅ eutectic (13).

Table 2 summarizes the chemical equilibria for the various regions of Figure 6. The methodology is the same as for the Cr-Cr₂O₃ system; accordingly, in the following discussion attention will be given only to departures from the earlier treatment. In this respect zones IV, VI and XIII are described.

TABLE 2

Zone IV is the two-phase region bounded by the vanadium-rich β-V₃O₇ solid solution and the oxygen-rich γ-V₆O₁₃ solid solution. For the most part the phase boundaries do not change composition with temperature. However, as one raises temperature near the V₃O₇ peritectoid, the right hand boundary of zone IV changes composition with temperature. In zone IV the variance is one, and at any given temperature there is one oxygen pressure common to all compositions. The equilibrium is



where the solid solutions are saturated with respect to one another. When the composition of the β-V₃O₇ solid solution shifts to higher oxygen content upon heating, the pressure plot shows upward curvature from the low temperature linear behavior in this zone. This is shown in Figure 7

where the oxygen pressure over solutions 8-12 is linear up to W, and then nonlinear from W to J.

Phase diagrams show V_3O_7 to be tentatively nonstoichiometric. This can be verified through the measurement of oxygen pressure in equilibrium with solid V_3O_7 and V_6O_{13} . Linear behavior right up to the V_3O_7 peritectoid would tend to show that this compound is stoichiometric or that deviations from stoichiometry are slight. On the other hand, pronounced curvature would demonstrate a significant range of composition for V_3O_7 . The same analysis holds for V_6O_{13} and V_2O_4 in relation to zones VI and XIII, respectively. It should be emphasized, in contrast, that plots of $\ln K_p$ versus $1/T$ under these conditions would be linear regardless of the natures of these compounds. In this respect, the oxygen pressure plots advocated herein have the capability of revealing something about the solution chemistry of the system.

FIGURE 8

It is instructive to follow, in Figure 8, the oxygen pressure curve generated by solution 11 which at room temperature lies in zone IV. Measurements of P_{O_2} in equilibrium with V_3O_7 and V_6O_{13} solids would give such results. At first glance the curve of Figure 8 appears strange. However, the present analysis shows this pressure curve to be normal. Fotiev and Volkov reported $\ln P_{O_2}$ to be effectively linear¹ in $1/T$ for the $V_3O_7-V_6O_{13}$ equilibrium all the way to the V_3O_7 peritectoid temperature (12). However, the slope of this line is so great that its projection would intersect the $\ln P_{O_2}$ line for the $V_6O_{13}-VO_2$ equilibrium

¹ Although their equation has a term in $\log T$, its effect on the value of $\log P_{O_2}$ is negligible.

at approximately 700 K. These two lines should diverge as temperature decreases, just as the lines for the $V_6^{13}-VO_2$ and $V_2^{15}-V_3^{17}$ equilibria do. One explanation for the intersection problem is that Fotiev and Volkov may have fit data from the region of positive curvature, denoted IVa on Figure 8 and data from zone IV to one common line. The broken line on Figure 8 illustrates how such curve fitting could estimate too steep a slope, i.e., more negative. FIGURE 9

Figure 9 shows the data of Fotiev and Volkov (12) and Block-Bolten (13) plotted in the Flengas format. The agreement in the data is remarkable even when plotted on such an expanded scale. Several things are worth noting. First, Block-Bolten's data show a relative minimum at the V_6^{13} peritectic temperature, a feature predicted by the thermodynamic analysis presented herein. Secondly, the curvature of the oxygen pressure line between the V_3^{17} peritectoid and V_6^{13} peritectic temperatures is so negative that over this temperature range oxygen pressure actually decreases with increasing temperature. Such behavior has been measured in other systems, such as $NbCl_5-KCl$ (14). On the other hand, at temperatures above the V_6^{13} peritectic the oxygen pressure increases with temperature while still showing negative curvature. This suggests that the slope of the liquidus above the V_6^{13} peritectic temperature is much steeper than below. In other words, above the V_6^{13} peritectic the increase in pressure due to the increase in temperature is not outweighed by the decrease in pressure due to the shift in the composition of the oxygen bearing condensed phase to lower oxygen content. Thirdly, the extrapolation of the oxygen pressure line reported by Fotiev and Volkov for the $V_6^{13}-VO_2$ equilibrium meets Block-Bolten's data at the peritectic temperature. This means that the oxygen-rich boundary of the $V_6^{13}-V_2^{14}$

solid phase field, zone VI on Figure 6, must be effectively vertical.

In view of this, one wonders whether V_6O_{13} may not be stoichiometric.

CONCLUSIONS

In this article an alternative graphical representation of the thermodynamics of phase equilibria in multicomponent systems has been adapted for use in oxide systems of mainstream metallurgical interest. It is evident from Figures 2 and 7 that the relevant pressure-temperature relationships are nontrivial and are considerably more elaborate than plots of $\ln K_p$ versus $1/T$. The properties of solid and liquid solutions have been described without the presumption of any thermodynamic model.

There are several significant differences between conventional phase diagrams (T versus X) and the Flengas plots ($\ln P_{O_2}$ versus $1/T$). For binary systems, conventional phase diagrams display two-phase fields as broad areas, whereas because P_{O_2} varies only with temperature and not composition here, two-phase fields on a Flengas plot appear as a single line. On the other hand, single phase fields, particularly nonstoichiometric intermediate compounds which may exist over relatively narrow ranges of composition appear dwarfed on a conventional phase diagram. On a Flengas plot these phase regions are more fully detailed. Indeed, it is precisely over these single phase regions that the most dramatic changes in oxygen potential occur. On this basis, the Gibbs-Helmholtz plot can identify potential errors in conventional phase diagrams regarding small ranges of solid compound nonstoichiometry which are often difficult to measure by standard techniques such as cooling curves or D.T.A. (differential thermal analysis). In this

respect, in the light of data which can be incomplete and/or conflicting, the Flengas plot could be of assistance to those concerned with computer generation of phase diagrams and with the selection of preferred values of thermodynamic properties. As well, the ability to predict the onset of liquid and solid phase miscibility gaps has been described.

The Flengas plots minimize the measurements which must be made to characterize a multicomponent system. As mentioned above, oxygen potentials are invariant with respect to composition over broad areas in two-phase fields and vary linearly there with $1/T$. Furthermore, interpolation between the all-liquid and two-phase solid regions must follow a uniquely defined curve. Thus, a simple eutectic type system with no solid solubility, for example, could be described in considerable detail with oxygen pressure data from just two compositions, one hypereutectic and one hypoeutectic. A vivid example of this is given in the vapor pressure measurements by Kvande in the $\text{Na}_3\text{AlF}_6-\text{Al}_2\text{O}_3$ system (15). In Ref. 15, Figure 2 plots $\log P$ versus $1/T$. One sees a common line up to 960°C , the Na_3AlF_6 eutectic. At higher temperatures there are two curves, each of opposite curvature. From these curves emanate linear segments at their respective liquidus temperatures. This fully corroborates the analysis presented herein.

Finally, there is the potential extension of this treatment to computer aided prediction of thermodynamic properties of multicomponent systems with attendant savings in data gathering.

ACKNOWLEDGEMENTS

The authors wish to acknowledge the financial support of the Office of Naval Research Contract No. N000140-C-80-0384 (for A. R. B.) and the Mining and Mineral Resources Research Institute of the Massachusetts Institute of Technology (for D. R. S.).

REFERENCES

1. R. L. Lister and S. N. Flengas, Can. J. Chem., 1965, Vol. 43, pp. 2947-2969.
2. J. E. Dutrizac and S. N. Flengas, in Advances in Extractive Metallurgy, Institution of Mining and Metallurgy, 1968, pp. 572-599.
3. S. N. Flengas and P. Pint, Can. Metall. Q., 1969, Vol. 8, pp. 151-166.
4. D. R. Sadoway and S. N. Flengas, in Extractive Metallurgy of the Refractory Metals, H. Y. Sohn, O. N. Carlson, and J. T. Smith, editors, AIME, Metals Park, 1981, pp. 107-126.
5. L. Brewer and A. W. Searcy, J. Am. Chem. Soc., 1951, Vol. 73, pp. 5308-5321.
6. O. Knacke and W. Neumann, Erzmetall, 1956, Vol. 9, pp. 261-310.
7. Ya. I. Ol'shanskii and V. K. Shlepov, Dokl. Akad. Nauk SSSR, 1953, Vol. 91, pp. 561-564.
8. R. E. Johnson and A. Muan, J. Amer. Ceram. Soc., 1968, Vol. 51, pp. 430-433.
9. F. N. Mazandarany and R. D. Pehlke, J. Electrochem. Soc., 1974, Vol. 121, pp. 711-714.
10. K. Kosuge, J. Phys. Chem. Solids, 1967, Vol. 28, pp. 1613-1621.
11. S. Kachi and R. Roy, Second Quarterly Report on Crystal Chemistry Studies, Pennsylvania State University, University Park, PA, Dec. 4, 1965.
12. A. A. Fotiev and V. L. Volkov, Zh. Fiz. Khim., 1971, Vol. 45, p. 2671.
13. A. Block-Bolten, Can. J. Chem., 1976, Vol. 54, pp. 1967-1970.

14. D. R. Sadoway and S. N. Flengas, Can. J. Chem., 1978, Vol. 56,
pp. 2538-2545.
15. H. Kvande, Electrochimica Acta, 1980, Vol. 25, pp. 237-240.

LIST OF FIGURES

- Figure 1** Schematic representation of the Cr-Cr₂O₃ phase diagram.
- Figure 2** Temperature and concentration dependences of oxygen pressure in the Cr-Cr₂O₃ system (schematic).
- Figure 3(a)** Phase diagram detail of zone I.
- 3(b)** Temperature and concentration dependences of oxygen pressure in zone I.
- Figure 4(a)** Phase diagram detail of zones I and III.
- 4(b)** Temperature and concentration dependences of oxygen pressure in zones I and III.
- Figure 5(a)** Phase diagram detail of zone IV liquidus
- 5(b)** Temperature and concentration dependences of oxygen pressure in the region of zone IV liquidus.
- Figure 6** Schematic representation of the V₂O₄-V₂O₅ phase diagram.
- Figure 7** Temperature and concentration dependences of oxygen pressure in the V₂O₄-V₂O₅ system (schematic).
- Figure 8** Temperature dependence of oxygen pressure of solution 11
- Figure 9** Comparison of previously reported oxygen pressure data in the V₂O₄-V₂O₅ system to behavior predicted herein.

LIST OF TABLES

Table 1 Summary of Equilibria in the Cr-Cr₂O₃ System

Table 2 Summary of Equilibria in the V₂O₄-V₂O₅ System

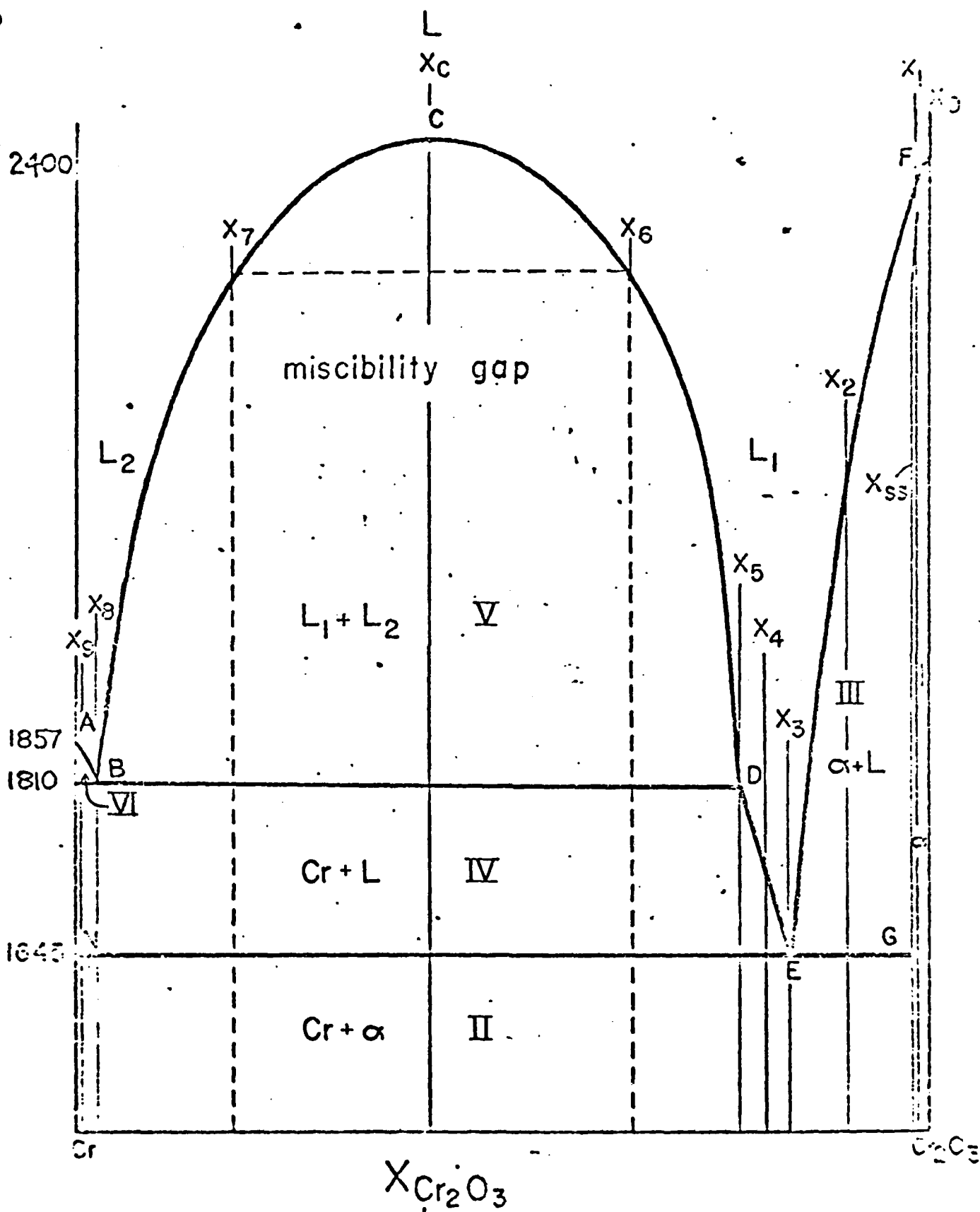


Figure 1

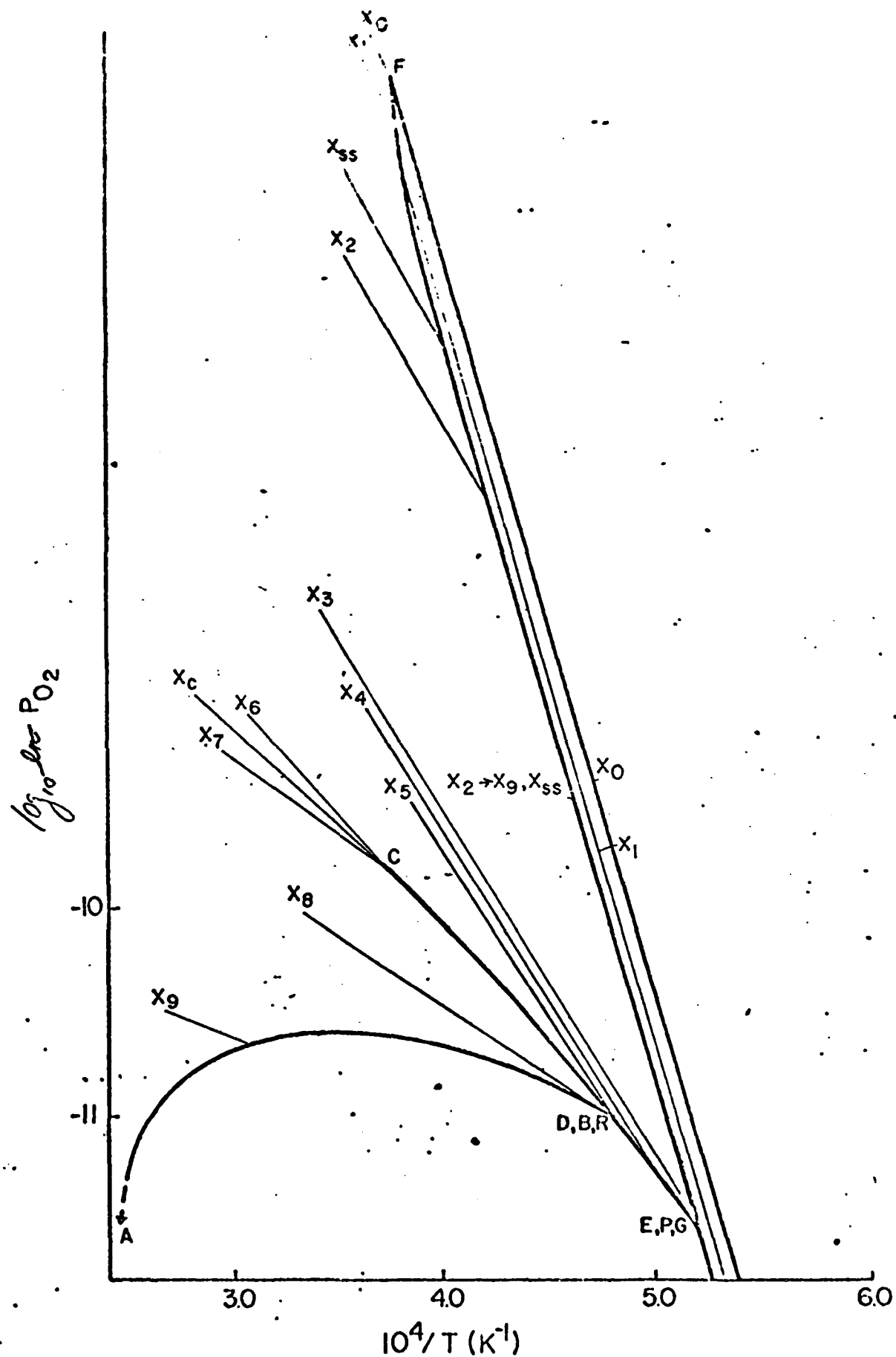


Figure 2

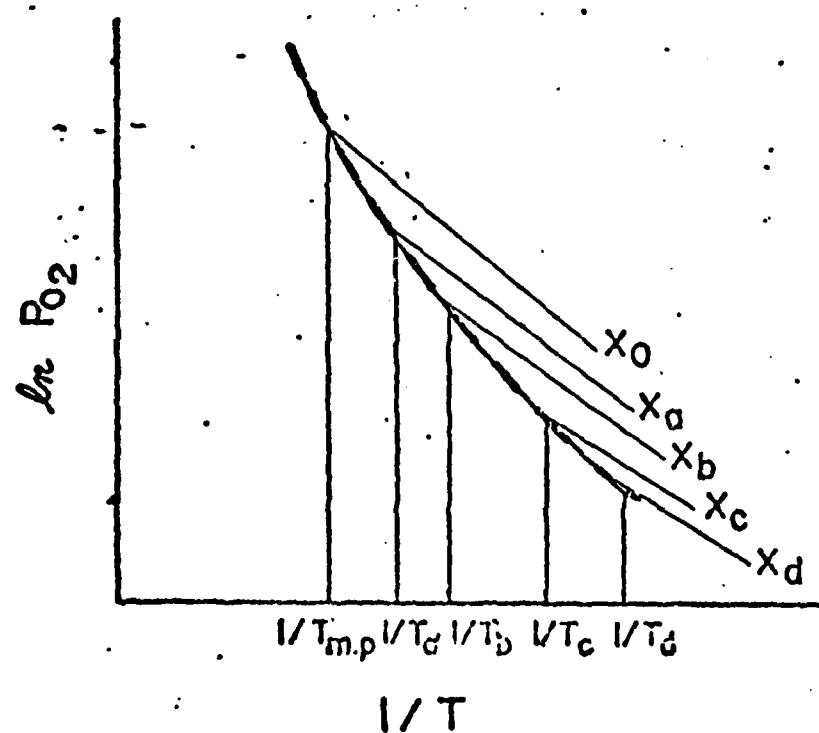
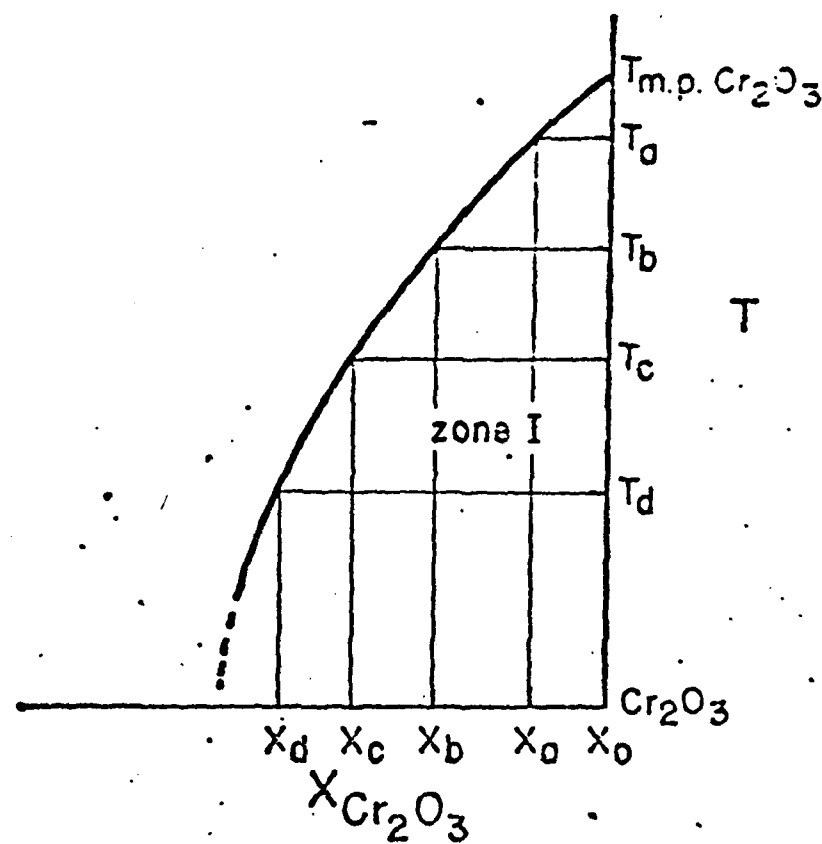


Figure 3

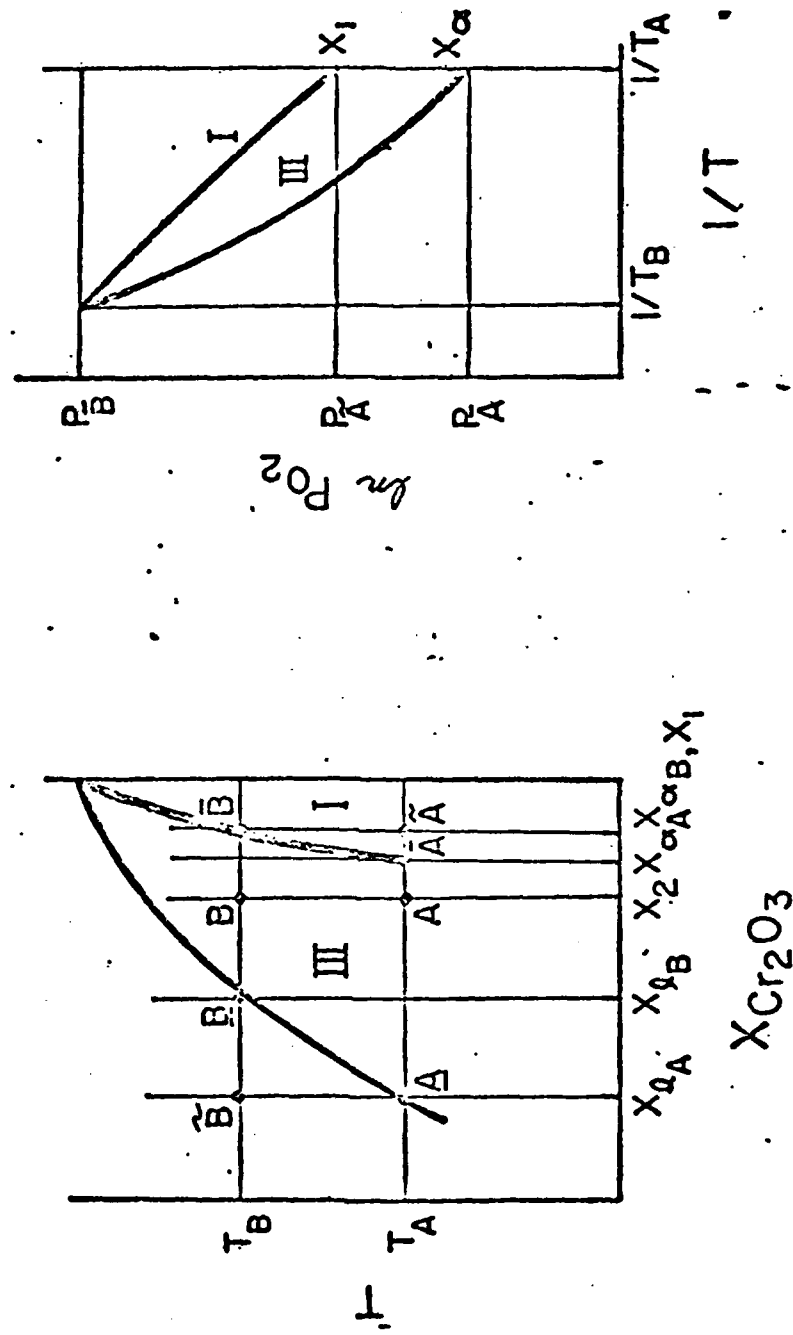


Figure 4

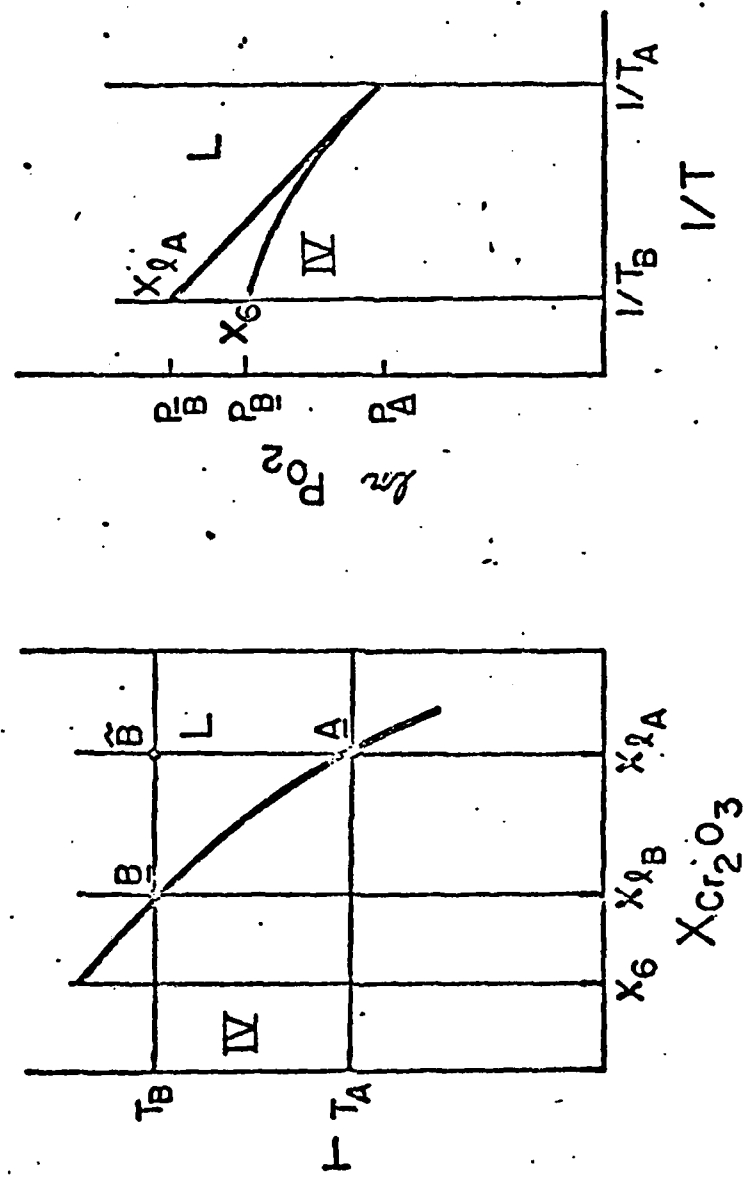


Figure 5

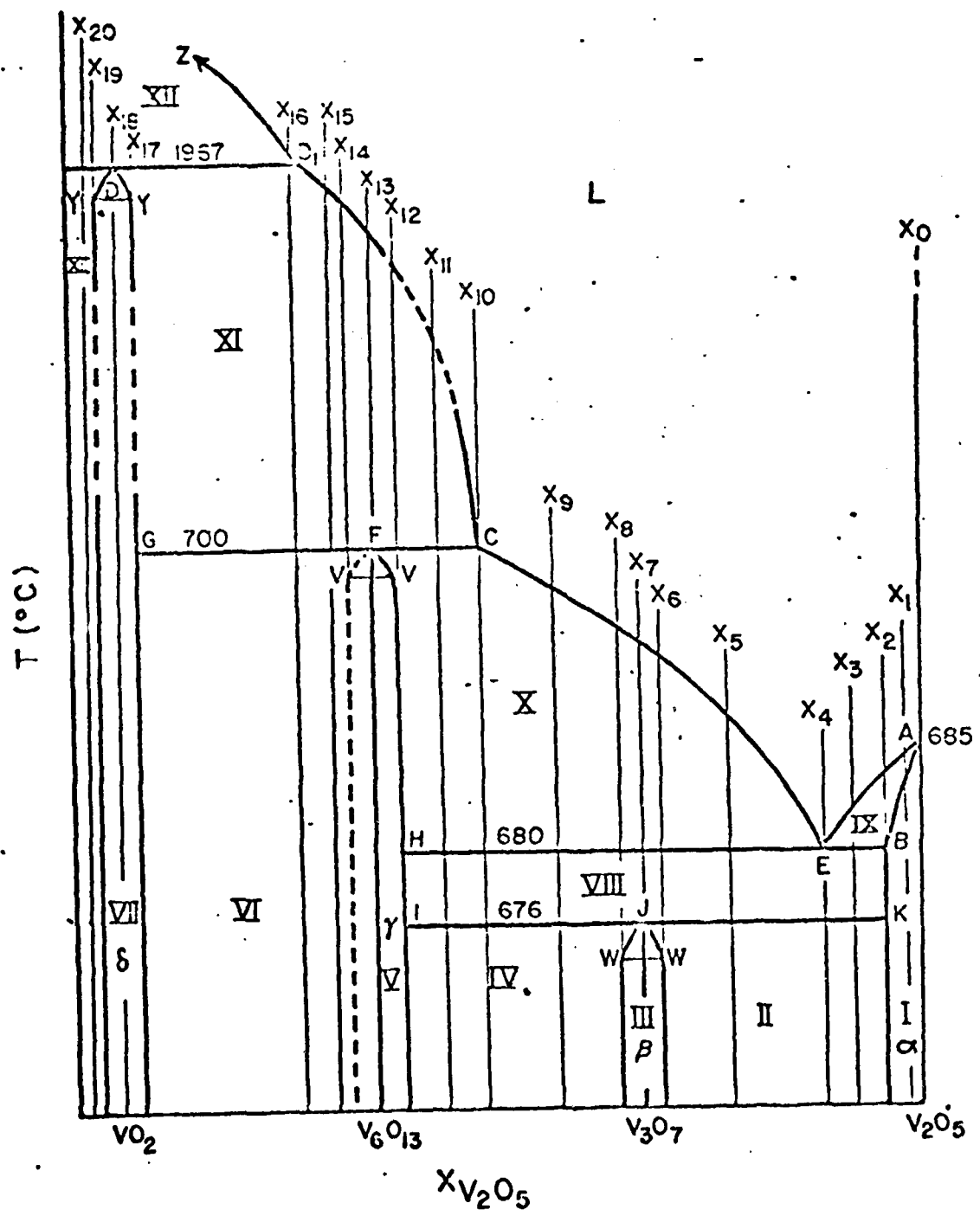


Figure 6

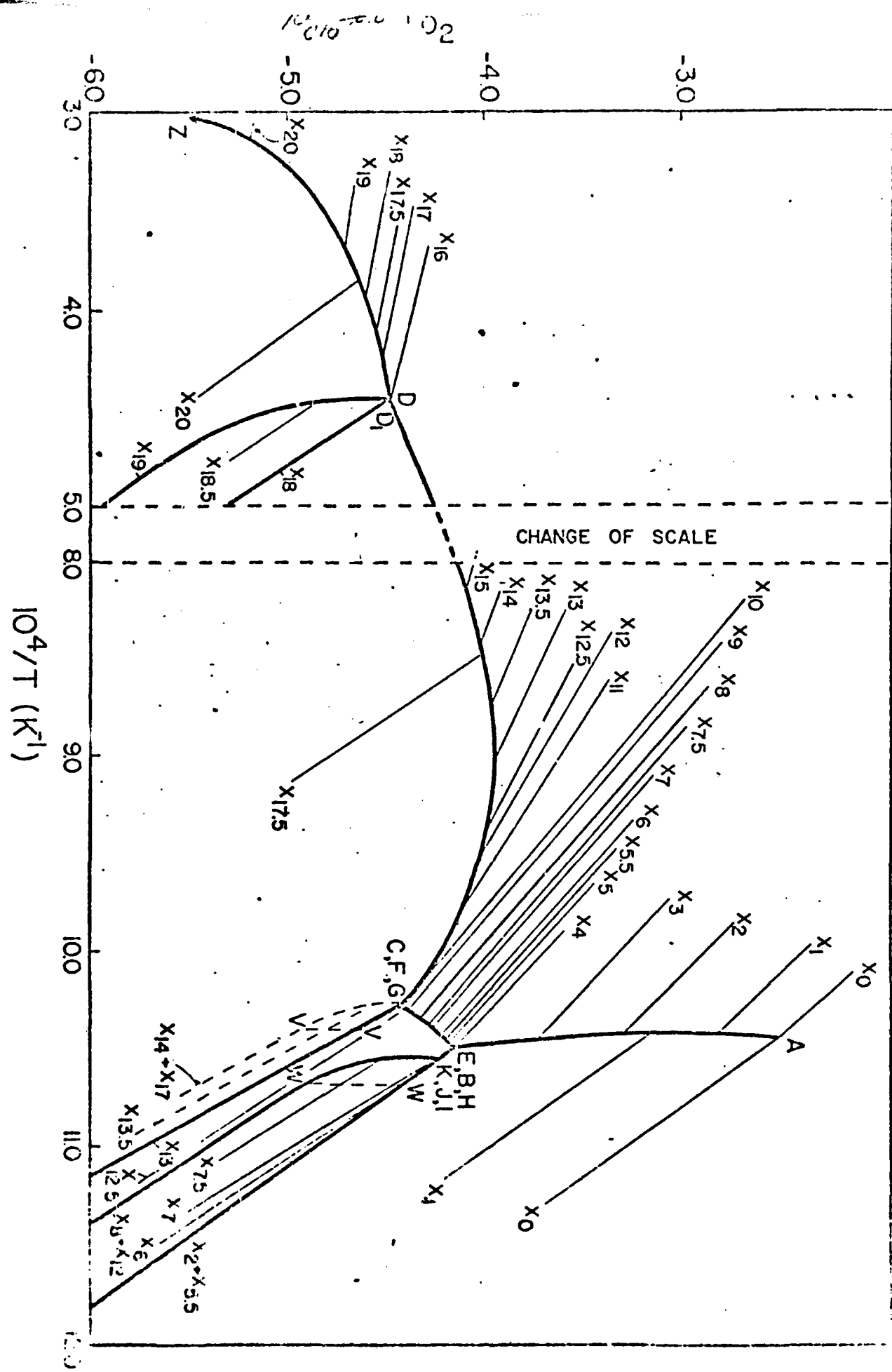


Figure 7

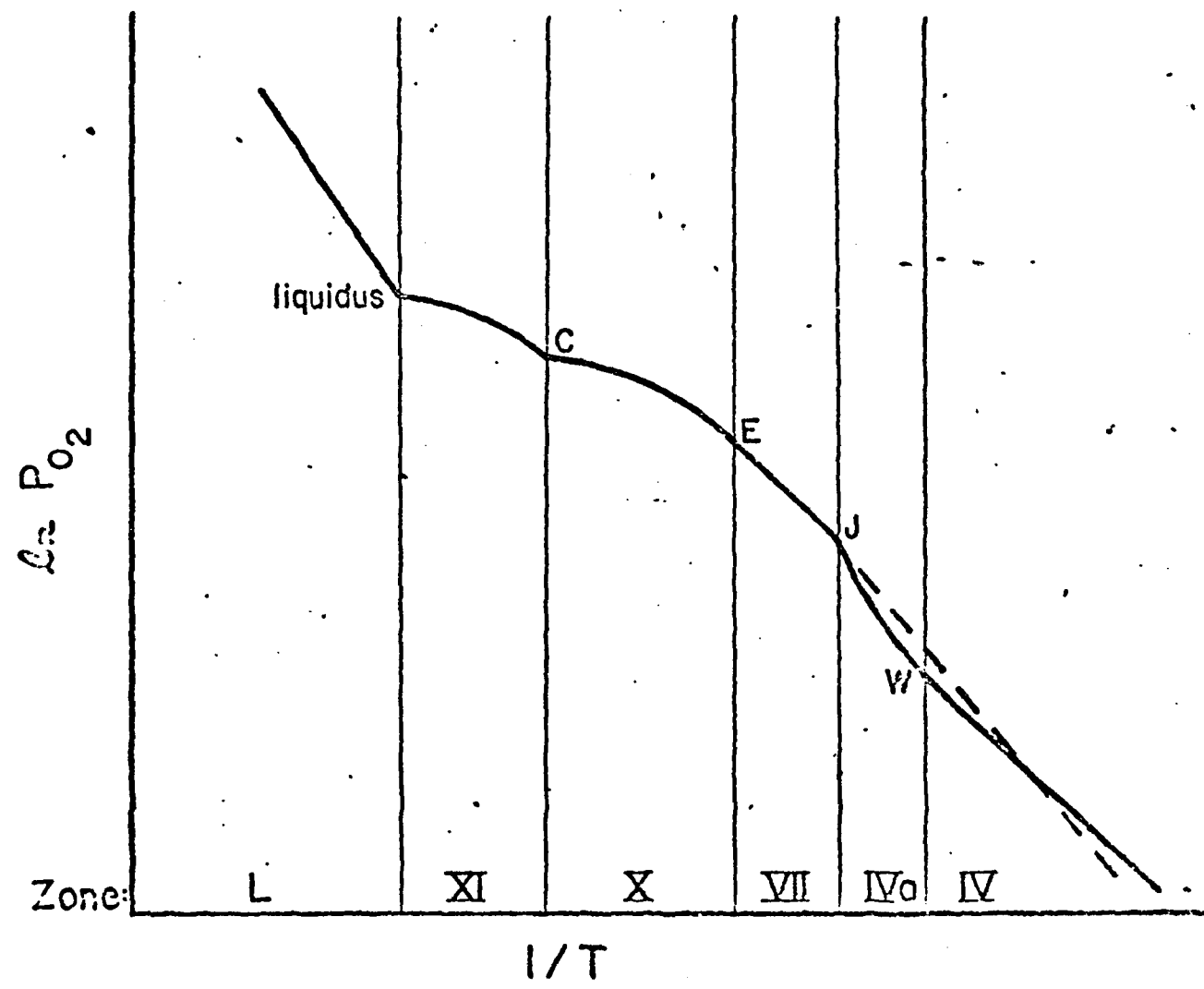


Figure 8 -

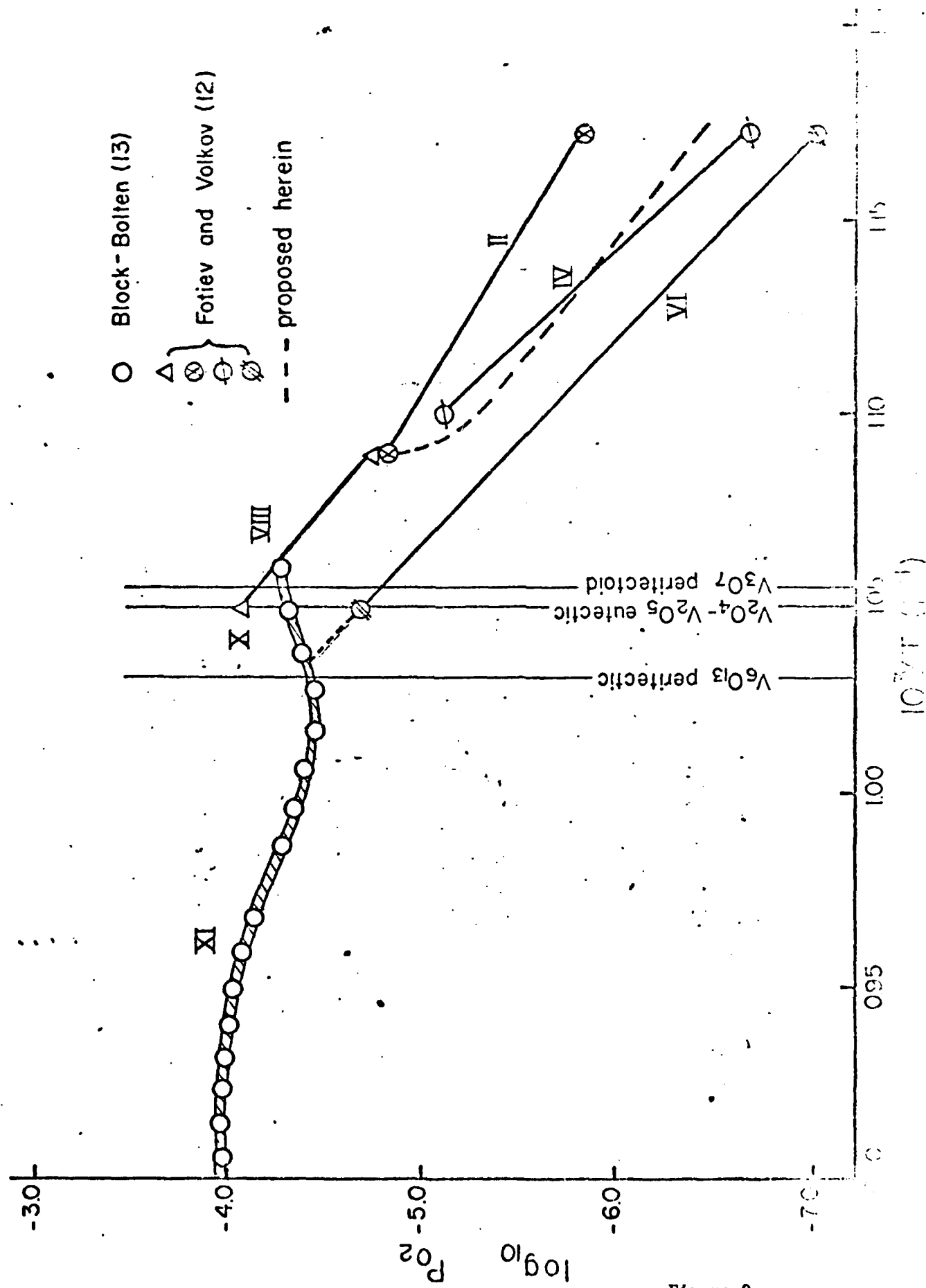


Figure 9

TABLE I - Summary of Equilibria in the Cr - Cr₂O₃ System

Zone ¹	Equilibrium ⁵	Variance ²	Curvature ³	Compositions	Remarks
I	2/3 Cr ₂ O ₃ (s,sat a) = 4/3 Cr(s) + O ₂	2	linear	$x_0 + x_{88}$	none
II	2/3 Cr ₂ O ₃ (s,sat a) = 4/3 Cr(s) + O ₂	1	linear provided that a / (a+Cr) boundary is an isopleth	$x_{88} \rightarrow x_9$	a is the Cr-rich solid solution of Cr and O which bounds Zone II
III	2/3 Cr ₂ O ₃ (s,sat a) = 4/3 Cr(l) + O ₂	1	positive	$x_{88} \rightarrow x_3$	none
IV	2/3 Cr ₂ O ₃ (l) = 4/3 Cr(l,sat pure Cr(a)) + O ₂	1	negative	$x_3 \rightarrow x_9$	degree of curvature depends upon slope of liquidus
V	2/3 Cr ₂ O ₃ (l,sat l ₁) = 4/3 Cr(l,sat l ₂) + O ₂	1	negative	$x_3 \rightarrow x_8$	curvature governed by shape of Cr-rich edge of stability gap
VI	2/3 Cr ₂ O ₃ (s) = 4/3 Cr(l,sat pure Cr(a)) + O ₂	1	negative	$x_3 \rightarrow x_9$	thermodynamically, zones IV and VI are identical
VII	2/3 Cr ₂ O ₃ (s) = 4/3 Cr(l) + O ₂	2	linear	$x_0 + x_9$	none

¹ Zones are defined in Figure 1.² Variance defined by Gibbs phase rule.³ Curvature defined as $\beta^2 \ln T_0^2 / \beta(1/T)^2$.⁴ Compositions as labelled in Figure 1.⁵ The notation "sat a" means "saturated with respect to phase a."

TABLE 2 - Summary of Equilibria in the $\text{V}_2\text{O}_4 - \text{VO}_3$ System

Zone ¹	<u>Equilibrium³</u>	<u>Variance²</u>	<u>Curvature³</u>	<u>Compositions⁴</u>	<u>Remarks</u>
I	$6 \underline{\text{V}_2\text{O}_3}(\text{s}) = 4 \underline{\text{V}_2\text{O}_7}(\text{s}) + \text{O}_2$	2	linear	x_0, x_1, x_2	none
II	$6 \underline{\text{V}_2\text{O}_3}(\text{s}, \text{sat } \delta) = 4 \underline{\text{V}_2\text{O}_7}(\text{s}, \text{sat } \delta) + \text{O}_2$	1	linear provided that $\delta/(a+b)$ boundary is an isopleth	$x_2 + x_6$	α and β are the U-rich and V-rich, respectively, solid solutions which bound zone I
III(a)	$6 \underline{\text{V}_2\text{O}_3}(\text{s}) = 4 \underline{\text{V}_2\text{O}_7}(\text{s}) + \text{O}_2$	2	linear	x_6, x_7	none
III(b)	$4 \underline{\text{V}_2\text{O}_7}(\text{s}) = 2 \underline{\text{V}_2\text{O}_{13}}(\text{s}) + \text{O}_2$	2	linear	x_7, x_8	none
IV	$4 \underline{\text{V}_2\text{O}_7}(\text{s}, \text{sat } \gamma) = 2 \underline{\text{V}_2\text{O}_{13}}(\text{s}, \text{sat } \delta) + \text{O}_2$	1	linear up to T_{W}^1 , above T_{W} , positive curvature	$x_8 + x_{12}$ $x_7 + x_{12}$	δ and γ are the U-rich and V-rich, respectively, solid solutions which bound zone IV
V(a)	$4 \underline{\text{V}_2\text{O}_7}(\text{s}) = 2 \underline{\text{V}_2\text{O}_{13}} + \text{O}_2$	2	linear	$x_{12p} + x_{13}$	none
V(b)	$2 \underline{\text{V}_2\text{O}_{13}}(\text{s}) = 12 \underline{\text{VO}_2}(\text{s}) + \text{O}_2$	2	linear	$x_{13} + x_{14}$	none
VI	$2 \underline{\text{V}_2\text{O}_{13}}(\text{s}, \text{sat } \delta) = 12 \underline{\text{VO}_2}(\text{s}, \text{sat } \gamma) + \text{O}_2$	1	linear up to T_{W}^1 , above T_{W} , positive curvature	$x_{14} + x_{17}$ $x_{13} + x_{17}$	γ and δ are the U-rich and V-rich, respectively, solid solutions which bound zone VI
VII(a)	$2 \underline{\text{V}_2\text{O}_{13}}(\text{s}) = 12 \underline{\text{VO}_2}(\text{s}) + \text{O}_2$	2	linear	$x_{17} + x_{18}$	none
VII(b)	$16 \underline{\text{VO}_2}(\text{s}) = 2 \underline{\text{V}_2\text{O}_{13}}(\text{s}) + \text{O}_2$	2	linear	$x_{18} + x_{19}$	none

VIII	$3 \underline{Y}_2^0(t, \text{sat } \gamma) = \underline{Y}_6^0(t, \text{sat } \alpha) + 0_2$	1	Linear provided that α/γ is boundary is an isopleth	$x_2 + x_{12}$	α, γ defined above
IX	$3 \underline{Y}_2^0(t, \text{sat } \alpha) = \underline{Y}_6^0(t, \text{sat } \gamma) + 0_2$	1	positive	$x_0 + x_4$	none
X	$3 \underline{Y}_2^0(t) = \underline{Y}_6^0(t, \text{sat } \gamma) + 0_2$	1	negative	$x_4 + x_{13}$	Note that above $T_Y, x_{12} - x_{13}$ are included in Zone $\frac{1}{2}$
XI	$2 \underline{Y}_2^0(t) = 4 \underline{Y}_2^0(t, \text{sat } \delta) + 0_2$	1	negative	$x_{10} + x_{16}$	Note that above $T_Y, x_{12} - x_{13}$ are included in Zone $\frac{1}{2}$
XII	$14 \underline{Y}_2^0(t) = 2 \underline{Y}_7^0(t, \text{sat } \epsilon) + 0_2$	1	negative	$x_{16} + x_{19}$	ϵ is the Verlich solid solution, which bounds Zone XII. ϵ is not shown on Figure 6.
XIII	$14 \underline{Y}_2^0(t, \text{sat } \epsilon) = 2 \underline{Y}_7^0(t, \text{sat } \delta) + 0_2$	1	linear up to T_Y , positive curvature above T_Y , positive curvature	x_{20}	ϵ, δ defined above
XIV	$2 \underline{Y}_2^0(t) = 4 \underline{Y}_2^0(t) + 0_2$	2	linear	$x_0 + x_{19}$	none

¹ Zones are defined in Figure 6.² Variance defined by Gibbs phase rule.³ Curvature defined as $\dot{\sigma}^2 \ln P_0 / \sigma(1/\tau)^2$.⁴ Compositions as labelled in Figure 6.⁵ The notation, "sat v" means "saturated with respect to phase v"

